Synthesis and Characterization of Nanocrystalline Diamond Films

Dissertation

Von der Fakultät für Physik
der Universität Duisburg-Essen
zur Erlangung des akademischen Grades eines
Doktors der Naturwissenschaften (Dr. rer. nat.)
genehmigten Dissertation
von

Nicolas Wöhrl

geboren am 25. April 1974
in Recklinghausen

Tag der Einreichung: 18. März 2010
Prüfungsvorsitzender: Prof. Dr. Lothar Schäfer
Erster Gutachter: Prof. Dr. Volker Buck
Zweiter Gutachter: Prof. Dr. Dieter Mergel

“Maximum in rebus humanis,
non solum inter gemmas,
pretium habet adamas.”

Naturalis Historia, C. Plinius Secundus (23-79 AD)

- Für Finjas -

dem neugierigsten kleinen Forscher in meinem Leben

Table of Contents

1 Abstract

Innovative Materials are the driving force for technological progress and with it for the international competitiveness of the industry. Recently a new area of work was opened here: Nanotechnology.
Nanocrystalline Diamond (NCD) is a product of this area. Besides replacements for dwindling or expensive raw materials this material is in the spotlight because of enhanced and versatile properties. Nanocrystalline or even ultrananocrystalline diamond (UNCD), as named by the Argonne National Laboratory group that performed the pioneering works in this field, is not only hard, but also even tough which is not the case for single crystalline diamond.
Although great effort was already made to characterize the crystalline part of this new form of nano-structured material, the influence of the matrix - surrounding the nanosized diamond crystals - on the film properties was mostly neglected. Therefore the aim of this work is to investigate the role of the matrix in UNCD films and its influence on the material properties to tailor films with specific properties.

Innovative Materialien sind die treibende Kraft für technologischen Fortschritt und damit für die internationale Konkurrenzfähigkeit der Industrie. Erst kürzlich wurde ein weiteres Arbeitsfeld erschlossen: die Nanotechnologie.
Nanokristalliner Diamant (NCD) ist ein Produkt dieses neuen Gebietes. Neben der Möglichkeit schwindende oder teure Rohstoffe zu ersetzen bietet dieses Material weitere verbesserte und vielfältige Eigenschaften. Nanokristalliner oder ultrananokristalliner Diamant (UNCD), wie er durch die Argonne National Laboratory Gruppe benannt wurde welche die Pionierarbeiten in diesem Feld geleistet hat, ist nicht nur hart, sondern auch gleichzeitig zäh, eine Eigenschaft die einkristalliner Diamant nicht aufweist.
Wenngleich viele Forschungsarbeiten sich auf die Charakterisierung der kristallinen Körner dieser Schichten konzentrierten, wurde die Nanokristalle umgebende Matrix als Korngrenze abgetan – eine Simplifizierung, die ihrem Einfluß auf die Schichteigenschaften nicht gerecht werden konnte. Es ist die Aufgabe dieser Arbeit erstmalig die Rolle der Matrix in UNCD-Schichten auf die Materialeigenschaften zu beleuchten um dadurch Schichten mit gezielten Eigenschaften zu designen und abzuscheiden

2 Introduction

Nanotechnology is the realization of an idea that Nobel-prize winner R. P. Feynman presented in his famous talk *There's plenty of Room at the Bottom* [Fey60] at the annual meeting of the American Physical Society on December 29th 1959; new effects and special properties occur in nanotechnology mainly for two reasons: on the one hand quantum effects can play a significant role when structures get small and on the other hand nanostructured materials possess a significant amount of surface or interface compared to their volume. These aspects are significantly influencing the materials properties when structures get smaller because the internal surfaces or the crystal-surrounding matrix start to determine essential material properties.

A recent remarkable example for solving a technological problem by nanotechnology is the toughness of a material. Hardness is one of the most important material properties for engineers for many applications such as cutting tools or drills. One problem is that usually hard materials are brittle at the same time, giving a clear disadvantage for the mentioned applications. Therefore the ideal material for cutting tools would be both hard and tough. This is now possible due to Nanotechnology: Nobel-prize winner P. G. de Gennes showed that with right design of nano-layered structures a *supermodulus* called effect can be observed [Oku01] – it is characterized by a pronounced maximum of hardness and enhanced toughness; especially by combination of nanometer sized hard with soft layers a crack arising in the hard layer can be parried in the soft layer. Indeed the same was shown in the case of nanocrystalline diamond films where nanocomposites consisting of hard nanocrystals embedded in an amorphous matrix lead to films with considerable toughness without loosing too much of the hard character [Vep99]. Due to its ability to form sp^3-, sp^2- and sp-bonds, different forms of carbon exist that make yet carbon alone an ideal element for nanostructuring.

The hardest known material is diamond and only the III-V analogue to diamond, cubic Boron-Nitride that is not found in nature, achieves comparable values. Due to its extraordinary properties natural and HPHT diamond is used for a long time as a material for tools, especially for grinding or sawing of rocks. Since the 1980s the conventional (microcrystalline) diamond deposited by thin film technology is increasingly used. One major problem with the microcrystalline diamond films

deposited in CVD processes is the high surface roughness. Additionally the homogeneous deposition of diamond films on substrates with a high aspect ratio is difficult with films consisting of relatively large crystals.

The nanocrystalline diamond grains are embedded into an amorphous carbon matrix whose fraction to the overall film volume is increased with decreased grain size. The increasing effect of the nanocrystals-surrounding matrix on the film properties gives another degree of freedom for the material. The well-aimed use of an amorphous matrix for nanocrystalline diamond grains leads to an enormous field of new materials, because a whole class of carbon based materials (*diamondlike carbon,* DLC) can be used as matrix that may contain carbon solely (a-C) or carbon and hydrogen (a-C:H) as well as other components like metals (Me-C:H); additionally other dopants like silicon, oxygen, halogens or nitrogen may be added with considerable effect on the film properties. Various examples can be found in the literature. By combining soft matrix properties with the hard diamond crystals it is possible to combine hard with elastic properties and get a material that is hard and tough at the same time. With the mechanical stress in the films it was possible to tailor yet another very important mechanical property for the application of UNCD films by adjusting the overall matrix fraction to the film volume (in the case of a 3D matrix surrounding the nanocrystals) [Woe07]. In different works it was shown that it is possible to adjust the conductivity of the films by n-type and p-type doping of the matrix.

The first and most important property of a coating is abviously the adhesion on the substrate. Since quantitatively the adhesion energy between substrate and film correlates with a critical mechanical stress [Pun04] optimization of the adhesion can be realized by reducing the mechanical stress in the deposited films. Adhesion of the film on the substrate is obviously one of the central requirements for any technical application of thin films even though the importance of the adhesion depends on the kind of application. Therefore the influence of the process parameters on the film properties with special attention on the residual stress is investigated in this work as a major topic.

3 Fundamentals

3.1 Carbon Thin Films

In the following chapter the fundamentals of deposition of either microcrystalline and nanocrystalline diamond as well as amorphous films should be discussed after a brief look on the history of CVD diamond deposition. Additionally amorphous carbon films will be briefly introduced due to the appearance of amorphous structures of carbon in the grain boundaries of the diamond films or as the matrix of NCD.

3.1.1 Synthesis of Diamond

The combination of outstanding properties such as highest hardness, highest thermal conductivity at room temperature and remarkable semiconductor properties make diamond one of the most promising materials for science and technology. Due to the fact that natural diamonds are very rare and expensive and because of strategic reasons due to the importance for petrol exploration, research programs were started after World War II trying to synthesize this allotrope of carbon.

At room temperature and atmospheric pressure, graphite is the stable crystalline form of carbon, with an enthalpy only 2 kJ mol^{-1} lower than diamond. In graphite each atom is bonded to three others in a plane composed of fused hexagonal rings (compare with Chapter 3.1.5, Figure 3.4). Only at very high pressures carbon forms an allotrope called diamond with each atom bonding to four neighbours. At these high-pressure conditions diamond is the thermodynamically stable configuration of carbon as can be seen in the phase diagram of carbon in Figure 3.1.

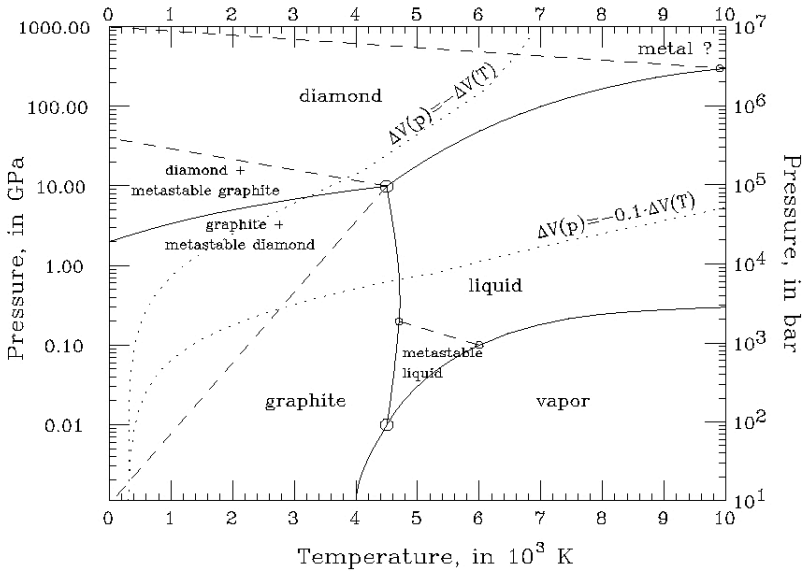

Figure 3.1 Phase diagram of carbon

Without knowledge of the phase diagram the first successful way of synthesising diamond in the laboratory was by duplicating the natural process of diamond forming: by applying high pressures and high temperatures. After the pioneering work of Bridgeman on HPHT (high pressure high temperature) crystal growth – honoured with the Nobel price in 1946 - who did not succeed in synthesis of diamond because the funding had finished, H. Liander at Allemanna Svenska Elektriska A.B. in Sweden [Lia55] and F.P. Bundy and coworkers at General Electrics in the early 1950s [Bun55] successfully synthesized diamond with the technology and methods developed by Bridgman. Although the technology of HPHT synthesis of diamond is very successful and widely used it has nevertheless some disadvantages. First of all the technical complexity to realize high pressures and high temperatures is very high. Secondly the appliance of high pressures is only possible for rather small volumes, limiting this technology to the synthesis of diamonds of sizes around some cubic millimetres. These drawbacks of the HPHT technology lead to the attempt to synthesise diamond from the metastable phase at low pressures.

Early tube oven experiments by W. G. Eversole [Eve62] and by J. C. Angus et al. [Ang68] were performed to successfully overcoat diamond seeds with diamond films (auto epitaxy). In both cases the co-deposited graphite was removed by a cyclic growth and etching procedure using H_2 in the case of Eversole and atomic hydrogen by Angus. The breakthrough to coat non-diamond substrates was achieved by the Russian research group of B. V. Deryagin, B. V. Spitzin, D. V. Fedoseev et al. who reported successful growth of diamond from the gas phase in 1969 by using a hot

filament to thermally activate the process gas [Der75] [Der76]. Beside the fact that the Russian group was able to deposit non-diamond substrates such as copper, they successfully combined the cyclic growth and etching procedure in one process step. These experiments have been ignored internationally except in Japan where the experiments were repeated and published in detail. A translation of the original works of Deryagin, Spitzin, Fedosayev et al. has been made available in [UCF89].

The deposition of diamond films with deposition rates of 1 µm/h was first reported by a research group of N. Setaka et al. at the National Institute for Research in Inorganic Materials (NIRIM) in 1981 for the hot-filament method [Mat81] and in 1982 for the microwave or radio-frequency activated plasma process [Kam82]. Additional methods of CVD-diamond deposition were found later, here only the synthesis of diamond by using a direct current (DC) arc plasma jet by K. Kurihara in 1988 [Kur88] leading to the high-rate deposition of diamond in CVD processes and applying an acetylene flame [Liu95] [Dis98] will be mentioned.

The works on diamond CVD deposition in our own workgroup goes back to the works of Haase in 1988 giving more than 20 years of experience in the low pressure synthesis of diamond films [Haa88].

A closer look on the mechanisms of CVD deposition of carbon films is taken in the subchapters of this section. A more detailed look on the industrially relevant deposition techniques of CVD diamond introduced here can be found in the following chapter.

3.1.2 CVD Deposition of Microcrystalline Diamond Films

The scientific understanding of CVD diamond deposition was not able to keep up with the rapid empiric-technical developments that were aiming directly at industrial applications and products for the diamond films. Processes were developed by a trial- and error approach regardless whether the physical-chemical backgrounds of the deposition were understood.

One of the first approaches to sort the variety of empirical data and combine them into one diagram was undertaken by P. K. Bachmann in 1991 (and in a modified way 1995) [Bac95]. In this diagram (Figure 3.2) the composition of the process gas used for diamond deposition was plotted with the edges of the triangle representing a 100 % concentration of hydrogen, carbon or oxygen. Any composition of process gases consisting of these three components is related to a specific position in the

diagram. By sorting available data for CVD deposition of carbon films into this diagram Bachmann was able to show that diamond deposition is only possible in a small regime within the so called diamond domain close to the CO axis.

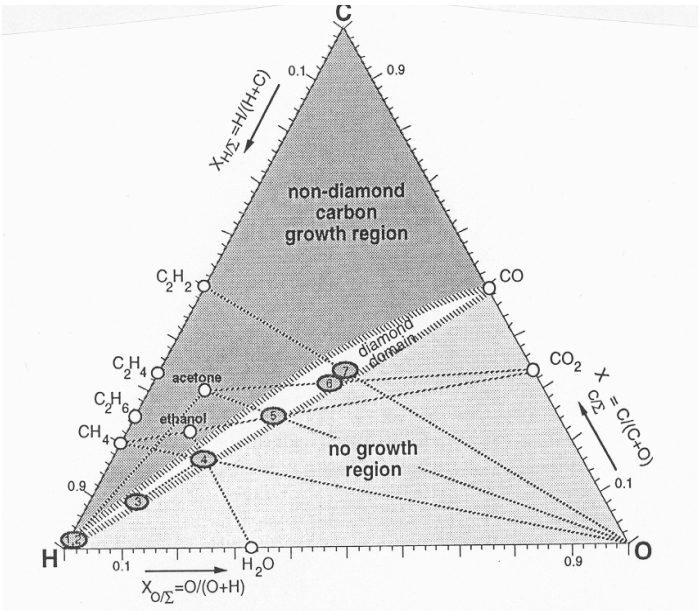

Figure 3.2 Bachmann diagram indicating the diamond domain [Bac95]

Below the diamond domain no deposition is taking place while above it non-diamond carbons are deposited.

However this diagram only gives information how the chemical composition of the process gas has to be in order to deposit diamond at all. It does not clarify the influence of traces of impurities in the process gas or the physical parameters on the microcrystalline diamond deposition. For example the crystal orientation in the deposited films is varied depending on the exact location within the diamond domain of the Bachman diagram and also by adding impurities to the process gas [Loc94].

Thus despite the fact that ambitious approaches were undertaken to theoretically explain the CVD diamond deposition many questions are still unanswered. Only few aspects of the deposition are widely accepted up to now. The atomic hydrogen for example is believed to be the key gas phase species driving the chemistry of diamond growth. The hydrogen fulfils several functions during the deposition in the gas phase as well as on the surface:

- Gas phase abstraction reactions
- Surface passivation

- Surface abstraction of hydrogen
- Surface etching of non-diamond carbon, e.g. graphite.

The gas phase abstraction reactions are necessary to activate the carbon carrier gas. The atomic hydrogen is the driving force in these processes by e.g. transforming the methane molecule into a methyl radical (one possible diamond growth precursor) by hydrogen abstraction [Law98]:

$$H_2 \rightarrow H + H \qquad \text{Equation 3.1}$$

$$H + CH_4 \rightarrow H_2 + CH_3 \qquad \text{Equation 3.2}$$

Another major role of atomic hydrogen in the deposition of diamond films is both the etching of non-diamond carbon bonds from the surface (e.g. sp^2-bonded graphite) and the temporarily stabilizing of the sp^3 growth sites on the surface by saturating the dangling carbon bonds [Goo93] [Hon97]. By releasing this hydrogen (for example by bonding to atomic hydrogen from the process gas) the carbon at the surface is chemically activated and can continue to grow by binding another carbon precursor. In fact the type of precursor is yet still discussed although it was tried to explain the diamond growth by including chemical reaction equation (e.g. [Fre91]). But although evidence was found that the methyl radical CH_3 [Har90] or the acetylene molecule C_2H_2 [Fre88] [Bel92] might be the precursor a uniform theory that is explaining the deposition process of CVD diamond is not found yet. Sternschulte et al. found different growth laws in different substrate temperature regimes [Ste06]. A square root dependence on the CH_4 feed gas concentration and a saturation for high methane concentrations in accordance with a methyl based growth mechanism was found for the growth rate at 800°C. At 1200°C the growth rate showed a linear relationship with the methane gas concentration and the C_2H_x mass spectrometer signal over more than one order of magnitude without any saturation behaviour up to methane concentrations of up to 20 %. This change of the growth law indicates an acetylene based growth mechanism at higher temperatures.

In the case of acetylene or methyl being the growth precursor the chemical equation for the diamond growth would be as follows:

$$C_dH + H \rightarrow C_d + H_2 \qquad \text{Equation 3.3}$$

$$C_d + C_2H_2 \rightarrow C_2H + H \qquad \text{Equation 3.4}$$

$$C_d + CH_3 \rightarrow C_2H + H_2 \qquad \text{Equation 3.5}$$

Here C_dH is the hydrogen-saturated carbon at the surface and C_d the reactive sp^3-bonded carbon on the surface of the growing film.

When modelling the CVD deposition of diamond the problem is not the gas phase chemistry that was investigated very soundly and a nearly complete understanding of the reaction processes of typical CVD environments was achieved [Lan94]. In fact much more work is needed investigating the surface physics and chemistry of diamond growth where a deeper insight into the none-equilibrium thermodynamics on the theory side, and sophisticated surface diagnostics at elevated pressures on the experimental side, are needed [Law98]. Yet still unresolved discrepancies between the numerous simulations and experiments indicate that essential aspects of the chemistry are not described properly by the models although some general agreements on the key steps exists as shown earlier. One attempt to overcome the lack of analytical techniques to probe the surface during CVD diamond deposition conditions was undertaken by Heerwagen et al. using IR visible sum frequency generation (SFG) [Hee01]. Surprisingly the group was not able to detect CH_3 species at the surface during the deposition process. The results were interpreted in a way that either other species such as acetylene are responsible for the growth or the CH_3 reacts so quickly that the concentration is below detection threshold. Since preliminary measurements at higher wavenumbers were not able to detect acetylene, Heerwagen presently favours the latter interpretation.

In the case that no carbon species can be proved to be the precursor for diamond growth other processes might be taken into account. Bibinov et al. for example established a growth model including charged radicals (ions) to participate in the deposition process of DLC films [Buc08a]. Growth models like this and some experimental findings are suggesting that charged radicals should also be taken into account for the deposition of diamond.

Within this work a detailed look at the theories of microcrystalline diamond deposition is not possible due to the variety and the lack of clarity. A comprehensive work on the models can be found in [Fre91] or [Heg96].

3.1.3 Nanocrystalline Diamond Films

The growing interest in nanotechnology and nanostructured materials has encouraged the research of diamond films with reduced grain size. By reducing the grain size those films feature rather unique combinations of properties making them potential materials for emerging technological developments such as Nano/Micro-Electro-mechanical Systems (N/MEMS) [Auc04] [Her04], optical coatings, bioelectronics [Yan02], surface acoustic wave (SAW) filters [Bi02], and tribological applications [Erd99]. The nanostructured films differ from the microcrystalline films in grain size and in roughness of the surface as shown in Figure 3.3.

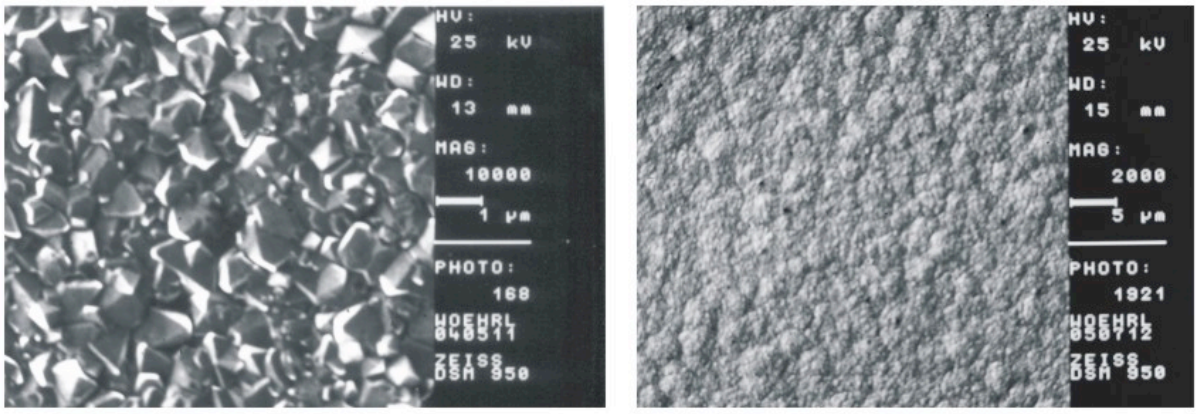

Figure 3.3 Morphological comparison of microcrystalline diamond film (left) and UNCD film (right)

The terms nano-crystalline (NCD) and ultra-nanocrystalline diamond (UNCD) were coined by the Argonne National Laboratory group that performed the pioneering works in this field [Gru99]. These terms were introduced to establish a differentiation to the microcrystalline diamond films that differ in film properties as well as in the way they are deposited. The technology developed at Argonne National Laboratory started from deposition of hydrogen free plasmas using fullerenes in Ar (Ar/C_{60}) and was thereafter extended to hydrogen diluted plasmas using Ar/CH_4 and gas mixtures containing only about 1 % hydrogen (either added intentionally or through the thermal decomposition of CH_4) [Gru99]. UNCD is grown from Argon-rich plasma giving it a very fine and uniform structure with grain sizes between 2-15 nm [Auc04]. The grain sizes are independent from the film thickness due to the high secondary nucleation of new growth sites during the whole deposition that is not taking place in the standard

van der Drift regime. UNCD consists of pure sp^3 crystalline grains that can be separated by atomically abrupt (0.5 nm) grain boundaries or embedded in a 3D matrix. The matrix in these films constitutes a large fraction of the overall film sometimes exceeding 10 % of the total volume giving those films a great proportion of non-diamond or disordered carbon [Auc04]. UV Raman spectroscopy [Zui96] and synchrotron based near-edge X-ray absorption fine structure measurements (NEXAFS) [Gru96] showed the presence of about 5 % sp^2-bonded carbon in a typical UNCD film.

In contrast NCD films are prepared from more conventional hydrogen-rich conditions resulting in grain sizes that scale with the film thickness due to columnar type of film growth in the van der Drift regime [Yan03]. Grain sizes of NCD films are usually between 50 – 100 nm [Auc04] although even grain sizes and film thicknesses of about 30 nm were reported [Wil06]. Due to the higher amount of hydrogen in the process gas and the thereby higher etching rate of sp^2 carbon during the deposition process NCD films feature less sp^2-bonded carbon in the grain boundaries compared to UNCD films. This can be advantageous for electrochemical applications where sp^2 carbon often reduces the electrode stability.

Just as for the deposition of microcrystalline diamond the mechanisms behind UNCD deposition are still discussed. Carbon dimers (C_2) are easily detected in UNCD plasma by optical emission spectroscopy [Gru95] and absorption spectroscopy [Goy98] and with the lack of atomic hydrogen needed to drive abstraction reactions in the gas phase and the surface it was proposed that the high reactive C_2 is the main growth species. By replacing H_2 with Ar in the process gas the fractional dissociation of H_2 becomes very high. One important reaction chain is [Law98]:

$$e^- + Ar \rightarrow Ar^+ + 2e^- \qquad \text{Equation 3.6}$$

$$Ar^+ + H_2 \rightarrow ArH^+ + H \qquad \text{Equation 3.7}$$

$$ArH^+ + H_2 \rightarrow Ar + H_3^+ \qquad \text{Equation 3.8}$$

$$e^- + H_3^+ \rightarrow H + H_2 \quad \text{or} \qquad \text{Equation 3.9}$$

$$\rightarrow 3H \qquad \text{Equation 3.10}$$

The partial equilibrium shifts toward carbon species that are stripped of hydrogen

$$C_nH_m + H \rightarrow C_nH_{m-1} + H_2 \qquad \text{Equation 3.11}$$

thus making the carbon dimer C_2 more important [Law98]. Although this has been supported by density functional calculations [Ste03], recent work [Zap02] has shown a very high-energy barrier for growth suggesting that the primary role of C_2 may be to trigger secondary nucleation. The combination of high plasma temperatures, high pressures and the presence of 1 % H_2 in fact make it likely that many species are present in the plasma, including CH_3, C_2H, C_2H_2 in addition to C_2 and some of these species could participate in the film growth [Xia04].

It is well accepted that the initial nucleation is one decisive factor for the subsequent CVD diamond film growth. While a low nucleation density can lead to van-der-Drift growth – known as the “survival of the largest” – high initial nucleation leads to shorter coalescence time and lower surface roughness. Due to the fact that substrate pre-treatment can significantly increase initial nucleation the pre-treatment is an important process step already predetermining the film properties [Liu095]. Three effective seeding methods are known: Mechanical scratching of the substrate surface (see e.g. [Er93] [Buc98], enhancing the nucleation by applying a bias voltage to the substrate in the early stages of deposition [Yug91], and ultrasonically activating the substrate in a suspension containing diamond powder (see e.g. [Lin06]). Nucleation densities of 10^{10}cm^{-2} or more were achieved with either of these methods. The latter method was used for the substrates in this work mainly for the good reproducibility and uniformity even for larger substrates of the method. Details on the pre-treatment and the deposition parameters used for the UNCD films deposited in this work are given in Chapter 4.5.

By reducing the grain size of microcrystalline diamond films the amount of material between the grains is increased. In fact the structure and density of grain boundaries or, better, the overall volume and structure of the film matrix significantly determine the properties of nanocrystalline diamond films. Thus, when comprehensively characterizing UNCD films one also has to analyze the matrix properties. Since the carbon atoms in the matrix have no crystalline configuration and are indeed amorphous, conventional techniques known from the analysis of amorphous carbon films can be used.

3.1.4 Amorphous Carbon Films

Amorphous carbon is the name used for carbon that does not have any crystalline structure. As with all glassy materials, some short-range order can be observed, but there is no long-range pattern of atomic positions. Depending on the structure and composition the amorphous films are roughly classified as a-C (general amorphous carbon), a-C:H (amorphous hydrogenated carbons), or to ta-C (tetrahedral amorphous carbon). Common properties of all these amorphous carbon configurations are e.g. chemical inertness, biocompatibility and lack of grain boundaries – other properties may be tailored in a very large extent like hardness (from soft to extremely hard), electrical conductivity (from good conducting to insulating), residual stress (from tensile to compressive), wettability (from hydrophilic to hydrophobic) or elasticity (more than one order of magnitude). [Buc06]

These types of carbon films differ in the sp^3/sp^2 ratio of bonded carbon and in the amount of hydrogen bonded in the film giving each structure very unique properties. The fact that the structure can be tailored, makes amorphous carbon a whole class of materials. In 2006 the Association of German Engineers, VDI, issued an authoritative report VDI 2840 [VDI06] in order to clarify the existing multiplicity of confusing terms and trade names for amorphous carbon films. The VDI 2840 report confirmed the utility of locating a particular DLC material onto a 2-dimensional map on which the X-axis described the fraction of hydrogen in the material and the Y-axis described the fraction of sp^3-bonded carbon atoms (nowadays usually as a triangular phase diagram).

But even with a fixed sp^3/sp^2 ratio and hydrogen fraction in the films the DLC material can differ by the specific configuration of the sp^2 phase giving another degree of freedom when tailoring film properties. The sp^2 bonds can appear in ring or in chain structure also influencing film properties.

A mechanism behind the formation of the amorphous films and the formation of different sp^2/sp^3 configurations was proposed by Robertson and Lifshitz and is based on the fact that sp^3-bonded carbon films are denser than sp^2-bonded films. Robertson proposed that a metastable increase of density is created by subplantation during film growth causing the local bonding to change to sp^3 bonds [Rob93] [Rob94]. Robertson was able to show that the formation of sp^3 sites strongly depends on the ion energy of the impinging particles.

A more detailed look at the growth models of amorphous carbon can be found in [Rob02].

3.1.5 Special Carbon Configurations

For a long time diamond, graphite and amorphous carbon films were the main carbon configurations known (see [Haa88] for a more detailed look) until Robert Curl, Harold W. Kroto and Richard E. Smalley discovered cage-like molecules like the C_{60} in 1985, which is also known as buckyball. 1991 Sumio Iijima reported another structure; a one-atom thick sheet of graphite (called graphene) rolled up into a seamless cylinder with diameter of the order of a nanometre: the carbon nanotube. Besides these tubes that are made up of single graphene sheets (single walled) there are also multi walled tubes that consists of multiple layers of graphene rolled in on them to form a tube shape. Those nanotubes can even be closed up at the ends with half of a buckyball.

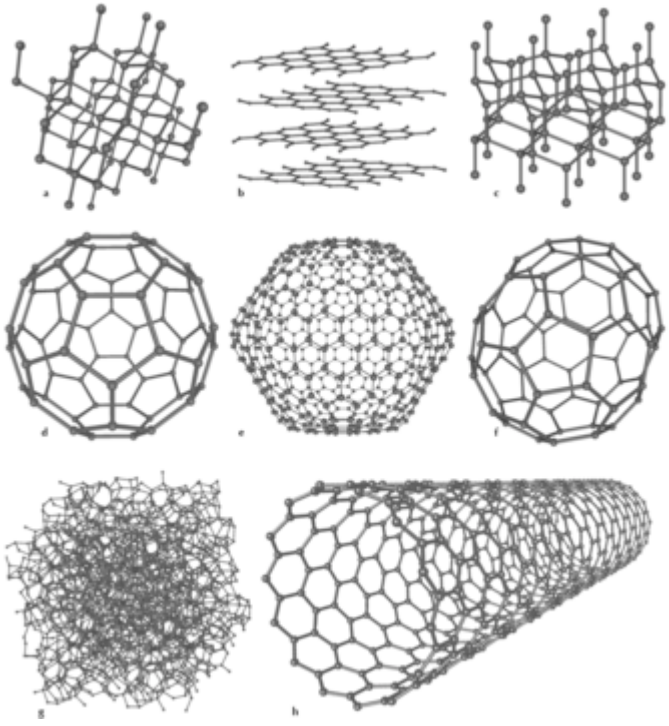

Figure 3.4 Eight allotropes of carbon: a) Diamond, b) graphite, c) Lonsdaleite, d) C_{60}, e) C_{540}, f) C_{70}, g) amorphous carbon and h) carbon nanotube [WIK07]

3.2 Thin Film Deposition

The ever-changing and demanding field of material science is in constant search for new materials with specific properties or even combinations of specific properties.
The reason for this is the great demand for products that are supposed to combine multiple – sometimes even complementary – material properties. One striking example is tools that should be hard and tough at the same time. In fact this combination can't be found in any known material. However by taking a closer look at the requirements for a product it sometimes comes out that only the bulk material has to be tough and it would be sufficient when only the surface is hard. This can obviously be achieved by coating a tough base material with a hard coating. In many cases already thin films with thicknesses of some micrometers or even below are sufficient to give the base material a completely different surface performance. Techniques that allow the deposition of such thin films are summarized with the term "thin film technology".
In the past years many methods to produce thin films on surfaces have been developed which use plasma assisted physical (PVD) or chemical (CVD) vapour deposition. Variation of the physical parameters involved in these deposition processes may change the properties of the deposited films dramatically. A proper control of the deposition process is therefore necessary to allow the tailoring of desired film properties.

3.2.1 Process Modelling

The most decisive criterion to evaluate the film quality is ultimately the film performance for a given application. To achieve this goal usually a trial and error approach is used by industry to get the desired macroscopic properties of a product. In the same way most of the industrially utilized processes of thin film deposition technology were developed in a more or less "empirical" way. Accordingly a deep understanding of the fundamental physical processes during thin film deposition is missing up to now in many areas. To optimize the currently used or develop new and innovative methods for film deposition a physical understanding of the deposition process is necessary. This is a major part for the fundamental science of thin film technology.

The variety of parameters that need to be considered is shown in Figure 3.5 where the influencing variables are sorted in a flow diagram [Buc93].

On the atomic level the film properties of a film are determined by the properties of the substrate surface on the one hand and the flux of the condensating particles on the substrate on the other hand. The problem is that mostly these microscopic parameters are not known and not easily accessible. The knowledge is limited to macroscopic available properties such as the substrate material, the substrate pre-treatment or process parameter such as the voltage and the current of the plasma generator or of the evaporator. However to optimize the deposition methods it is necessary to have a deeper understanding of the physical background of the processes.
To quantitatively understand the connection between the function-specific properties of the films and the process parameter of the deposition it makes sense to subdivide the process into separated successive steps [Buc93] as shown in Figure 3.5 and understand how the specific steps contribute to the film properties.

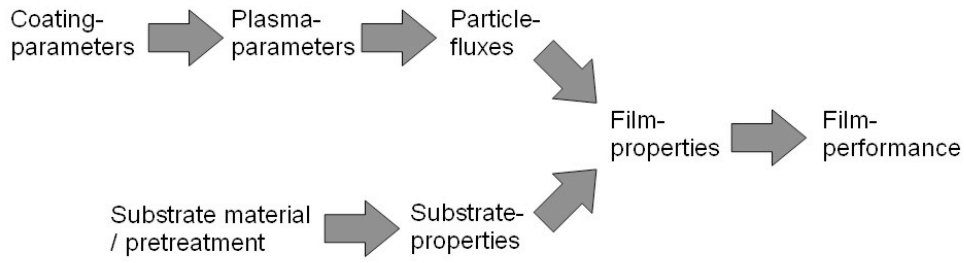

Figure 3.5 Scheme of modelling thin films [Buc93]

The – microscopic – film properties thus depend on the one hand on the substrate properties (lower branch in Figure 3.5) and on the other hand on the particle fluxes interacting with the substrate (upper branch in Figure 3.5). To reach the ultimate goal, that is to tailor film properties, it is therefore essential to know and to control the physical properties of the particle fluxes interacting with the substrate surface. In detail to characterize the deposition process the type of the condensating particles (atoms, molecules, ions, neutrals) as well as their state of excitation (kinetic energy, potential energy) must be known. Beside these parameters the properties of the substrate (substrate material, substrate surface condition, and substrate

temperature) need to be taken into account. One particular example for the complexity of the influence of these process parameters on the film properties during diamond deposition is the grain size in the deposited films. The nucleation density can vary it significantly – either by direct substrate surface treatment or by selective adjustment of the particle fluxes.
To characterize a deposition process at least the following parameters should be known:

- The deposition rate, the number of neutral and ionized atoms to condense on the substrate per cm^2 and second *(overall particle flux)*
- The ratio of ion flux and overall particle flux
- The energy of the condensing particles and
- The film thickness after the deposition.

Beside these parameters that are determined by the deposition process the substrate properties need to be taken into account:

- Substrate material
- Substrate surface properties and
- Substrate temperature.

Already this simplified view reveals that a variety of variables need to be considered, which results in a very complex and difficult to control system when interacting with each other. Moreover often so-called hidden parameters also influence the deposition process. These are unknown influencing variables whose relevance is only realized after long experimental series like for example specific impurities of the materials used or the process gas [Buc86].
The role of physical modelling is to describe the interaction of all these parameters. Since technical advances were recently achieved in plasma analytics as well as in surface and film analytics new methods are available to succeed in this task.

3.2.2 Film Growth

The predominant method for the deposition of thin films is a growth process where the film is built up by single particles (atoms, molecules or radicals). In doing so the properties of the deposited film are essentially influenced by the physical-chemical parameter of the deposition process. The ultimate ambition of current fundamental research is to understand the mechanisms behind the deposition of thin films – to eventually control the deposition process in a way that the resulting films have the desired properties. A real understanding of the mechanisms leading to the deposition of thin films would give the chance for the selective design of films with desired properties instead of just depositing films in a trial- and error kind of way mostly done in industry up to now. With this the tailoring of a specific deposition process for the requested properties could be realized. The present state of research in the field of modelling the crystal growth can be found in [Mic04] [Kru07].
The following steps generally describe the film growth on the substrate surface by the impinging particle fluxes:

- Occupation of the substrate surface with single atoms
- Diffusion of these adatoms on the surface to preferential locations
- Assembly of adatoms to groups of atoms (nuclei)
- Growth of the nuclei to a closed film
- Growth of the film

The atomic processes behind these steps of film growth are shown in Figure 3.6. Beside the process of particle adsorption at a substrate terrace, the forming of nuclei by bonding of identical particles (homogeneous nucleation), the adsorption of particles at substrate defects (heterogeneous nucleation) and desorption of adatoms in the gas phase are displayed.

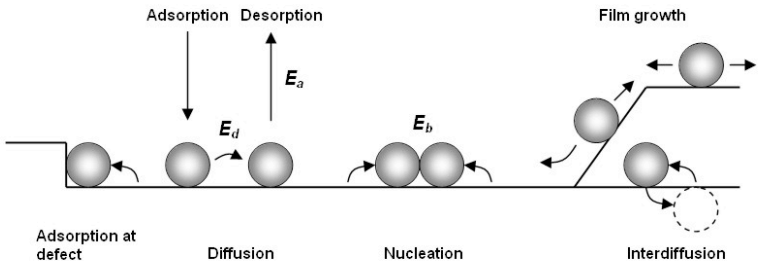

Figure 3.6 Microscopic processes and the characteristic energies during nucleation and growth of thin films

The different ways of film growth illustrates Figure 3.7. The Vollmer-Weber-growth (3D Island growth) describes the growth of the film by coalescence of islands. A second mode of film growth is the layer-by-layer growth (Frank van der Merwe) where the film is growing parallel to the substrate surface and stops building out islands already at a very early stage of film growth. The combination of these two growth modes leads to the Stranski-Krastanov Growth [Bau58a] [Bau58b] [Gre02].

Coverage / Mechanism	Θ < 1 ML	1 < Θ < 2	Θ > 2 > ML	Examples
3-D Island Growth / Vollmer-Weber		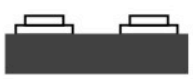		Metals on a-SiO_2
2-D Layer by Layer Growth / Frank van der Merwe				Si/Si, GaAs/GaAs
Stranski-Krastanov Growth				In/Si, Ag/Si, Ge/Si

Figure 3.7 Film growth modes

Necessary for the nucleation of the adatoms is a sufficient mobility of the particles after the adsorption of the atoms on the surface (“wettability”) so that an agglomeration at a substrate defect or an assembly of adatoms can occur [Mic04]: if the atoms of the deposited material have stronger attractive forces among themselves than between substrate atoms and film atoms the condensated particles tend to island growth. In the opposite case layer by layer growth is likely to occur. Furthermore adatoms diffusing on an upper terrace require additional energy to cross descending step edges. This additional energy is called Ehrlich-Schwoebel barrier that leads to the 3-D Island Growth shown in Figure 3.7. [Sch69].

Generally plasma assisted methods for thin film deposition support the formation of a closed film at early stages of film growth preventing the formation of raised islands that would coalesce later. Through this the formation of rough surfaces can be reduced.

The coherences between film growth and the mechanical properties of the deposited film is shown by a growth model by Windischmann [Win92] on the basis of mechanical stress forming in the growing film. This example shows how a material with identical chemical composition can have different mechanical properties depending on the methods of deposition. Most optical, mechanical and chemical properties depend on the microstructure of the material in the same way.
Due to the technical relevance of residual stress in thin films the formation of stress is discussed in the following chapter in more detail.

3.2.3 Residual Stress in Thin Films

A crucial parameter in the application of thin films is the residual stress in the films. High stress in films counteracts the adhesion and can lead to failure of the films. Failure of thin films can mean that the film is delaminating from the substrate or in other cases the residual stress leads to cracks in the films limiting their functional capability. Figure 3.8 shows these two effects of residual stress in thin films. Figure 3.8 (left picture) shows a DLC film that was delaminating because of high compressive stress, the right picture shows a UNCD film with cracks due to high tensile stress.

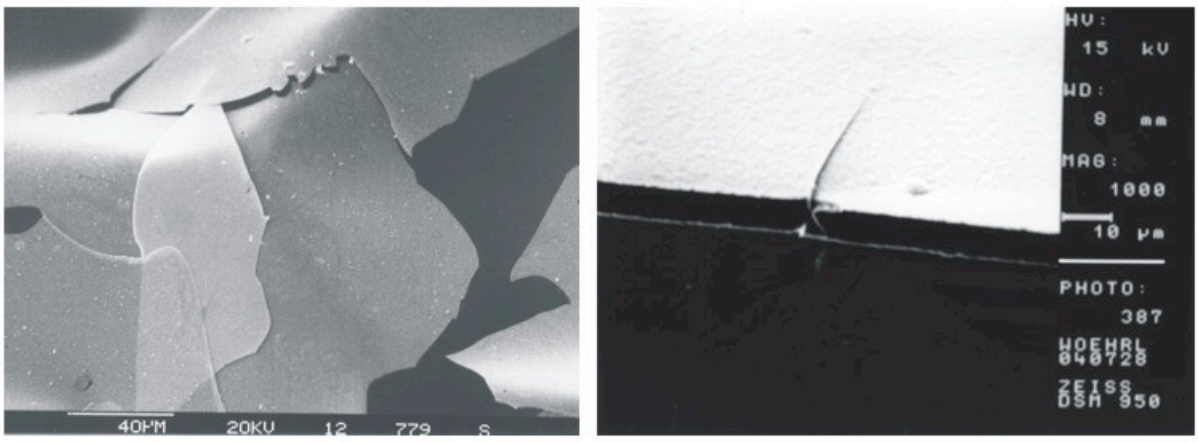

Figure 3.8 Residual stress in thin films. Compressive stress in DLC (left) and tensile stress in UNCD film (right)

But also less dramatic effects make the investigation and control of the residual stress an interesting field. For instance physical properties (optical, electrical, magnetic) can be influenced by residual stress in the films.

First works investigating the residual stress in thin films were performed by Stoney [Sto09] at the beginning of the last century. Depositing metal films on substrates by electrolysis he observed, that the films started to develop cracks and peel off the substrate when exceeding a specific film thickness. By systematic investigations he not only found out that the residual stress is scaling with the film thickness but he also found a way to measure the stress. With respect to the so-called Stoney equation it was possible to quantitatively determine the residual stress from the stress-induced curvature of the substrate. Up to now his method, based on the measurement of the bending of the substrate, is used in various methods to measure the residual stress in thin films.
It should be noted here that spectral methods of determining stress for example from the shift of Raman peaks or the shift and broadening of lines obtained by X-ray diffraction measurements can measure the stress in the crystalline grains but not the contribution from the matrix thus making these methods valuable to obtain additional information about the stress in the films but not necessarily to obtain the overall stress in the films. Furthermore the possible application of these spectral methods is of course limited when used for nanostructured materials, because the small crystals in films lead to a broadening of the spectral lines and therefore limit the accuracy of the methods.

Mechanical stress in thin films arises from different effects, that are due to the properties of the materials used on the one hand, and due to the process parameters of the deposition itself on the other hand.
The residual stress in thin films is the sum of three components – the thermal stress σ_{th} the intrinsic stress σ_{in} and the stress due to a lattice mismatch σ_{lat} of the growing crystal and the substrate lattice.

$$\sigma = \sigma_{th} + \sigma_{in} + \sigma_{lat} \qquad \text{Equation 3.12}$$

The thermal stress σ_{th} arises from the differences of thermal expansion coefficients of substrate and film material with the elevated temperature during the deposition. After deposition the substrate is cooled down to the ambient temperature and both the substrate and the film contract according to their thermal expansion coefficients.

When the two materials have different thermal expansion coefficients they contract differently resulting in residual stress in the film just as known from Bimetals. This stress component can be calculated [Win91] [Woe06a] by

$$\sigma_{th} = E_f(\alpha_f - \alpha_S)(T_B - T_M). \qquad \text{Equation 3.13}$$

In this equation E_f represents the elastic modulus of the deposited film, α_f and α_S the mean values for the thermal expansion coefficient of the film and the substrate respectively and T_B and T_M the temperature during the deposition and the stress measurement. Thus with known material constants one can calculate the fraction of the thermal stress of the residual stress in the film.

The lattice mismatch effect is due to a small difference in the lattice constant of the growing crystal and the lattice of the substrate. By distortion of the lattices a strain is building up in the films. In the case of UNCD films as investigated in this work this effect can be neglected because the films are nanocrystalline and not growing heteroepitaxial. In the case of monocrystalline or even large microcrystalline diamond films on silicon this effect can have an influence and needs to be considered.

3.2.3.1 Grain Boundaries Mismatch Model

The intrinsic part of the residual stress consists of two independent contributions. The “grain boundaries mismatch model” [Hof76] describes the origin of tensile stress in films: In the early steps of the deposition only isolated nuclei grow on the substrate. At these nuclei the film growth will take place, till the isolated growth zones get in contact with each other. At this point it is improbable that the gap between two growth zones is exactly of the size of one atom. More probable is a gap that is slightly bigger than one atom diameter. Because a closed film surface is energetic more preferable for the film the atoms attract one another to close the gap. This process leads to attractive forces between the atoms that result in tensile stress in the film. Figure 3.9 graphically shows this effect and the bending of a substrate that was coated with a film under tensile stress.

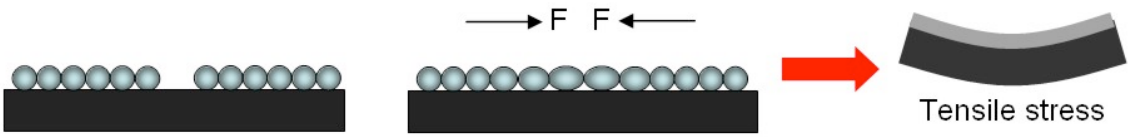

Figure 3.9 Evolution of tensile stress in thin films

One can deduce from this “grain boundaries mismatch model” that the arising tensile stress must be proportional to the reciprocal grain size of the film. The tensile stress thus gets bigger the smaller the grain size is, making this efect a dominant one when depositing nanostructured films. This fact has to be considered, especially when the grain size can be varied by the process parameters and the residual stress be tailored by this.

It should be mentioned here, that a variation in grain size as a function from the distance from substrate to film surface, e.g. by selective grain growth (van der Drift), can course stress gradients in the film [Gra05].

3.2.3.2 Ion-Peening Model

In contrast to the prior model the “ion-peening model” describes the origin of compressive stress in films, especially occurring in ion-assisted deposition of thin films [Win87].

When high energetic particles bombard an already deposited film surface they do not necessarily condense on the surface, but penetrate, depending on their energy, into the film. In doing so the already deposited film can get densified and compressed. The resulting compressive stress is therefore strongly depending on the energy of the impinging particles and can easily be adjusted by this parameter. Figure 3.10 schematically shows this process and the influence on the curvature of the substrate.

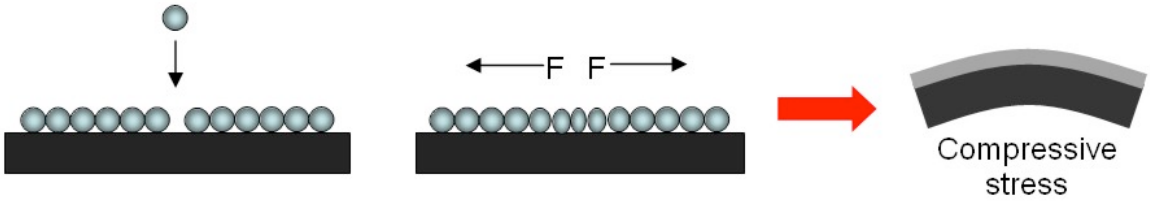

Figure 3.10 Evolution of compressive stress in thin films

Compressive stress caused by implanted atoms is associated with increased strain energy due to the overdensified structure in the film. This energy can be released when the bombarding particles transfer a significant fraction of their kinetic energy to motion of the atoms in the area of the impact. This local heating, or “thermal spike” [Mul86a] can provide the energy necessary to overcome the densified state of the film and lead to a relaxation of the film. Bombardment of films under high compressive stress with energetically high particles will lead to an “annealing” and the resulting films will have less or even no stress at all [Dav92].
Muller [Mul86b] has even predicted for large energies that the film density will be reduced because of sputtering of atoms from the surface of the growing film. The resulting voids can than even lead to tensile stress in the films [Mul86b].

The evolution of residual stress in thin films as described by the grain boundary mismatch model and the ion-peening model is outlined in Figure 3.11 as a function of the ion energy.

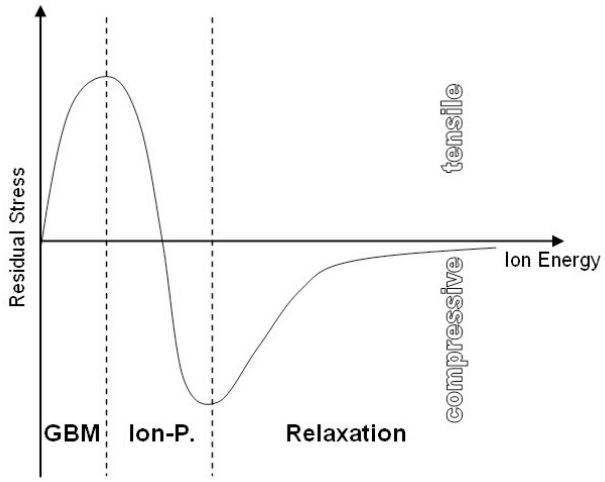

Figure 3.11 Residual stress as a function of the ion energy as described by the grain boundary mismatch model (GBM) and the ion-peening model (Ion-P.)

For low ion energies the residual stress is dominated by the effects described by the grain boundary mismatch model and the stress is tensile. For higher ion energies the growing film gets more and more densified and a compressive stress is developing. When the impinging particle energy extends a certain level the compressive stress is relaxed again by annealing effects.
Compressive stress is by definition negative while tensile stress is positive.

3.3 Deposition Methods

Gas-phase activation above the substrate surface is necessary to deposit CVD diamond at reasonable growth rates. The various CVD methods differ mainly in the way the gas-phase activation is achieved. The methods can be classified in three basic methods [Liu95]:

1. External heating (as in hot-filament CVD) [Mat82a] [Mat82b] [Hau93]
2. Plasma activation (as in plasma assisted CVD) [Kam83] [Sai86] [Mat87a]
3. A combination of thermal and chemical activation (as in flame CVD) [Hir88] [Han88]

The industrial applicability of a method strongly depends on the growth rate and the scalability of a process.

The gas-phase temperatures reached with these CVD methods is one of the most decisive factors for the growth rates during the deposition.

A comparison of the linear deposition rates for the different CVD methods (Figure 3.12) shows that the rates positively correlate with the gas-phase temperature reaching up to 1 $mm \cdot h^{-1}$ in atmospheric pressure plasma arc-jet CVD with temperatures above ca. 5000 K [Bac91].

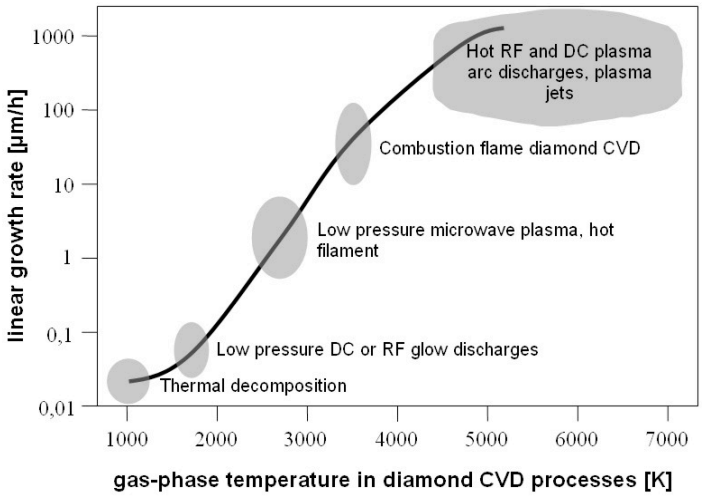

Figure 3.12 Linear growth rate as a function of gas-phase temperature [Bac91]

Angus et al. indicated that linear growth rates in different diamond CVD processes increase approximately linearly with the areal power densities employed [Ang89] as shown in Figure 3.13.

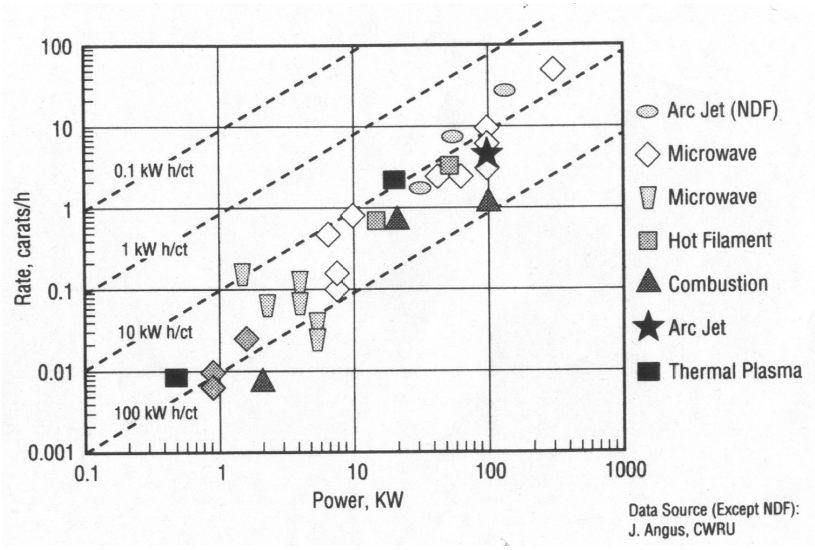

Figure 3.13 Growth rate as a function of power [Ang89]

In the following three different deposition methods are introduced in more detail. The Hot-Filament CVD method because it was historically one of the first and is still one of the most common principles used both in industry as well as in laboratory conditions, the dc-arc method and the microwave method as representatives of high rate deposition methods.

3.3.1 Hot Filament

HFCVD deposition of diamond [Der76] [Mat82b] [Kam83] is most probably the simplest way to grow diamond at low pressures. In a HFCVD process the process gas (typically 0.1 – 4 vol. % methane in hydrogen) is fed into a vacuum chamber at a pressure of usually 1 – 200 mbar and flows across a wire or mesh made of metals such as W, Ta, Mo or Re heated up to temperatures between 2000°C and 2400°C [Liu95]. Thermal activation of the process gas is leading to the formation of methyl radicals etc. (see Chapter 3.1.2) and additionally a part of the H_2 is dissociated into atomic H allowing diamond to deposit on a substrate. Deposition rates of up to 20 $\mu m \cdot h^{-1}$ were reported with this method.

Though the HFCVD process is still widely used for the deposition of diamond both in laboratory conditions as well as in industry the method has some limitations associated with long-term stability of the filament and the contamination of the growing film caused by evaporating metal from the filament. An up scaling of the process has been done up to areas of ca. 100 cm x 50 cm [Con07] although it is not

easy because uniform temperature distribution on the substrate need to be realized to obtain good film quality [Hau93].

3.3.2 DC-Arc

The name DC-arc is due to the fact that a DC electrical arc discharge between two electrodes is used to dissipate energy into the process gas. In 1988, Kurihara et al. [Kur88] first reported the use of the DC plasma arc-jet CVD method, in which methane was mixed into an H_2/Ar plasma jet at around 200mbar. The sudden expansion of the gases into the reactor chamber as they are heated by the plasma arc gives rise to the formation of a high-speed arc-jet. At the high plasma temperatures (>5000 K) a large amount of the hydrogen is dissociated and a sufficient supply of the active carbon precursor is created. The highest deposition rate recorded is 930 µm/h and has been achieved using DC plasma jet CVD by Ohtake and Yoshikawa [Oht92] and thick deposits are routinely produced. [Mat92] [Liu95]

Despite the fact that the linear deposition rates are unmatched by any other deposition method, the deposited area is rather small for the usual dc-arc systems (some square cm).

The works of Akatsuka, Böhm, and Meyer [Aka88] [Böh94] [Mey00] showed the applicability of a dc-arc for diamond deposition where the process gas was laterally introduced into the arc. The setup is comparable to the one of HFCVD whereas the arc between the electrodes is used as a filament substitution. It was possible to enlarge the coated area with this setup compared to the conventional dc-arc. One can clearly see now that the coated area depends on the length of the dc-arc. To increase the cost effectiveness and the applicability it is desirable to increase the length of the arc. Two technological problems arise with this task:

- The ignition voltage needs to be technically controllable
- The arc needs to be stabilized

Although attempts were taken to increase the deposition area for the DC-arc (for example [Lan98] [Kar96] [Woe03]) the scalability of the method is still a challenge.

3.3.3 MW-CVD

Besides the HFCVD the microwave plasma assisted CVD (MW PACVD) is the most frequently used technique for diamond growth. In MW PACVD the process gas is introduced into a reactor and Microwave power is then coupled into the chamber through a dielectric window in order to ignite a plasma.

Research on MW PACVD started with the pioneering works of Matsumoto and his group in the early eighties [Mat81] [Kam83] and further work by Bachmann led to a commercial product (ASTeX). A major step forward was the geometrical stabilization of the plasma by suitable resonator designs like coupled resonators with multi-antenna configuration [Sun04], the “Koidl-egg” [Wil99] or the “Cyrannus” source [Cyr00].

3.3.3.1 CYRANNUS®-Principle

Plasma processes can be made more effective by decreasing the process time or increasing the size of equipment. Both lead to higher production quantities in a system. While increase of size is commonly used for multi-mode plasma and RF plasma processes, the increase of process speed was limited in the relation between pressure and spatial homogeneity of the plasma.

The concept of cylindrical resonators with annular slots (CYRANNUS) allows the increase of diameter and volume as well. The power coupling concept and a change of wavelength enables such modifications. The microwaves are fed into a ring resonator by an outer waveguide and coupled into the cylindrical resonator of the reactor with slot antennae. A cylindrical resonator with the preferential TM_{012}-mode enables the generation of a freestanding centric plasma in the quartz cylinder. The top- and the bottom-side of the plasma source (Figure 3.14) can be designed accordant to the requirements. By that it is possible to install for example a process gas supply directly on top of the substrate, an electrode for bias enhanced nucleation or probes for plasma diagnostics. The substrate holder, which is usually inserted into the reaction chamber from the bottom, can be custom designed. Depending on the deposition process it can be equipped with an additional heater or cooling. In conjunction with high gas flows, which are possible at medium pressure operation, the sources show very high performance and fast processing speed due to larger

amounts of available active species in the plasma. The highly effective production of hydrogen radicals is known to be essential for very high quality diamond deposition with microwave-excited plasmas. Since the critical ion density of plasma is a function of the exciting frequency, this shows the limit for the plasma generation.

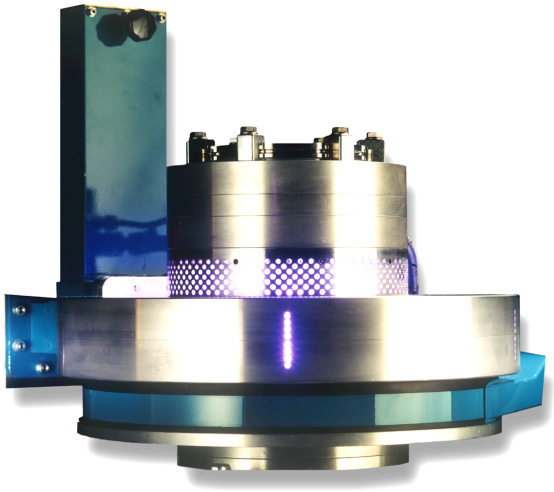

Figure 3.14 CYRANNUS® Plasma source

3.3.3.1.1 Scaling of Microwave Plasmas

The size of the generated plasma is an essential parameter for a cost-effective production. A scaling of microwave technology however is limited when high demands on the quality are made. Two attempts for upscaling microwave technology were done for CYRANNUS® plasma sources and should be briefly shown here to show the industrial feasibility for UNCD film deposition by CYRANNUS® plasma technology.

A rather simple solution for the enlargement of microwave plasma sources is scaling the device to another excitation frequency. The most commonly used microwave frequency is 2.45 GHz. In addition a frequency of 915 MHz is also available for example. Both frequencies are used for a long time for industrial heating treatment or for vulcanization of rubber. Hence the commercially available components are not only sophisticated but also inexpensive.

To excite a plasma source with a customized frequency it is necessary to adapt the whole construction including the periphery to the new frequency. The scaling is

performed linearly with the wavelength. Starting for example with a 2.45 GHz setup, all dimensions need to be enlarged by a factor of 2.68 when going to 915 MHz. That will convert the 6” diameter plasma source into a 16” diameter plasma source using the longer wavelength.

But just mechanical resizing of the plasma source doesn’t necessarily result in enlarged plasma. In high vacuum environment this is true because ions and radicals are distributed uniformly due to long mean free paths and small amounts of collisions. At higher pressure, and thus shorter mean free path, the plasma is located in regions with highest electrical field. Thereby only with a homogeneously spread electrical field the result is a bigger plasma ball.

Power feeding into a plasma chamber via a single antenna (as performed in the ASTeX reactor) shows a strong impact on the electrical field from the near field of the antenna. For 2.45 GHz and a power beyond 3 kW per antenna the near field tends do dominate over the mode structure of the resonator. Subsequently the plasma shifts more into the direction of the antenna until it finally may damage the dielectric window.

In the case of the CYRANNUS® principle the scaling up can be achieved by superposition of the TM_{012}-mode in the resonator with the radial arranged near field of the microwave coupling. First studies of the 915 MHz plasma source show that the performance is analogous after scaling up compared to the 2.45 GHz system.

An inverse scaling was already shown for the CYRANNUS® principle by exiting the plasma with 9.55 GHz a few years ago. Although the dimensions become very small, the advantage of this configuration is the increased ion density at this frequency. The switch of the microwave frequency to 915 MHz is one possibility to overcome the limitation of size, but it enables only an increase of all dimensions by a factor of 2.7 [Buc04].

By introducing a multi-antenna plasma source combined with a resonator it became possible to enlarge the plasma source also by increasing the number of antennas.

If the number of coupling sites is increased in a plasma source, only the diameter of the source is increased and the plasma assumes a spherical shape or a flat disc.

Starting from an excitation frequency of 2.45 GHz plasma sources with 2.7’’, 6’’ and 10.5’’ diameter respectively were already built. For all cases the applicability up to atmospheric pressure was demonstrated. The homogenity can be demonstrated by the quality of deposited diamond films. It was shown that the plasma sources with

plasma size of 6'' are capable of coating 4'' wafers with a uniformity of ± 30 %. With the 10.5'' sized plasma source up to 8'' wafer were coated. Since there is no limitation to a specific wavelength this scaling could also be realized with the 916 MHz source [Buc04].

3.4 Diagnostics

According to Figure 3.5 it is evident that it is necessary to measure and control the plasma and the substrate properties during film deposition to achieve the goal of tailoring specific film properties. The most important methods used in this work are shown in the following.

3.4.1 Plasma Diagnostics

It is important to acquire as many parameters involved in film deposition as possible directly during the process (in-situ) to understand the connection between deposition parameters and the resulting film properties. One problem for some in-situ diagnostic methods is that the elements of the diagnostic device are also coated during the deposition process resulting in false readings. Another problem can be that the elements of the diagnostic are interfering with the plasma limiting the possibility to measure the plasma properties right inside the plasma.
The two methods used in this work for plasma diagnostics do not have these drawbacks because both - the optical emission spectroscopy and the mass spectroscopy - measure the plasma properties without interfering with the plasma.

3.4.1.1 Optical Emission Spectroscopy (OES)

Emission spectroscopy is a spectroscopic technique that examines the discrete photon emissions of the plasma. Atoms or molecules in the plasma first absorb energy, exciting electrons to higher energies to then radiate this energy as characteristic emission (photons of a particular wavelength) as the electrons fall back to lower energy levels or by collisions. The emission spectrum of an atom or molecule consists of several emission lines, each corresponding to a specific electron transition.

The C_2 carbon dimers are believed to be one of the important species for deposition of nanocrystalline diamond films and fortunately the plasma properties and C_2 density explicitly can be measured by optical emission spectroscopy. Though the simplicity of OES makes it a popular method for plasma diagnostics, usually the emission intensities alone provide only limited insight into the plasma parameters. The reason for that is that the emission intensity depends strongly on both, exitation and nonradiative deexcitation rates as well as radiative decay rates and therefore does not give direct information on ground state species concentrations. Fortunately Goyette et al. were able to find a linear correlation between the optical emission intensity of the $d^3\Pi \rightarrow a^3\Pi$ (0,0) vibrational band of the C_2 Swan system with the absolute C_2 concentration in $Ar/H_2/CH_4$ plasma [Goy98]. These absolute C_2 concentrations were obtained by white-light absorbtion spectroscopy. The results confirm the reliability of the (0,0) Swan band for relative determination of C_2 density with high sensitivity under conditions used for hydrogen-deficient plasma-enhanced chemical vapour deposition of diamond used for UNCD.
Figure 3.15 shows an OES spectrum taken during UNCD deposition indicating the strong emission lines of the C_2 dimer, the Fulcher α band of H_2 and the H_α line.

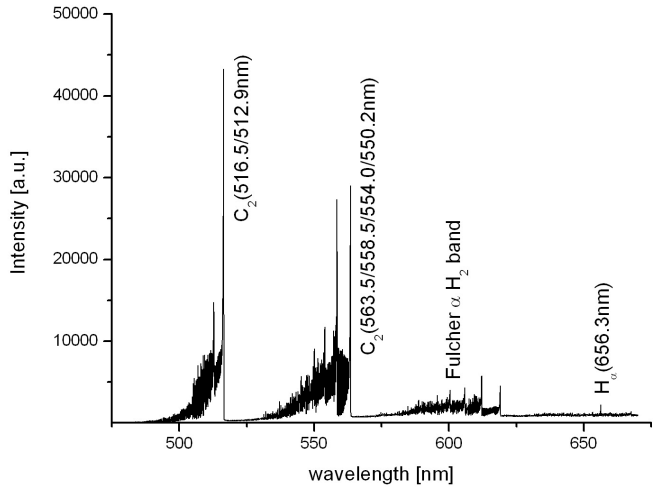

Figure 3.15 OES spectrum of UNCD CVD plasma

Beside the function as plasma monitor to control the plasma compositions the OES spectra were used to measure the plasma temperature. A local thermal equilibrium is assumed for the analysis of the spectra because in doing so the electron excitation

temperature of the plasma can be obtained from the ratio of the Hydrogen Balmer Lines by resolving

$$\frac{I_1}{I_2} = \frac{g_1 A_1 \nu_1}{g_2 A_2 \nu_2} \exp\left(- \frac{E_1 - E_2}{k_B T} \right) \qquad \text{Equation 3.14}$$

Here I_i is the line intensity and g_i its degeneracy, A_i are the Einstein coefficients, ν_i the excitation frequencies and E_i the excitation energy (values taken from [Wie66]). The H_α and the H_β line intensities were used in this work.

The spectra in this work were obtained by a Jobin Yvon HR 460 spectrometer that was coupled to the process chamber via a glass fibre.

3.4.1.2 Mass Spectrometry

Mass spectrometry is an analytical technique used to measure the mass-to-charge ratio of ions. Here it is used to measure the chemical composition of the process gas during the deposition process.

Although Goyette et al. found the feasibility of OES for plasma analysis during UNCD deposition, comparative studies were also done by mass spectroscopy. The intensity of the carbon dimer (mass number 24) was taken from the mass spectra and compared with the results obtained by OES.

A detailed investigation of the plasma processes during nanocrystalline diamond deposition from $Ar/H_2/CH_4$ can be found in [Zho06]. By investigating the plasma with quadrupole mass spectroscopy and optical emission spectroscopy Zhou et al. were able to find an explanation for CH_4 decomposition in hydrogen-poor plasmas, in these plasmas electron impact seems to be mainly responsible for the CH_4 dissociation other than hydrogen abstraction with atomic hydrogen.

The mass spectrometer used in this work is a Balzers Prisma QMS 200 Quadrupol mass spectrometer.

3.4.2 Film Diagnostics

The analysis and characterization of films and surfaces is due to the complexity of the methods used and the special knowledge needed for the evaluation of the data a

separate field of research by itself with a great variety of methods. A detailed description of all available methods to analyze film properties is not possible within this work but the methods used to investigate the diamond films should be briefly introduced and classified in this chapter.

Despite the variety of methods three standard methods for identification and classification of microcrystalline diamond have been established [Mes87]: The scanning electron microscopy to reveal the crystalline morphology of the diamond films, the Raman-Spectroscopy to identify the characteristic diamond lines in the spectrum and the X-ray diffraction to detect the crystalline structure of the film.

The application of all these methods becomes difficult for nano- and ultrananocrystalline films because all the mentioned features of the conventional analysis (morphology, characteristic diamond Raman-line and the diffraction patterns) get weaker or are broadened with the reduced grain size.

The fact that the volume of the crystals is reduced and the surface of the crystals and the film matrix play an increasing role for the film properties makes the analysis of nanocrystalline diamond films an even more challenging task. The combination of traditional analyzing techniques for (microcrystalline) diamond and methods for the analysis of amorphous carbon films is therewith necessary.

The methods can be categorized in five groups that are defined by the information that can be obtained by these methods:

- Film Properties (such as film thickness, growth rate, density)
- Surface Properties (Roughness, Morphology)
- Chemical Composition
- Physical structure
- Mechanical Properties

3.4.2.1 Film Properties (Growth Rate, Thickness, Density)

3.4.2.1.1 Thickness Measurements by Cross Sectional Scanning Electron Microscopy (SEM)

A scanning electron microscope (Zeiss Digital Scanning Microscope Model MSM 950) was used to investigate the deposited films. Cross sections of the films were taken to measure the film thickness and with that the deposition rate. Figure 3.16

shows the images of a UNCD film deposited at a pressure of p = 250 mbar with a MW-power of 1 kW. The gas flow of the process gas was set to 600 sccm with 15 sccm hydrogen (~2.5 %), 4.8 sccm methane (~0.8 %) and 580 sccm argon (~83 %). The substrate temperature during deposition was measured to be 630°C and the deposition time was 5 h.

The film thickness was taken from the cross section pictures and was estimated to be 10 µm giving a deposition rate of 2 µm/h.

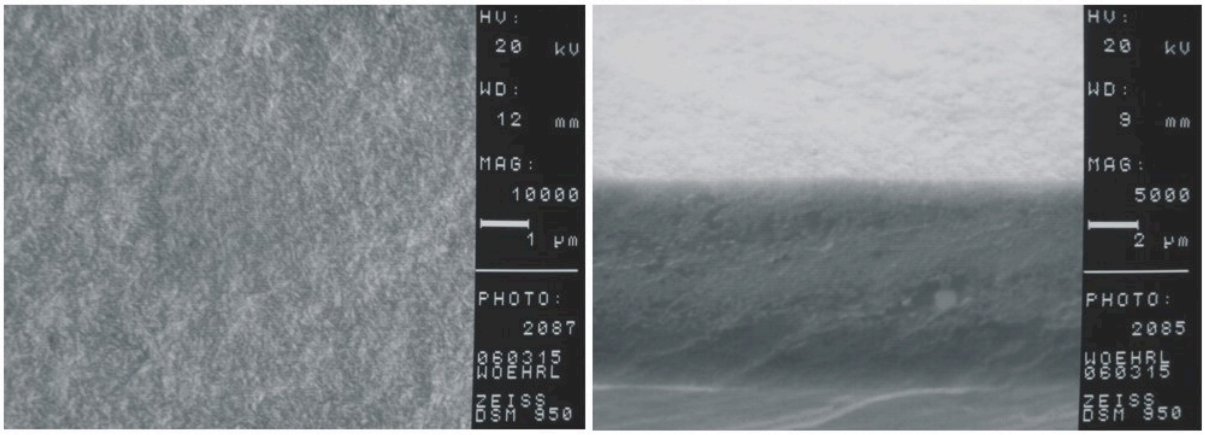

Figure 3.16 Top- and cross-sectional view of an UNCD film taken by scanning electron microscope (SEM)

3.4.2.1.2 Density Measurements

The density of the deposited diamond films where calculated by precision balance measurements of the weight of the films. With known density ρ_{Si} and thickness t_{Si} of the silicon substrate the substrate surface area A_{Sub} can be calculated:

$$A_{Sub} = \frac{g_{\Pr e}}{t_{Si} \cdot \rho_{Si}} \qquad \text{Equation 3.15}$$

By performing pre- and post deposition measurements of the sample weight the mass of the deposited film can be calculated as follows:

$$g_{film} = g_{post} - g_{pre} \qquad \text{Equation 3.16}$$

Finally using Equation 3.15 and Equation 3.16 with the measured film thickness t_{film} one can calculate the density of the deposited films:

$$\rho_{film} = \frac{g_{film}}{A_{Sub} \cdot t_{film}} \qquad \text{Equation 3.17}$$

3.4.2.2 Morphology

3.4.2.2.1 Morphology Measurements by Scanning Electron Microscopy (SEM)

Microscopic methods are particularly useful to investigate surfaces. The film morphology is of importance in thin film technology because it affects the film performance of technical applications (like in optics and tribology). Pictures of the surface of the films were taken to investigate the influence of the process parameters on the morphology by scanning electron microscope (Zeiss Digital Scanning Microscope Model MSM 950). Figure 3.17 shows the measurement of a sample deposited with 5 % hydrogen (left) and a film deposited with 2.5 % hydrogen (right) in the process gas with all other deposition parameters the same. One can see the relative smooth surface of the UNCD films compared to the rougher surface of the film deposited with more hydrogen.

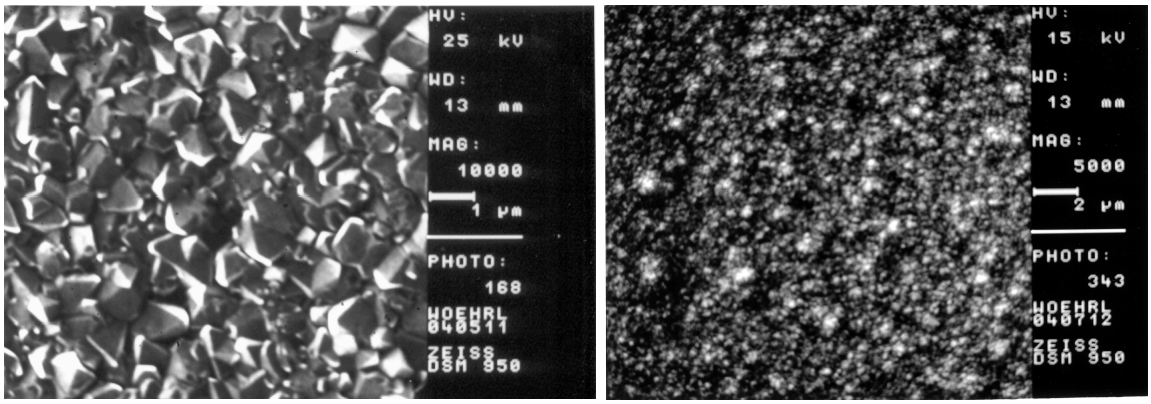

Figure 3.17 Comparison of two diamond films deposited with 5 % (left) and 2.5 % (right) hydrogen admixture

3.4.2.2.2 Morphology Measurements by Atomic Force Measurements (AFM)

The atomic force microscope (AFM) is a scanning probe type microscope that offers a resolution of less than a nanometre that is by a factor of 1000 better than the optical diffraction limit. The AFM consists of a cantilever with a sharp tip with a radius of curvature in the order of nanometres at its end that is used to scan the sample surface. When the tip is brought close to the surface, atomic forces between the tip and the sample lead to a deflection of the cantilever. The deflection of the cantilever is then measured by a laser that is reflected from the cantilever onto an array of photodiodes.

In comparison to the scanning electron microscope (SEM) that is measuring a two-dimensional image of a sample not necessarily corresponding to the morphological features, the AFM provides a true three-dimensional topographical image of the surface giving information about the roughness of the investigated surface. While specimens measured in SEM needs to be conducting and are therefore often coated with a thin metal film (e.g. gold) irreversibly alter the film properties, AFM measurements do not require such special treatments. While the SEM can easily measure an area in the order of square millimetres with a depth of field on the order of millimetres the AFM is usually restricted to a maximum scanning area of around 150 μm^2 with a depth of field in the order of micrometers. Another characteristic that has to be considered for high resolution AFM is the fact that the quality of an image is limited by the radius of curvature of the probe tip and can lead to image artefacts. [Sar91]

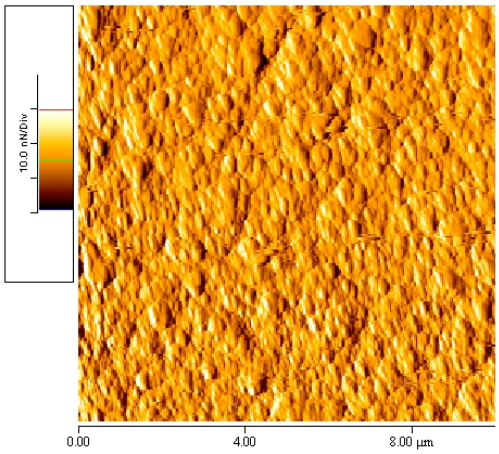

Figure 3.18 AFM measurement of a UNCD film on a SiC substrate

Figure 3.18 shows an AFM measurement of a 10 µm thick UNCD film on a SiC substrate. The measured area on the sample was 100 µm^2. Figure 3.19 shows the roughness measurement along the linear line indicated in the upper left picture. The average roughness of the surface is measured to be R_a= 21.40 nm. This is relatively rough for this kind of films and the reason is to be found in the rough SiC specimen. UNCD deposited on smooth Silicon substrates usually reach a roughness as low as few nm when deposition parameters are chosen right.

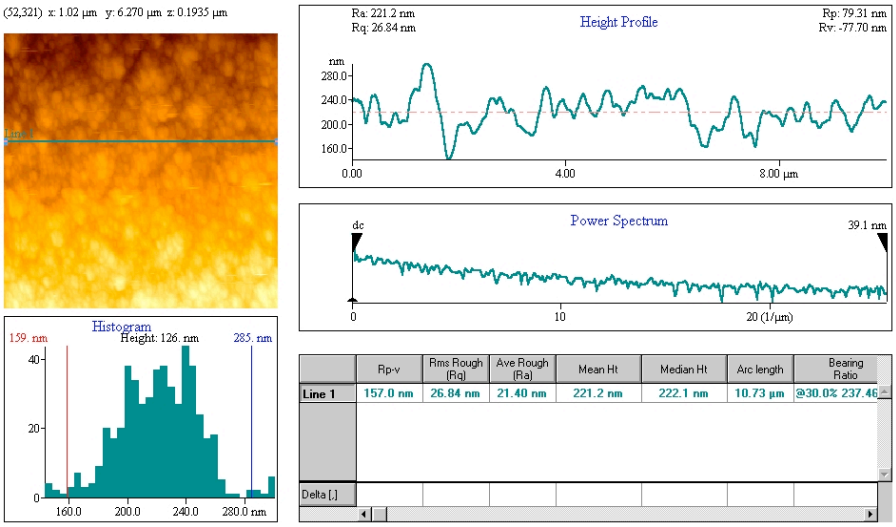

Figure 3.19 AFM roughness measurement of a UNCD film on SiC specimen

3.4.2.2.3 Morphology Measurements by Phase Shift Interferometry

A Phase Shift Interferometer (SENSOFAR PLµ 2300) was used to measure the surface height of the extremely smooth UNCD films on silicon wafers. The sample is scanned vertically in a few steps that are in a fraction of a wavelength. The profiling algorithms produce a phase map of the surface that can be converted to a corresponding height map with a sub-nanometre vertical resolution.

The film surface measured in Figure 3.20 was deposited on silicon with a hydrogen admixture of 6 % at a substrate temperature of 730°C. The average surface roughness over the scanned area was measured to be 1.25 nm. All UNCD films deposited from the standard Ar/H_2/CH_4 gas mixture possess comparable smooth films surfaces proving the low roughness as one outstanding property of the nanocrystalline diamond films in opposition to the microcrystalline diamond films.

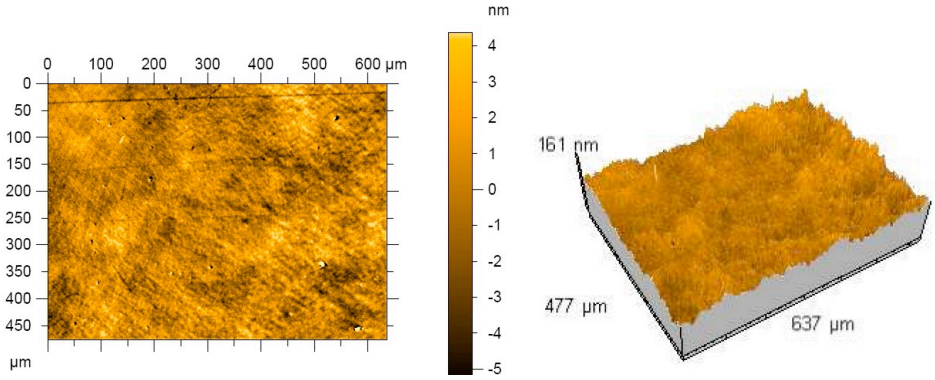

Figure 3.20 Phase Shift Interferometric measurement of UNCD film on silicon

3.4.2.3 Chemical Composition

As mentioned before (Chapter 3.1.4) the internal structure of amorphous carbon films can mainly be characterized by the sp^3/sp^2 ratio and the configuration of the sp^2 phase (rings or chains) on the one hand and by the content of admixtures, usually hydrogen, on the other hand. Furthermore in the case of crystalline films additional information can be obtained by investigating the microstructure such as grain size and crystal orientation. To determine these properties without destruction of the coating – as it is important for most technical applications – spectroscopic methods (FT-IR- and Raman-spectroscopy) are used; because the C-C and C-H-bonds are responsible for the IR- and Raman-spectra, H-content and sp^3/sp^2- ratio can be deduced via deconvolution of these spectra [Ris98] [Hei98] [Rob02]. Both, the Raman and the infrared spectrum, give partial description of the internal vibrational motion of the molecules of the constituent atoms. Both types of spectra alone give no complete description of the pattern of molecular vibration and only the combined results of both methods let us understand the structure and composition of our

carbon films. Essential is therefore a consistent result with all experimental techniques [Buc07].
Some special setups to characterize film properties such as residual stress and adhesion are also introduced in this chapter.

3.4.2.3.1 Raman Spectroscopy

Raman spectroscopy is a powerful non-destructive characterization technique for any carbon system not only amorphous and crystalline carbon films but also for nanotubes, fullerenes and aromatic molecules. Raman spectroscopy is based upon the Raman efect that can be described as scattering of light from a gas, liquid or solid with a shift in wavelength from that of the monochromatic incident radiation; that means for solids inelastic scattering on optical phonons. The internal vibrational patterns are the fingerprint of the material and give information about the structure and composition of the carbon films.

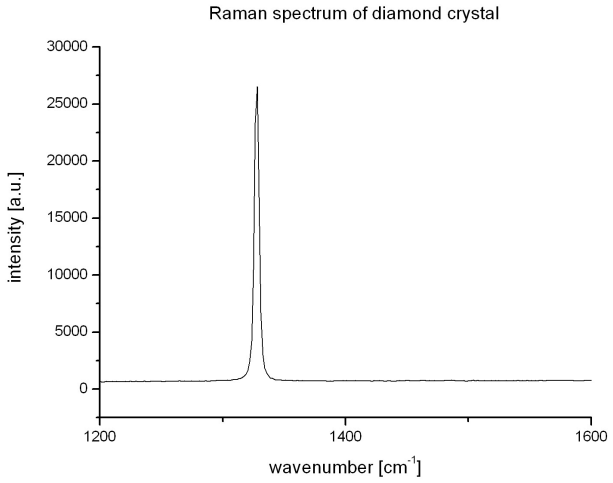

Figure 3.21 Raman spectrum of single crystal diamond

In visible Raman spectra, diamond has a single Raman active mode at 1332 cm^{-1} as shown in Figure 3.21. A similar spectrum is obtained for single crystal graphite with a single peak at 1580 cm^{-1} labelled ‘G’ for ‘graphite’. As disorder increases a second peak appears at around 1350 cm^{-1} labelled ‘D’ for ‘disordered’ as shown in Figure 3.23 for a typical DLC film. One remarkable and important fact is that most disordered carbon films are dominated by these two modes even when the films have no particular graphitic order.

In visible Raman spectra the cross-section of the sp^2 phase is much higher than that of the sp^3 phase [Wad80]. Thus, effects from the sp2-bonded carbon dominate all spectra. Even spectra of carbon films that primarily consist of sp^3-bonded carbon such as ta-C or UNCD films show no direct evidence for the sp^3 configuration but are dominated by the sp^2 features. Therefore it is only possible to derive sp^3 content from visible Raman spectra if there is a direct relationship between the sp^2 and sp^3 phase. An exception would bring the use of UV Raman spectroscopy. In the spectra obtained with UV excitation a new peak is found at around 1060 cm^{-1} conventionally labelled T-peak. The position of this peak and the I(T)/I(G) ratio give direct information about the sp^3 content in the film.

Robertson and coworkers did great effort in finding out how structural information of DLC films can be worked out of the G-Peak and the D-Peak of visible Raman spectra [Rob02]. The difficulty of this task is illustrated by Figure 3.22 which shows the various factors which can shift the G and D peaks in either direction, alter their relative intensities and affect their FWHM.

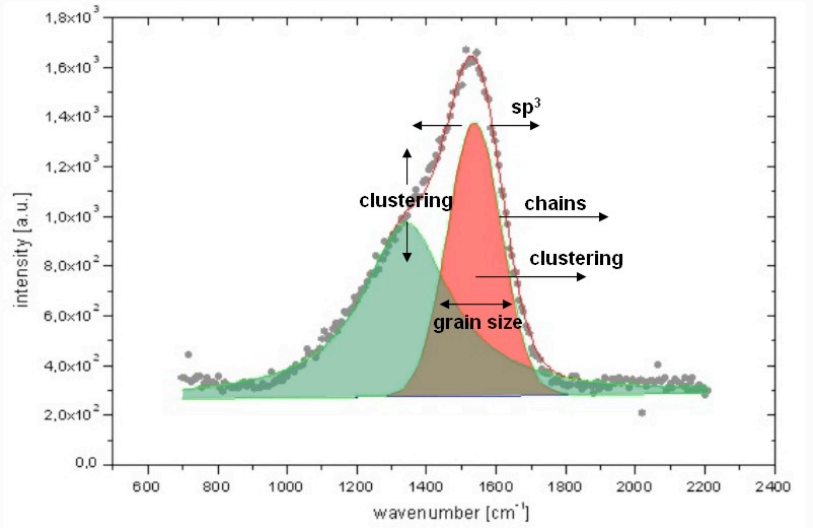

Figure 3.22 Factors affecting Raman spectra in carbon films

They found out that the G mode is actually the stretching vibration of any sp^2 sites, whether in C=C chains or in aromatic rings [Fer00a]. Thus the G-Peak does not only indicate ‘graphite’ in the specimen. Contrary to that the D-Peak is the breathing mode of sp^2 carbon aligned in rings and not in chains.

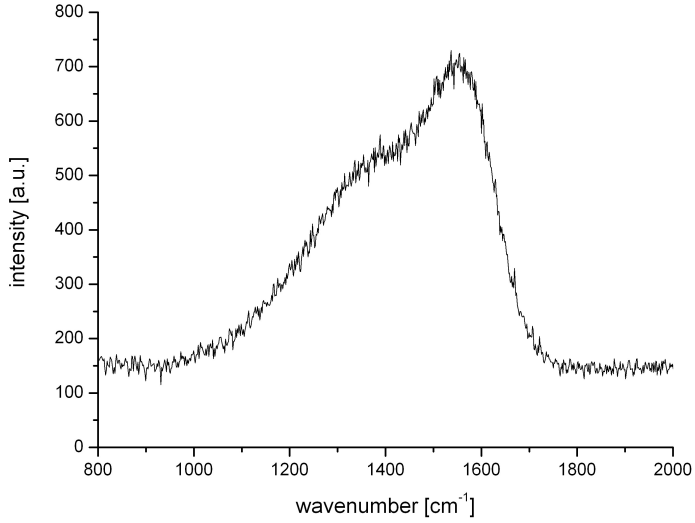

Figure 3.23 Spectrum of DLC film

All Raman spectra of amorphous carbon films can be interpreted by the three-stage model of increased disorder [Fer00a] [Fer00b]. When moving from ordered graphite to nanocrystalline graphite, to amorphous carbon and finally to sp^3-bonded ta-C, the sp^2 groups become first smaller, then topologically disordered and finally change from ring to chain configuration. Characteristic changes can be observed in the Raman spectrum along this amorphization trajectory, namely the position of the G-Peak and the intensity ratio of the D and the G-Peak.

Another hint for increased disorder in amorphous carbon films that can be deduced from the Raman spectra is the full width of half maximum of the G-Peak ($FWHM_G$) that correlates with the disorder. The smaller the sp^2 grain size in the film the $FWHM_G$ increases and with that the disorder in the films.

Another way to measure the disorder of DLC films is the G-Peak dispersion (Figure 3.24). The G-peak position increases as the excitation wavelength decreases from infrared to UV. This dispersion is due to the resonant selection of sp^2 chains of different sizes at different excitation energies [Fer01] [Pis05] and is higher for more disordered films. The G-Peak does not disperse in graphite itself, in nanocrystalline graphite or in glassy carbon. With respect to the G-peak dispersion films can roughly be classified in two types. Films with only sp^2 rings will show a saturation of the G-Peak dispersion around 1600 cm^{-1}, the G position of nc-graphite. In the other class of films, films that also contain sp^2 chains, in particular ta-C and ta-C:H films, the G peak will rise above the 1600 cm^{-1} and can even reach values around 1690 cm^{-1}.

This makes the multi-wavelength Raman spectroscopy a powerful instrument not only to get information about the disorder and configuration of sp^2 sites in the carbon films but also enables one to classify the films.

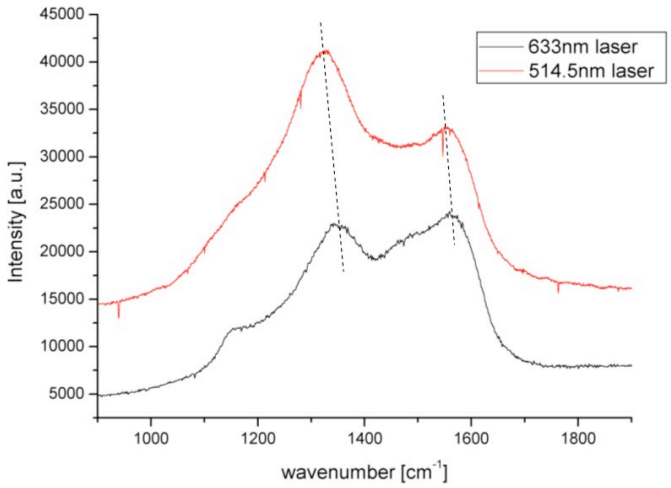

Figure 3.24 Dispersion of D- and G-Peak in UNCD diamond films

By visible Raman spectroscopy no C-H modes can be detected in amorphous carbon films due to the high photon energy necessary. However a typical feature of hydrogenated carbon films is the strong photoluminescence background in the spectra. The ratio between the slope, m, of the linear fitted background and the intensity of the G-Peak can empirically be used as a measure of the bonded H in the films [Mar97].

For completeness it should be mentioned that nitrogen containing amorphous carbon films also show special features in the Raman spectra and that this influence of nitrogen in the carbon films was also investigated [Fer04]. These effects will not be discussed here in detail.

Although it is not possible by visible Raman spectroscopy to measure the dominant sp^3-bonded carbon directly, in the UNCD films Raman spectroscopy is an important method for characterization especially in the case of nanostructured films. This is because the nanostructuring leads to an increased surface to volume ratio of the grains in the film and the grain boundaries (i.e. the film matrix) having more influence on the film properties. Since amorphous bonded carbon can be found in the grain boundaries the film matrix can be characterized by Raman spectroscopy. One major

task when investigating carbon films with Raman spectroscopy is therefore to correlate information from the spectra with film properties such as residual stress, hardness and density. That can trace the changes in the film properties back to changes in the structural configuration in the films. This not only gives a deeper understanding of the mechanisms behind the film performances and lead the way to improve them but also enables to use Raman spectroscopy for non-destructive investigation of those mechanical properties. One possible application for such an investigation is shown later by correlating features in the Raman spectrum with the intrinsic stress in UNCD films.

To analyse the deposited films in this work quantitatively they were characterized by two wavelengths scanning micro Raman spectroscopy. The Raman spectra were obtained by a Jobin Yvon LabRam Raman Spectrometer in the range of 900-1800 cm^{-1} with a step size of 1 cm^{-1}. Two laser wavelengths were used with an Ar Laser (λ=514.5 nm) and a HeNe Laser (λ=632.8 nm).
Figure 3.25 shows a spectrum of an UNCD film. The spectrum was deconvoluted into five peaks that are known to be found in nanocrystalline diamond films [Zai01].

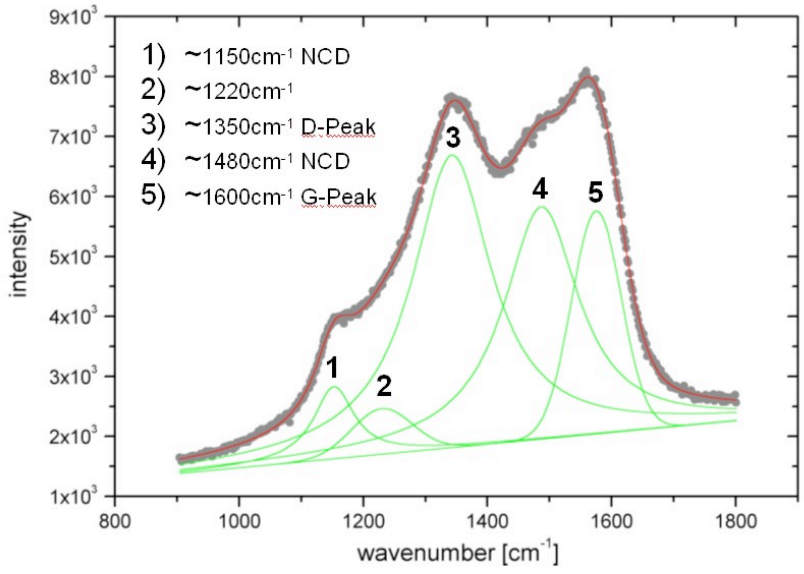

Figure 3.25 Deconvoluted Raman spectrum of NCD film

The fitting constraints for the given peaks were taken from the literature and are listed in Table 3.1.

No.	Peak position [cm^{-1}]	FWHM [cm^{-1}]	Shape
1	1120 – 1150	30 – 150	Lorentzian
2	1180 – 1220	0 – 150	Gaussian
3	1310 – 1450	80 – 400	Lorentzian
4	1475 – 1570	80 – 220	Lorentzian
5	1520 – 1610	40 – 200	Gaussian

Table 3.1 Fitting constraints for the five Raman peaks used taken from [Zai01]

The main features found in the spectra of UNCD are the already described D- and G-peak due to sp^2-bonded carbon in the film. The UNCD labelled peaks at 1150 cm^{-1} and 1480 cm^{-1} respectively are assigned to NCD and UNCD although their true origin is still discussed. Some authors found evidence that these peaks are due to trans-polyacetylene in the grain boundaries [Cas04] [Fer04] [Bir05]. Polyacetylene is an organic polymer with the repeat unit $(C_2H_2)_n$. The polymer consists of a chain of carbon atoms with alternating single and double bonds between them, each bonded with one hydrogen atom. The structure of trans-polyacetylene is shown in Figure 3.26.

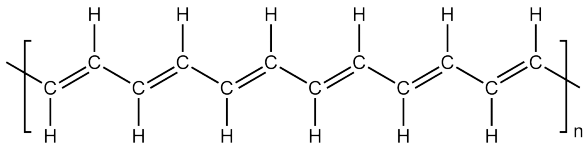

Figure 3.26 Segment of trans-polyacetylene

3.4.2.3.2 Infrared Spectroscopy (FTIR)

The properties of a-C:H films are mainly determined by the sp^3/sp^2 ratio of bonded carbon and the total content of incorporated hydrogen in the film. In comparison to the Raman Spectroscopy that is probing only the C-C bonds in the films the IR-Spectroscopy is sensitive for the C-H bonds. An IR-spectrum of carbon consists of the C-H stretching modes around 2800 cm^{-1} to 3300 cm^{-1} and the C-H bending modes below 2000 cm^{-1}; the C=C double bonds can be seen too, but the peaks depend on the (unknown) surrounding and thus no quantitative conclusion can be drawn from these spectra. Since the C-H vibration modes are well tabulated the

wavenumbers of the peaks in the spectrum can be assigned to specific molecule vibration frequencies. Tables with the vibrational frequencies can be found in [Dis87] and [Ris98]. Using the available data the C-H stretching modes can be divided into three regions: The $sp^1{\equiv}CH$ modes at 3300 cm^{-1}, the $sp^2{=}CH_n$ modes from 2975 to 3085 cm^{-1} and the $sp^3\text{-}CH_n$ modes from 2850 to 2955 cm^{-1}.
Quantitative analysis of C-H vibrations in terms of their absorption strength is challenging. This is mainly because usually a number of overlapping modes contribute to stretching and bending absorption bands that are not readily disentangled (Figure 3.27).

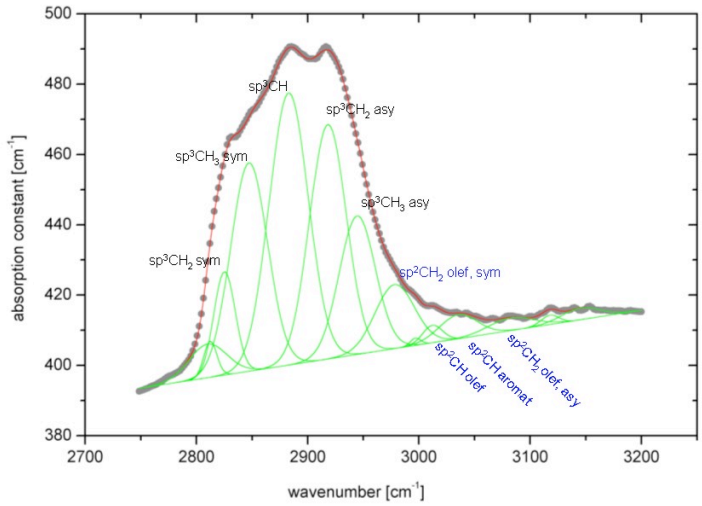

Figure 3.27 FTIR spectrum of UNCD film (stretching modes)

The vibration notations include both the carbon hybridization and the binding configuration of the molecule. Carbon atoms in chain molecules are commonly denoted as aliphatic. If there are one or more double bonds in the chain, the molecule and the resulting vibration is defined as olefinic (short: olef). Ring structures are labelled aromatic (aromat.). Additionally symmetric (sym) and antisymmetric (asy) vibrations of the same C:H configuration are indicated as well.

IR-Spectroscopy is a popular method to determine the hydrogen content in amorphous carbon films [Bey82]. To quantitatively evaluate the data the spectra need to be deconvoluted in the different vibration modes and the area of the deconvoluted peaks taken into account. By multiplying with the absorption coefficients *A* one can calculate the number of hydrogen atoms per area [Rob02]:

$$N = A\int \frac{\alpha(k)}{k} dk \qquad \text{Equation 3.18}$$

However this is not easy because the absorption coefficient depends on the type of C-H bonds. The absorption coefficient in hydrocarbon molecules can differ one order of magnitude because the C-H bonds in aromatic rings have a cross section which is four times bigger than the one of sp^3-C:H bonds [Ris98]. Hence every deconvoluted peak of the IR-spectrum has to be multiplied by the appropriate absorption coefficient A_i. In [Ris98] the hydrogen content was determined by this method by comparing the results to data that were subsequently determined by mass selected thermal effusion showing the adequacy of this routine.
As mentioned above the FTIR spectroscopy is only sensitive to the bonded hydrogen in the film. Therefore when quantitatively analyzing the films the question arises how high the content of unbound hydrogen in the films is. Donnet et al. were able to show by using NMR that the amount of unbound hydrogen can usually be neglected [Don99] in amorphous carbon films.

Analogous to the determination of the hydrogen content in the film one can calculate the sp^3/sp^2 ratio from the deconvoluted spectra. But it should be pointed out that again this result gives only the sp^3/sp^2 ratio of the hydrogen-bonded carbon in the films and not the overall sp^3/sp^2 ratio. Here the sum of the area of sp^3 and sp^2 vibration modes are summed up and compared. The discrete vibrational modes are normalized by being multiplied with their associated scattering cross-sections, which can be found in [Ris98].

The measurements shown in this work were performed with a Bruker FTIR spectrometer EQUINOX® IFS55 that allows to measure spectra between 370 cm^{-1} and 7500 cm^{-1} [Bru95].

3.4.2.4 Physical Structure

3.4.2.4.1 X-Ray Diffraction (XRD)

X-Ray diffraction (XRD) is used to characterize the crystalline structure of the films. The method is based on the evaluation of diffraction patterns obtained by X-ray

radiation interfering with the crystal lattice. The position of the reflection peaks in the diffraction pattern gives information about crystallographic structure and preferred orientation (texture) of the crystals in the film.
The analysis of nanostructured films is problematic because the peaks in the diffraction pattern broaden not only with the reduced grain size in these films but additionally by intrinsic stress (having influence on the position and the FWHM of these films). If the background obscures reflections of higher order, these two contributions cannot be separated. Despite these limitations XRD is a powerful and frequently used method for diamond film analysis [Bac92] [Deu98]. Recently the applicability of the XRD method for UNCD was also shown [Ger05].

The diffraction patterns measured in this work are obtained by a Phillips Diffractometer PW 1710 with a theta 2-theta goniometer using Co K_α radiation.
Figure 3.28 shows a x-ray diffraction pattern of a UNCD film with the assigned diamond crystal orientation.

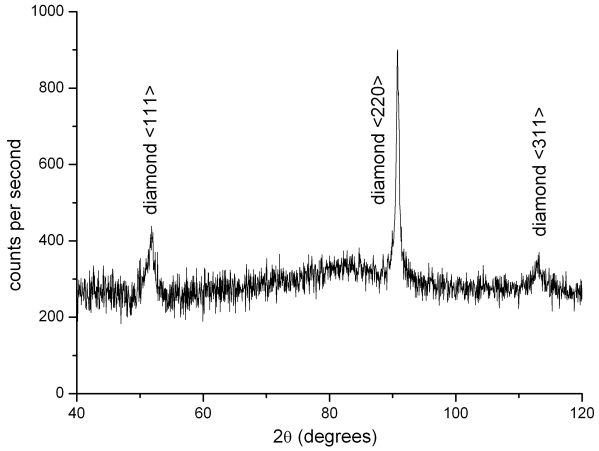

Figure 3.28 XRD pattern of UNCD film

3.4.2.5 Mechanical Properties

3.4.2.5.1 Residual Stress and Coefficient of Thermal Expansion Measurement by SSIOD Method

Stress measurements were performed with a SSIOD ("**S**urface **S**tress **I**nduced **O**ptical **D**eflection") setup. By measuring the deflecting angle of a laser on a

substrate the curvature of a substrate can be measured. With respect to Stoney's equation (Equation 4.1) one can calculate the residual stress in the film σ with respect to substrate properties (Elastic modulus E_{sub} of the substrate, Poisson ratio ν of the substrate, substrate thickness t_{sub} and to the film thickness t_{film}). Because the residual stress is calculated from the change in substrate curvature induced by the deposited film a pre-deposition R_{pre} and a post-deposition measurement R_{post} of the substrate curvature is necessary [Sto09].
Because one setup to measure the residual stress was designed in the run-up to this work and extended in the course of this work to measure additional film properties such as the Coefficient of Thermal Expansion a special chapter is dedicated to this topic in Chapter 5.4.3.

3.4.2.5.2 Hardness and E-modulus Measurements by Nanoindentation

The hardness of a material – although no physical quantity – is an important material property with great technological importance. Hardness is a technical parameter that is defined as the resistance of a solid material to the indentation by another material.
Traditional indentation refers to a variety of hardness tests applied to small volumes that differ mainly in the indenter geometry.
The Brinell hardness test applies a hardened steel or carbide ball as indenter. This method is especially useful to measure the bulk or macro-hardness of a material.
Another common method to determine the hardness by indentation is the Vickers hardness test. Here the indenter is in the form of a right pyramid with a spare base and an angle of 136 degrees between opposite faces and is made of diamond. The Vickers Test can also be used to test very hard materials and has the widest scales among hardness tests. The unit of the Brinell as well as the Vickers hardness test is N/m^2.
In all indentation hardness tests the load placed on the indenter tip is increased as the tip penetrates further into the specimen reaching a user defined value.
After reaching the maximum load the tip is removed again. The area of the residual indentation in the sample is measured and the hardness can be calculated. The hardness H is defined as the maximum load P_{max} divided by the residual indentation area A_r after removal of the indenter.

$$H = \frac{P_{\max}}{A_r}$$ Equation 3.19

As can be seen from this equation, the harder the investigated material the smaller the measured indent will be.

For most applications the residual indentation area A_r can be measured directly using an optical light microscope giving the hardness of the material.

In Nanoindentation small loads and tip sizes are used and the measured indentation area becomes very small. Instead measuring the indentation area by atomic force microscopy or scanning electron microscopy techniques (which can be quite cumbersome) the materials response to the penetration of a defined indenter shape (e.g. Vickers, Berkovich or Knoop) into a sample is recorded. During the indentation a record of the depth of penetration is made and the area of the indent can than be calculated using the known geometry of the indentation tip. A load-displacement curve (Figure 3.29) can be plotted and these curves can be used to extract mechanical properties of the material [Oli04]. Especially from the hysteresis between loading and unloading the plastic (permanent) deformation under the indenter and thus elastic properties of the film can be determined additionally.

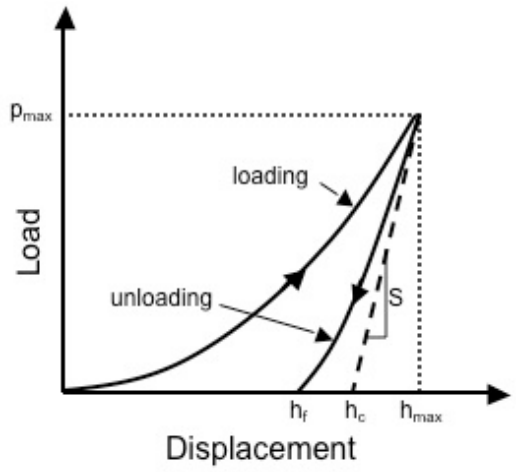

Figure 3.29 Load-displacement curve of an indentation measurement

In Figure 3.29 it is shown how a load-displacement can be interpreted with h_{max} being the maximum depth of the indenter during indentation and h_f the depth of the impression after removing the indenter. The plastic displacement h_c is found as the

crossing of the x-axis of a line originating from the top of the unloading curve with the slope of the tangent of the unloading curve *S*.

Figure 3.30 shows a cross sectional views of an indentation during load and after unload.

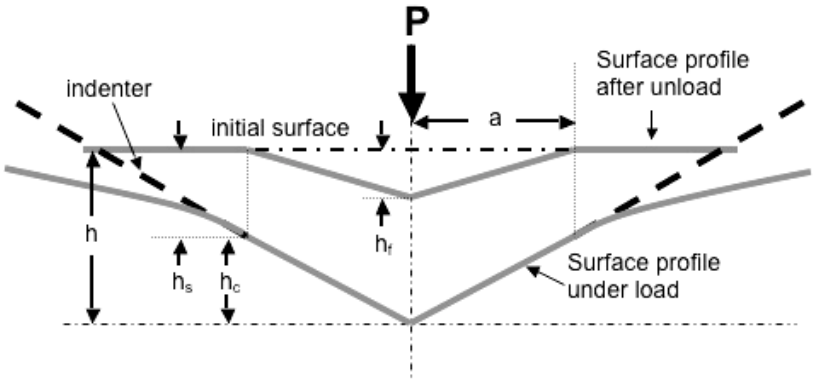

Figure 3.30 Schematic representation of the impression during load and impression left after unload

The technical parameter hardness although easy to measure, turned out to be of a very complex character. It implies effects resulting from surface roughness, grain boundaries, interfaces, and elastic and plastic deformation contributions. A consistent theory of hardness indentation measurements is, hence, still absent although approaches where taken to isolate aspects of correlations between hardness values and elemental physical properties on the one hand, as well as to correlations between hardness values and application properties on the other hand [Pet83] [Mat87b]. Rother tried to find an approach to interpret hardness indentation measurements based on these recorded indentation load-indentation depth measurements by energy-related data interpretation [Rot94].

The Nanoindentation technique is used in this work to gain the hardness and the elastic Modulus of the deposited films. For the measurements a Berkovich tip which has a three-sided pyramid geometry is employed.

As indicated in Figure 3.29 the slope of the load-indentation depth curve upon unloading is used to determine the stiffness *S* of the tested material given by $S=dP/dh$. The stiffness of the contact is then used to calculate the reduced modulus of elasticity as

$$E = \frac{\sqrt{\pi}}{2\sqrt{A(h_c)}} S \qquad \text{Equation 3.20}$$

where $A(h_c)$ equals the contact area of the Berkovich tip with respect to the residual indentation depth. For the Berkovich tip geometry $A(h_c)$ is calculated by

$$A_c = 24.5 \cdot h_c^2 \qquad \text{Equation 3.21}$$

with

$$h_c = h_{\max} - 0.75 \frac{P_{\max}}{S}. \qquad \text{Equation 3.22}$$

The reduced modulus of elasticity E_r includes contributions from both the material being tested as well as the response of the test device itself.
E_r is related to the modulus of Elasticity E_s of the test specimen through the following relations from contact mechanics

$$\frac{1}{E_r} = \frac{(1-\nu_i^2)}{E_i} + \frac{(1-\nu_s^2)}{E_s} \qquad \text{Equation 3.23}$$

with E_i and ν_i being the property of the indenter material. For a diamond indenter tip E_i is 1140 GPa and ν_i is 0.07.

.

4 Experimental Setup

In this chapter the main components for the deposition of the nanocrystalline diamond films will be discussed. In detail this is the CYRANNUS® plasma source and the setup of the vacuum chamber. Due to the importance of substrate temperature for the deposition of diamond films a more in-depth chapter is dedicated to the aerosol substrate holder cooling that was developed for the deposition chamber during this work within a Diploma-Thesis of Degenhardt [Deg05] supervised by the author.

In addition the setup for measuring the residual stress in the deposited films will be discussed in this chapter due to its relevance for the experimental analysis of a variety of mechanical properties later in Chapter 4.4.

Finally the deposition process including the substrate pre-treatment will be introduced in this section.

4.1 CYRANNUS

The nanocrystalline diamond films shown in this work were deposited with a 2.45 GHz IPLAS *CYRANNUS*® I-6" plasma source. The functional principle of this microwave plasma source was explained in detail in Chapter 3.3.3.1.

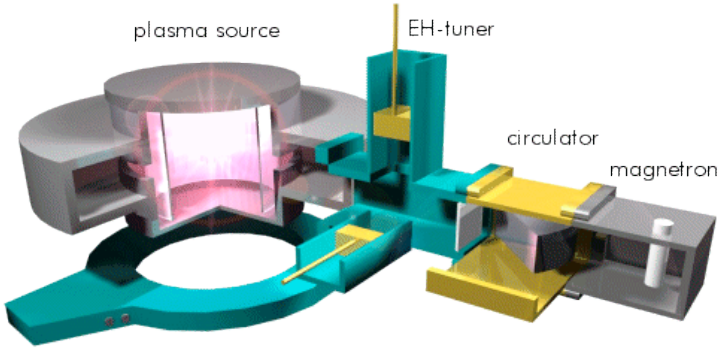

Figure 4.1 schematic picture of CYRANNUS® Plasma source

The plasma source consists of a plasma chamber that is designed as a cylindrical resonator that includes a quartz recipient (Figure 4.1). The plasma chamber is supplied with microwave power by a multi antenna arrangement of a surrounding ring resonator. The microwave supply is realized by a microwave generator (magnetron),

a subsequent microwave isolator (microwave-circulator and –dump to prevent reflected microwaves to come back to the generator) and a tuning element (EH-Tuner) consisting of an E- and an H-junction and two adjustable sliders. The tuning element is used to adjust the plasma source to potential operation states that could change by choosing different deposition parameters (e.g. deposition at different pressures) or by changing the chamber geometry (e.g. by modifying the substrate holder). The maximum power input is limited to 5 kW for by the microwave power generator (alter® power systems SM1180).

R26 flanges connect the microwave components. To keep the mechanical load for the R26 flanges as low as possible the whole microwave feeding was supported by a column on which the whole system rests additionally to the plasma source itself that is mounted to the vacuum chamber.

A diode (S-Team Detector 451570 S/No 1589) is connected to the circulator at the front side. The diode is connected via a coaxial cable with a voltmeter (Keithley 177 Microvolt DMM) that displays a signal allowing to get information of the reflected microwave power (with non linear correlation between output signal and reflected power because the characteristic curve of the diode is not linear). The displayed voltage should never exceed 150 mV. A value of 250 mV is critical for the diode itself.

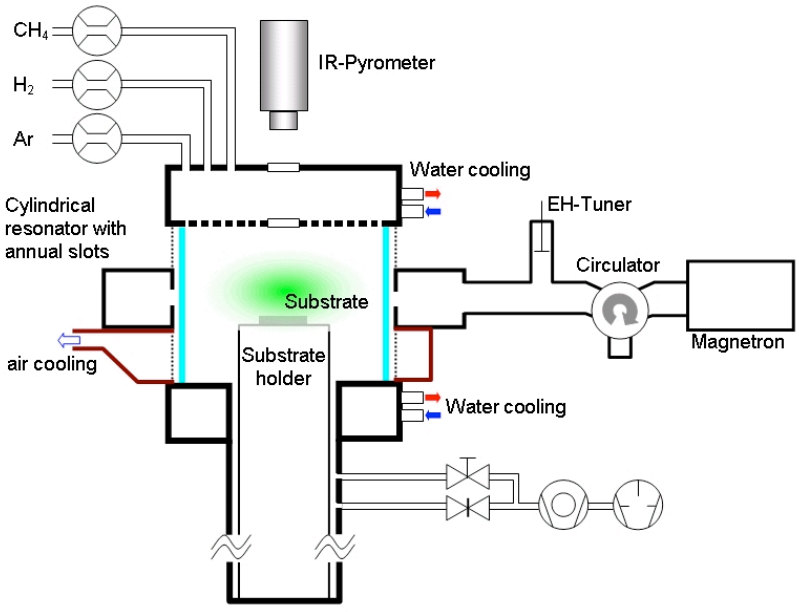

Figure 4.2 Schematic picture of plasma source with microwave supply

An air duct that is cooling the cylindrical quartz resonator surrounds the ring resonator. The fan needs to be connected in a way that it is drawing the air away

from the resonator and not blowing cool air in the direction of the resonator because the cooling is more evenly by this first method. The temperature of the air drawn into the fan must not exceed 55°C because components of the fan can be damaged at higher temperatures.

The MW-generator, the MW-isolator, the upper and the bottom flange of the plasma source are water-cooled. A cooling circuit was installed as shown in Figure 4.3. It is a continuous serial cooling circuit that provides water to all components. The cooling water is entering the system at the “in” labelled inlet of the microwave generator; from there it flows through the MW-isolator back to the MW-generator. Inside the generator a flow controller monitors that a sufficient amount of water is flowing through the system. In the case of a failure in the water supply it automatically turns off the microwave generator. From the “out” labelled outlet of the generator the water flows to the thermal more loaded upper flange of the plasma source and leaving the cooling circuit through the bottom flange of the resonator.

Both at the inlet and after leaving the cooling circuit the water temperature is measured with thermocouples. Both measurements are important. The pre cooling circuit measurement is important to prevent the usage of cooling water that is too cool and would lead to condensation of water inside the microwave generator when air humidity is too high (dew point). Such condensation could lead to damage inside the generator and must be prevented by heating the cooling water to be above the dew point. The temperature measurement of the used cooling water gives information about the heat input into the water by the plasma source and could give evidence for irregularities in the process. This for example could be a bad MW-power coupling into the plasma or a plasma ball that is too close to either the bottom or the top flange of the plasma source.

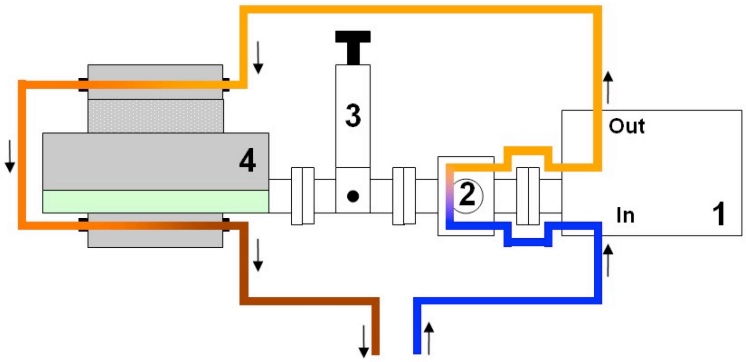

Figure 4.3 Cooling circuit of the microwave components: 1) microwave generator 2) MW-isolator 3) EH-Tuner 4) CYRANNUS plasma chamber

4.2 Vacuum Chamber

The Cyrannus plasma source is installed on top of a 100 l UHV chamber. To realize the connection the bottom flange of the plasma source was changed in a way that it can be connected to the vacuum chamber by a standard CF200 flange. In the same process the opening in the bottom was widened from 100 mm diameter to 110 mm diameter to allow a loading with 4-inch silicon wafers.

The rather large vacuum chamber in combination with the variety of flange connections of different sizes has the advantage of easily adding vacuum components like vacuum gauges or other measurement instruments to the setup. Furthermore the spacious setup allowed more freedom in constructing the substrate cooling which is inserted into the vacuum chamber through the bottom flange.

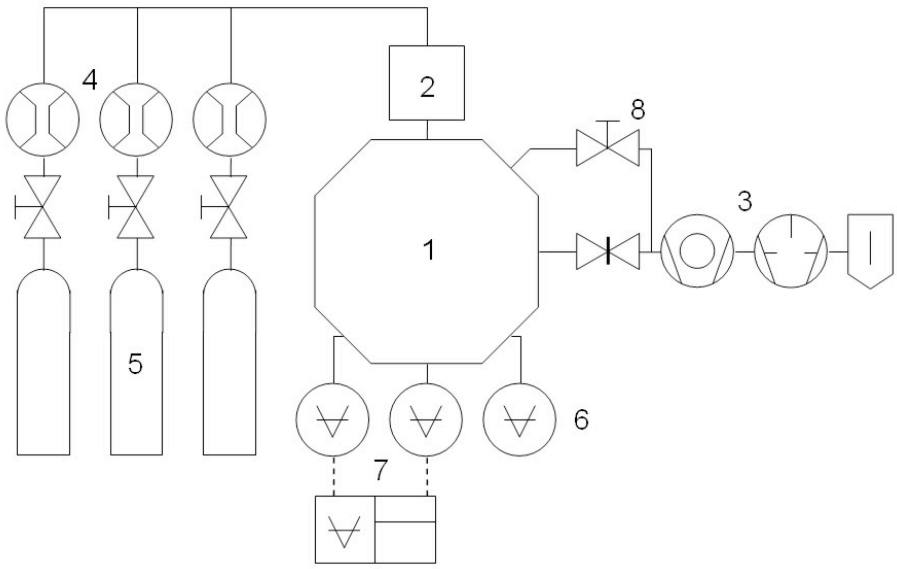

Figure 4.4 schematic drawing of the vaccum side of the setup: 1) 100 l vacuum chamber 2) CYRANNUS® plasma source 3) *Leybold* pumping station: (rotary vane pump Trivac D16B and turbo pump Turbovac 361) 4) Mass-Flow-Controller 100sccm / 5000sccm / 50sccm / 200sccm 5) gas supply argon, hydrogen, methane 6) *Leybold* membrane vacuum gauge 7) *Leybold* Combivac (Pirani vacuum gauge TTR 211B and ionisation vacuum gauge ITR100) 8) MKS Excaust Valve Controler (Type 252A)

Evacuation is realized by a Leybold pumping station that consists of a rotary vane pump (Triviac D16B) and a turbo pump (Turbovac 361).

The process gas inlet into the plasma chamber is realized by a gas shower in the top flange of the CYRANNUS® cylindrical resonator. The gas flow is controlled by MKS gas flow controllers (100 sccm / 5000 sccm / 50 sccm / 200 sccm) and a MKS controller unit (MKS multi gas controller 647C).

As it will be explained later in the chapter about the substrate holder cooling (Chapter 4.3) the substrate temperature is measured from above by an IR-pyrometer through the plasma. To do this, two KBr windows were integrated in the center of the gas shower.

All data measured during the deposition process is acquired and logged by a HP Data acquisition scanner (HP 34970A). A program was coded in LabVIEW that allows displaying and saving the data in a data file. LabVIEW (short for Laboratory Virtual Instrumentation Engineering Workbench) is a platform and development environment for a visual programming language from National Instruments. The program is logging the data of the reflected MW-power, the substrate temperature

and the pressure during the whole length of deposition every 15 s. Unexpected results in the deposited films can thus be traced back to possible irregularities during the deposition process. Additionally the program is communicating by a client/server scheme through the intranet to remotely control the deposition process.

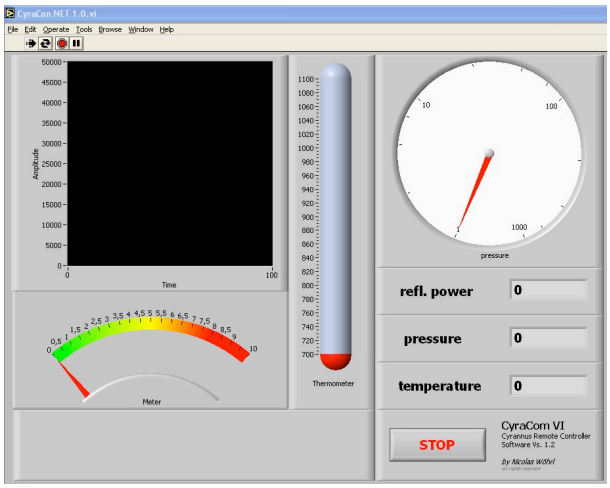

Figure 4.5 screenshot of the custom-made process controlling program

Finally the setup consisting of plasma source, vacuum chamber and the substrate holder was characterized by measuring the reflected power during the deposition process. This was done at two typical set of parameters: As process gas mixture 1 % methane in 99 % argon was used as a typical process gas in UNCD deposition. Two different pressures were chosen with 3 mbar as typical pressure where the plasma is ignited and 200 mbar as typical deposition pressure.

The diagrams Figure 4.6 and Figure 4.7 show the measurements of the reflected power at the two pressures against the setting of the EH-Tuner. The diagrams do not only show the best setting of the EH-Tuner for minimal reflected MW-power but also the regimes where the plasma will ignite best (regime with best MW-power coupling) and the regimes where the plasma broke down and no stationary operation was achieved (white regimes outside the blue).

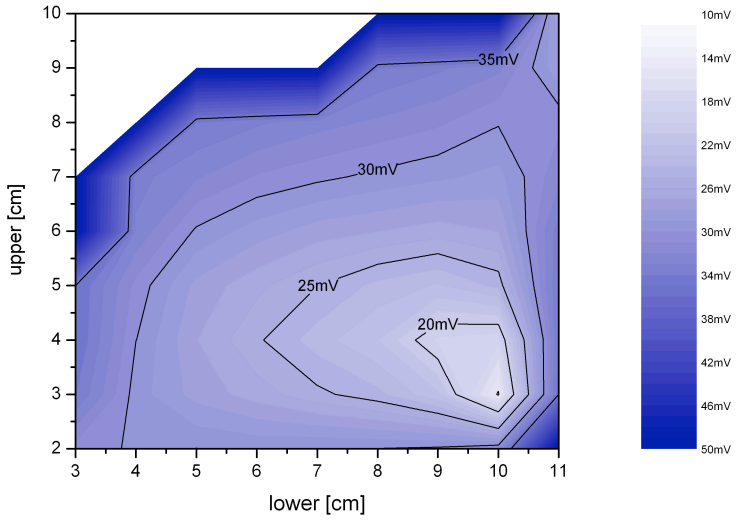

Figure 4.6 Reflected MW-power at typical plasma ignition parameters: 99 % argon 1 % methan / p=3 mbar / P_{MW}=600 W

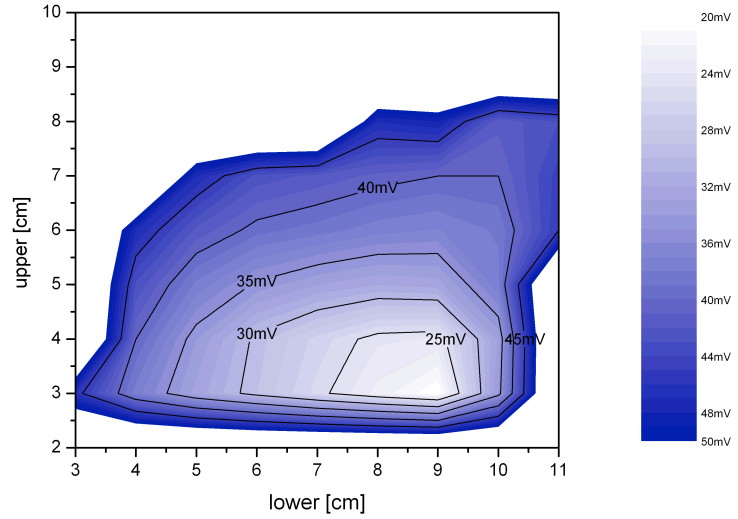

Figure 4.7 Reflected MW-power at typical deposition parameters: 99 % argon 1 % methan / p= 200mbar / P_{MW}=1 kW

The diagrams of the reflected power can be used as a rough guideline for the operation and ignition of the CYRANNUS plasma source in combination with the chosen setup. It should be mentioned here that it is nevertheless necessary to control the reflected power and adjust the EH-Tuner for every single experiment

because even small changes in the process parameters like the process gas mixture, position of the substrate holder in the plasma or choosing a different substrate (with a high dielectric coefficient ε_r) will affect the impedance of the whole system and makes an readjustment of the microwave coupling necessary [Ipl02].

4.3 Substrate Holder with Aerosol Cooling

Results of this chapter were published in [Buc09].

Although the concept of the substrate holder used is explained here in a separated chapter the design and the performance of the cooling is directly linked to the originalities of the plasma source and must be adapted to it. Neither part of the experimental setup can be viewed by its own but should be grasped as an integrated system. As shown later in this chapter a shortfall of one of the systems components can be compensated by one of the other components. For example it is possible to compensate a system inert inhomogenity in the plasma density (and by that an inhomogeneous temperature profile on the substrate) resulting from the plasma source geometry by applying a specific cooling profile by the substrate holder.

As shown in Figure 3.5 the substrate properties are one major factor in thin film deposition. Substrate temperature is thereby a critical parameter in diamond growth, which is significantly affecting the growth rate and the quality of the deposited films. Therefore it is essentially important to control the substrate temperature independently from other process parameters. While electrical heaters are widely commercially available in thin film technology, diamond deposition (especially deposition at high pressures and therefore high growth rates) requires a substrate cooling. This is because typical growth conditions for diamond films demands rather high amounts of hydrogen in the process gas. The recombination of the atomic hydrogen leads to a huge heat input into the substrate and the substrate holder. But also deposition of UNCD at high pressures leads to sufficient heating of the substrate holder that makes a cooling system necessary.
A frequently used method for substrate cooling is the use of fluid water cooling. Since the temperature span of fluid water is limited between ca. 20°C and 100°C the difference to the necessary substrate temperature of around 600°C to 1000°C must

be realized by appropriate thermal resistance and thermal conductivity of the substrate holder. The fact that the thermal absorption of the cooling water is limited to a temperature span of around 80°C is limiting the cooling capacity of this method. Breiter, Dopplep, Weiß and Nutsch (TU Ilmenau) introduced a different approach for substrate cooling: The Aerosol water cooling [Bre00].

Because of the huge specific evaporation heat of water (r_{H2O}=2257 kJ/kg) the evaporation comes along with high-energy dissipation and power dissipation respectively. By using a gas and a liquid simultaneously and bringing them together in an atomizer nozzle the bulk liquid (here water) is converted into a fine spray or mist. This fine mist is sprayed on the backside of the substrate holder where it is immediately vaporized absorbing the evaporation heat. The maximum dissipated power as a function of the amount of water used was calculated and diagrammed in Figure 4.8. It is shown that the aerosol water cooling is ten times more effective compared to the conventional water cooling when the same amount of water is used.

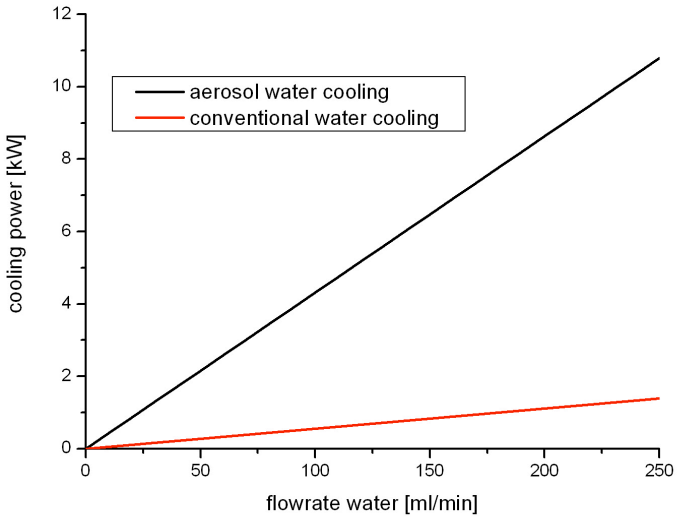

Figure 4.8 Cooling capacity of the aerosol and the traditionally liquid water cooling as a function of the amount of water used [Bre00]

Breitner et al. did not install a feedback loop for the system to control the temperature but only used manual setting of the water flow for a rough stabilization.

The principle was adapted and an active substrate cooling was developed during the time of this work in a Diploma-Thesis by Degenhardt [Deg05].

4.3.1 Temperature Measurement

The substrate temperature is measured by an IR pyrometer. The method is based on the Stefan Boltzmann law that says that the energy radiated by a blackbody radiator per second per unit area is proportional to the fourth power of the absolute temperature.

The pyrometer is a commercially available product (optris® CT). The measurement range is from -40°C to 900°C with an accuracy of ± 1 % or ± 1°C respectively. The temperature is measured in a spectral range from 8 to 14 µm. It is installed on top of the plasma chamber and is measuring the substrate temperature directly through infrared transmitting KBr windows.

The main advantage of this method is the contact free temperature measurement of the substrate and that no device or electrical supplies are interfering with the plasma.

The specifics of substrate temperature measurements through plasmas by an IR-pyrometer were described before [Mey98] and shall not discussed in detail here.

4.3.2 Setup of Controller

4.3.2.1 Atomizer Nozzle

A pneumatic atomizing nozzle with a full cone spray characteristic was used (Figure 4.9) [Lec00]. Due to its functional principle the nozzle does not need a minimum flow rate of water to realize the atomization like it would be in the case of single fluid atomizers. The nozzle achieves an aerosol stream that has a uniform liquid distribution over a circular area with a cone angle of 20°. Dependent on the water and compressed air pressure the aerosol jet passes over to turbulent shape after 30 to 40 cm.

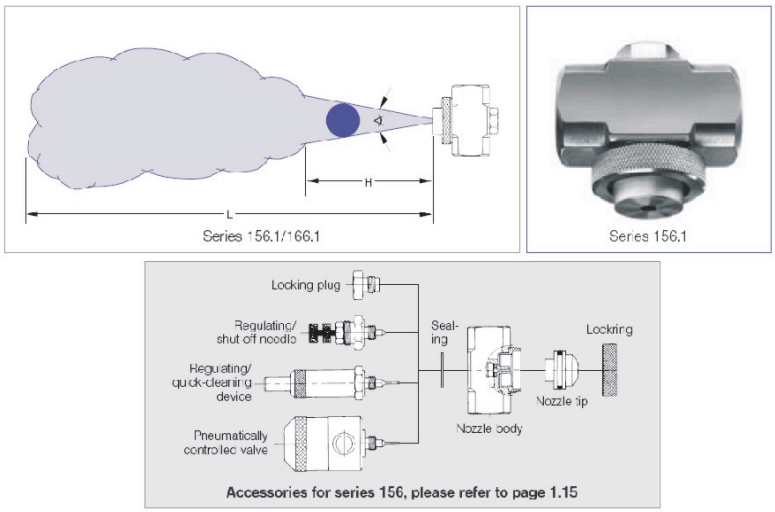

Figure 4.9 Pneumatic atomizing nozzle [Lec00]

The flow rate of the atomized water and by that the cooling capacity can be adjusted in two ways: It can either be adjusted by a needle valve controlling the water supply to the nozzle or of course by the pressures of the water and the compressed air. Fig. 4-10 shows the relation between the needle valve setting and the flow rate. The ratio of water pressure to compressed air pressure was kept constant at 5:6, because the nozzle provides a stable atomization at this ratio. There is a linear correlation between flow rate and needle valve setting for the first 50° after opening of the valve, for bigger angles the characteristic curve flattens as shown in Figure 4.10.

When higher water flow rates compared to the one from the characteristic curves are needed the compressed air pressure can be reduced as shown in Figure 4.11. In this diagram the flow rate of the atomized water was measured in dependence of the water and the compressed air pressure. The diagram clearly shows how a specific flow rate can be realized by variation of either of the two pressures.

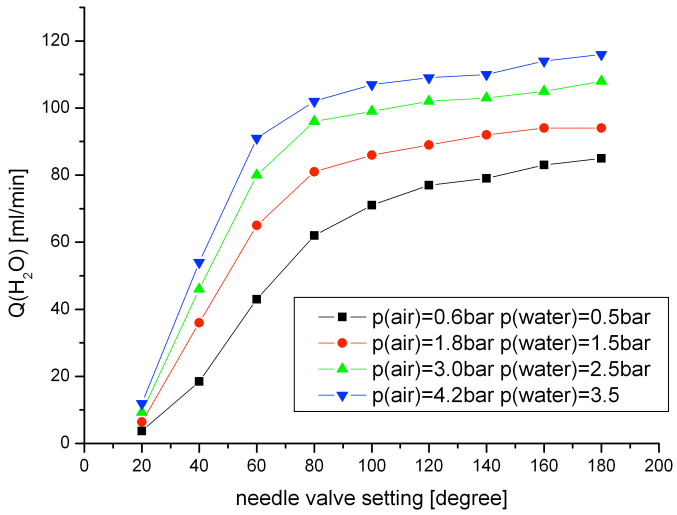

Figure 4.10 Characteristic curve of the atomizer nozzle

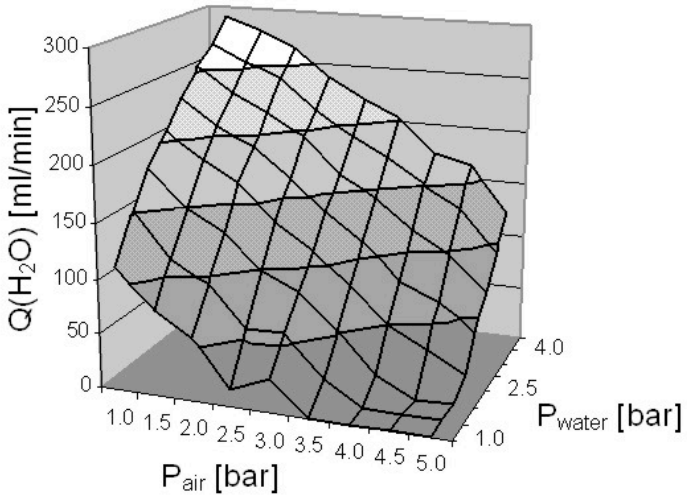

Figure 4.11 Flow rate of the atomized water depending on water and compressed air pressure

4.3.2.2 Digital Controller

The controller was implemented as a PID controller programmed in C++. The sampling rate T_a was set to 0.2 sec because the time constants of temperature controlling tasks are usually around seconds or even minutes. The sampling rate is therefore sufficiently small. The digital controller determines the time delay between

every measurement and uses this value as T_a in the algorithm. Delays in the program flow are accounted for by this method.

4.3.3 Technical Implementation

4.3.3.1 Design of the Aerosol Cooling

The design of the aerosol cooling is schematically shown in Figure 4.12 and as photography in Figure 4.13.

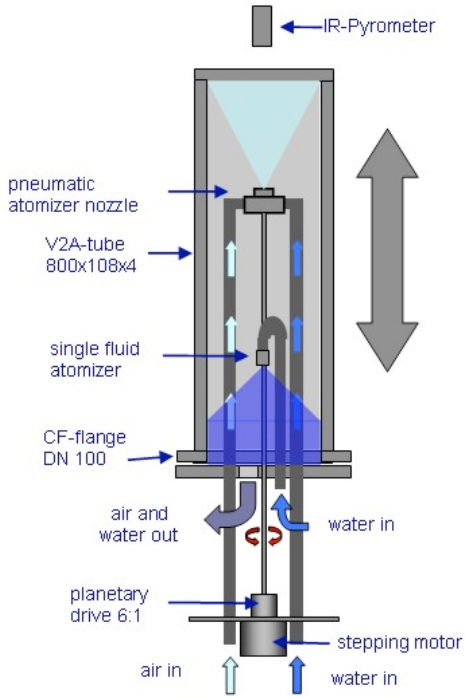

Figure 4.12 Schematic setup of the cooled substrate holder

The main component is the atomizer nozzle described earlier centred in the substrate holder tube. The substrate holder tube is a closed system that can be mounted to any standard vacuum chamber by the CF 100 flange on the bottom. The substrate is placed on top of the substrate holder during deposition. The atomizer nozzle is supplied with water and compressed air via a pressure reducer from the bottom of the system. The flow rate of the atomized water is adjusted by a stepping motor that is connected to the needle valve of the nozzle by an axle. The stepping motor does 400 steps in a full revolution which gives 0.9° for each step. From the set of

characteristic curves shown in Figure 4.10 one can see that the nozzles dynamic lies almost completely in the first 50° of the opening. That accords to 56 steps of the stepping motor, which results in a change of 2 % of the maximum flow rate with every step. Such a coarse regulation limits the quality of the controller from the outset. Therefore the resolution had to be improved. This was done by the use of a planetary drive with a gear reduction of 6:1 resulting in a reduction of step size step by a factor of 6 corresponding to steps with a 0.3 % increment.

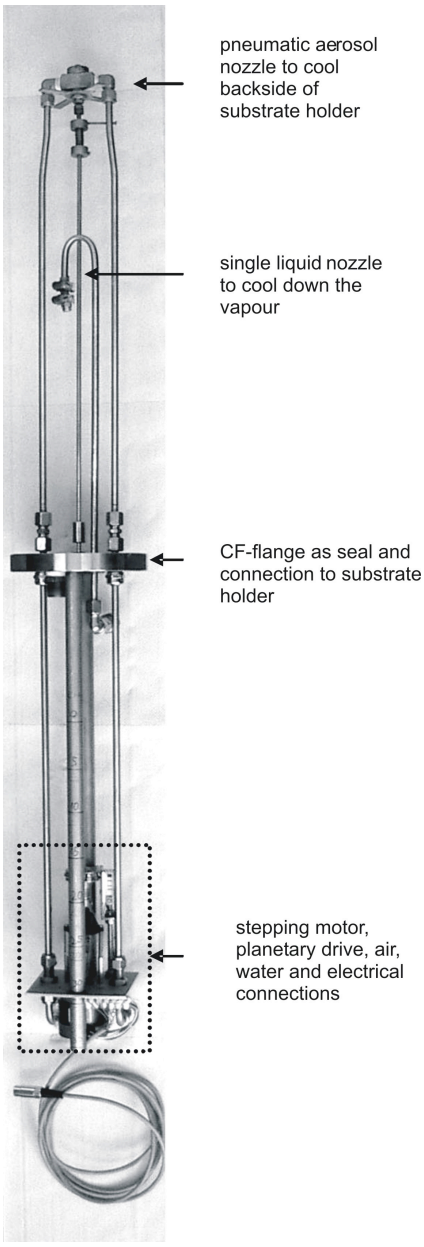

Figure 4.13 Setup of the aerosol cooling

4.3.3.2 Adjustable Distance Nozzle/Substrate Holder

A parameter that has certainly huge impact on the behaviour and performance of the cooling is the distance between the nozzle and the backside of the substrate holder. The cooling was constructed in a way that this distance can be adjusted easily, even during operation.

8 mm stainless steel tubes are used to realize the water and air supply. The tubes are led through the CF-flange DN 100 that is sealing the substrate holder at its bottom. A retaining ring seals the axis, which is also led through the flange. The stepping motor, the planetary drive and a switch for the positional reference measurement of the stepping motor are mounted on a panel along with the supply tubes. By moving this panel up and down the whole cooling setup is vertically adjusted inside the substrate holder. This changes the distance of the nozzle to the substrate holder. The maximum distance adjustable in this setup is 40 cm.

4.3.3.3 Single Liquid Nozzle

A second nozzle, which is located in the lower part of the tube, was installed to cool down and condensate the water vapour which is evaporating on the backside of the substrate holder. By that a heating up of the bottom flange is impeded, that could lead to damaging of the elastomer parts. A single liquid nozzle, which is also vertically adjustable, is used for this cooling step.

During construction attention was paid to the fact that all parts in the substrate holder tube that will come in contact with the hot water vapour, are built from one material – stainless steel – to prevent galvanic corrosion.

4.3.4 Measurements

The substrate cooling was connected to the deposition chamber and its performance was tested during a deposition experiment.

4.3.4.1 Step Function Response

The step function response was tested at a microwave power of 1000 W and a distance between nozzle and substrate holder of 30 cm. The step was initiated at t=0. The characteristic shows a compensation time of ca. 230 sec. (Figure 4.14).

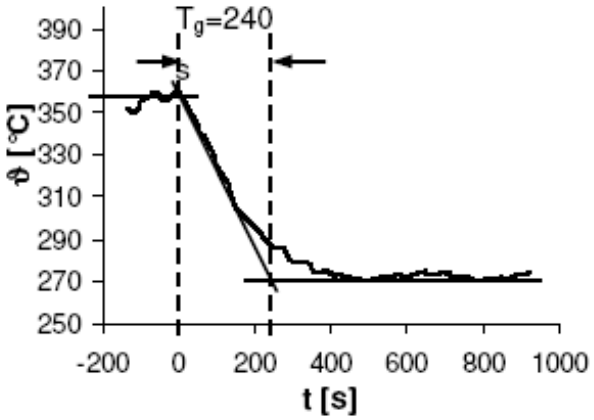

Figure 4.14 Step function response of the controlled system

4.3.4.2 Quality of Control under Deposition Conditions

It was investigated if the quality of control, thus the accuracy of control, depends on the distance between the nozzle and the substrate holder and if there is an optimal distance. For this purpose different distances were adjusted and a controller tuning by the method of Ziegler-Nichols [Zie42] was performed at a temperature of 500°C. Water and compressed air pressure was set in a way that the controller was working in the middle to upper third of the maximum controller output because controller tend to oscillate in low output regimes.

Over a time of 5 min the controlled variable was recorded and the effective value and the maximum deviation of the controlled variable measured. Both quantities give information about the quality of control. The results are shown in Figure 4.15.

The quality of control surpasses the required accuracy (maximum deviation of 5°C) by one order of magnitude for small nozzle to substrate holder distances. Even for larger distances the requirements are surpassed by a factor of two to five.

The water pressure during these test runs was set to a relative low value of 0.2 bar to 0.8 bar to get a controller output signal of at least 20 %. Thus the cooling capacity also has a reserve of at least one order of magnitude.

The results in Figure 4.15 show no preference for one of the controller configurations neither PI- nor PID. Only for higher distances between nozzle and substrate holder the PID-controller seems to be preferable.

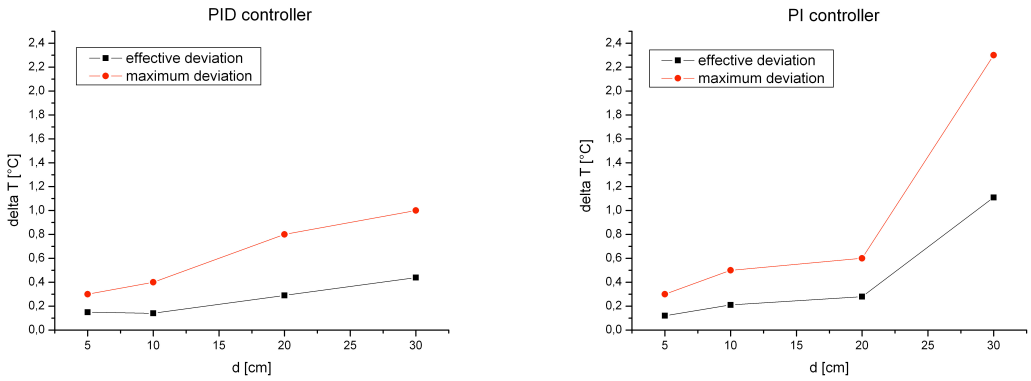

Figure 4.15 Effective value and the maximum deviation of the controlled variable measured during a 5min time interval during deposition conditions

4.3.4.3 Usage of Cooling Profiles

When depositing thin films on large areas not only the time-stability of the temperature is important but also a spatial profile. Obviously a homogeneous temperature distribution over the whole deposition area is a requirement for homogeneity in deposition since the temperature is one critical parameter. In fact two major factors are leading to undesired temperature differences on the substrate holder: Firstly the substrate holder geometry itself is leading to unequal temperature distribution because heat can be dissipated more effectively at the edge of the substrate holder due to better heat conductivity through the substrate holder walls. Secondly the heat input into the substrate holder from the plasma can be non-uniform due to an inhomogeneous field distribution in the plasma usually leading to a higher heat input at the centre. This non-uniformity in the field strength was already proven by simulations performed [Lee06] for the CYRANNUS® plasma source. Both effects are leading to a higher substrate temperature at the centre of the substrate holder compared to the outer edge. Therefore a cooling profile with a higher cooling capacity in the middle of the substrate holder would be desirable to compensate

temperature inhomogenities. Moreover an adjustable cooling profile would be advantageous to be able to adjust the cooling to changed deposition conditions.
Taking a closer look at the spray characteristic of the used atomizer nozzle it is clear that for small distances between the nozzle and the substrate holder the center will be cooled more than the edge.
The right distance between nozzle and substrate holder could possibly optimize the temperature profile of the substrate holder. To investigate this possibility temperature profiles were measured for different distances.
The pyrometer head was first centred over the substrate holder to get a setpoint of 500°C in the middle of the substrate holder. The controller was deactivated to keep all settings constants during the spatial measurement of the temperature.
Figure 4.16 shows the results of the spatial measurements. The 20 cm measurement is taken as the reference measurement and all other results are plotted in comparison to this reference data. A higher value therefore means higher temperature compared to the 20 cm setting. The results confirm the expected cooling profile when the distance of the nozzle to the substrate holder is varied. For short distances (5 cm, 10 cm) the temperature at the edge is higher compared to the 20 cm measurement. In contrast to this the edge of the substrate holder is cooled more effective for a distance of 30 cm. This trend is not continued for the distance of 40 cm where the edge is cooled less effective compared to the reference measurement of 20 cm. One possible explanation could be turbulences in the tube.
The measurements have shown that the nozzle distance to the substrate holder makes it possible to realize cooling capacity profiles on the substrate holder.

Combining these results with the field strength simulations made for the CYRANNUS® plasma source [Lee06] a homogeneous deposition of UNCD films over a large area can be realized. The works on uniform large area deposition are not finished yet and will be incorporated into future works.

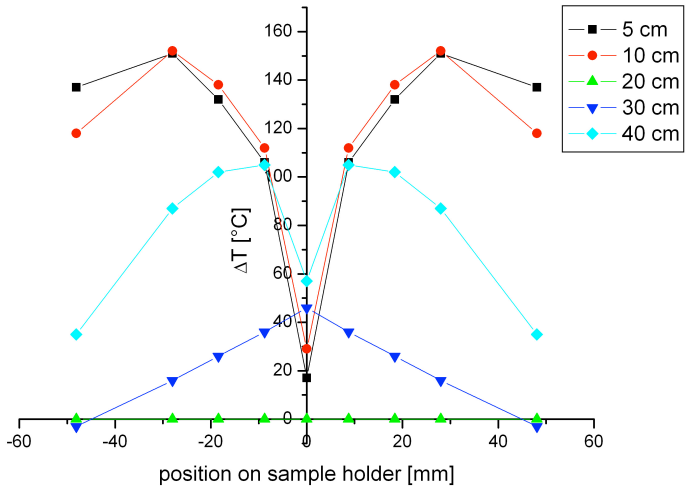

Figure 4.16 Differences between the temperature profiles for different nozzle distances

4.4 SSIOD

4.4.1 Principles of Substrate Curvature Measurement

As mentioned before residual stress in thin films lead to a bending of the substrate. This bending can be measured and the residual stress quantitatively derived from it. Ideally long, narrow samples (length:width ratio 2:1) are used for stress measurements so that the Stoney equation can be used to calculate the residual stress:

$$\sigma = \frac{E_{sub}}{(1-\nu)} \frac{t_{sub}^2}{6 \cdot t_{film}} \left(\frac{1}{R_{post}} - \frac{1}{R_{pre}} \right) \qquad \text{Equation 4.1}$$

It is striking and feasible that primarily only material constants of the substrate are needed to calculate the residual stress with this equation: E_{sub} represents the elastic modulus of the substrate; ν is the Poisson ratio of the substrate and t_{sub} the substrate thickness. Solely the film thickness t_{film} must be measured as information of the film. R_{post} and R_{pre} represent the curvature of the sample measured before and after the

deposition respectively because for the calculation of the residual stress in the film the change in the curvature of the substrate is essential.

For thick films the film bending moment and resultant flexure stress are no longer negligible and the film/substrate structure must be treated as a composite beam as Windischmann and coworkers worked out for diamond films [Win95].

Because the film thickness investigated in this work is relatively large (usually >10 µm) the Brenner-Senderoff equation must be used to avoid substantial errors in the calculated stress [Bre49]

$$S = S_0\left(1 + 4R\frac{t_{film}}{t_{Sub}} - \frac{t_{film}}{t_{Sub}}\right) \qquad \text{Equation 4.2}$$

where R is the ratio of the film and substrate biaxial moduli (6.08 for polycrystalline diamond on (100) silicon) and S_0 is the stress derived from the Stoney equation.

The maximum residual stress and the resolution of the stress measurements strongly depend on the boundary conditions of the measurement. As one can get from the Stoney equation, substrate material, substrate thickness and film thickness need to be considered. Exemplarily the numbers for a 1 µm thick film on a silicon wafer of 425 µm thickness shall be given. In this case the maximum of residual stress measurable with the setup described in Chapter 4.4.2 is 5.5 GPa with a resolution of around 1.4 MPa at a substrate curvature of 4 km.

The determination of the curvature is equivalent to the fitting of a circle, or, because the length of the substrate is usually much smaller than the curvature, a parabola to the contour of the substrate as shown in Figure 4.17.

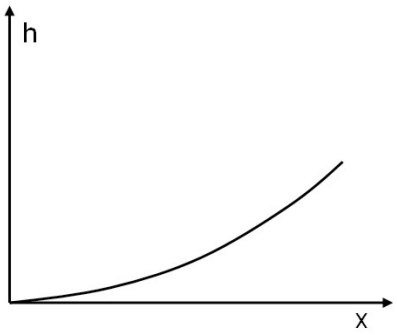

Figure 4.17 Fitting of a circle or a parabola respectively to the contour of the substrate

$$h(x) = \frac{1}{R}x^2 + bx + c \qquad \text{Equation 4.3}$$

It is evident that for the fitting the height must be measured for at least three positions *x*. If it is not necessary to calculate the centre of the circle two tangents or angles at known positions are sufficient according to

$$h'(x) = \frac{2}{R}x + b \qquad \text{Equation 4.4}$$

It should be mentioned here that formerly frequently used setups, which were using one sided clamping at x=0 and measuring h only at the loose end may lead to errors due to thermal drift.

Different methods for the determination of the curvature of a sample are known in the literature [Buc79] [Buc89] [Mos88]. Here, two optical methods are used that allow getting the curvature from electrical signals. Both methods use the fact that a laser beam is deflected in a specific angle depending on the curvature of the sample when scanning over it. The measurement of at least two reflection angles allows calculating the curvature. Figure 4.18a shows this principle schematically for a flat sample. The laser beam strikes the sample perpendicular to the surface and is reflected in the same direction. In contrast to that a curved surface is reflecting the laser beam according to the law of reflection [Figure 4.18b].

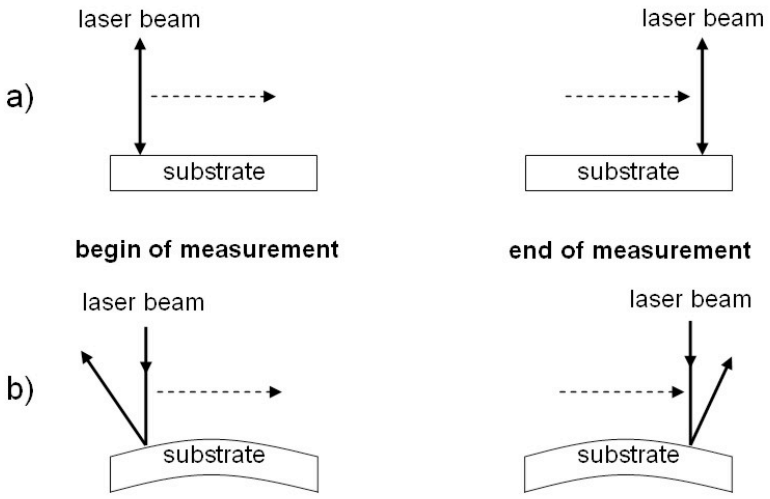

Figure 4.18 Optical principle of SSIOD method

4.4.2 High Stress SSIOD Setup

The setup for one apparatus used [Pan84] is shown schematically in Figure 4.19. The measurement of the angle of reflection is done by a position sensing diode (PSD). The PSD is in principle a one-dimensional expanded “normal” diode. It consists besides of one ground contact in the middle of the diode of two electrical contacts at each end of the diode over which the laser-induced current can drain off. By comparing the two currents and standardization to the overall current one gets the position information of the focused laser beam spot on the diode, independent from the light intensity.

All optical components are set up on a vibration absorbing optical bench. The laser beam (3) is reflected by mirrors (4) onto the substrate (5) and reflected back onto the position sensing diode (6). The optical path length of the laser is a decisive factor for the sensitivity of the setup and was therefore extended by the mirrors (current optical path length of 1 m). The laser and the PSD are mounted on a linear positioning stage (2) that allows scanning over the sample. Although – like shown earlier – the measuring of two reflection angles would be sufficient; the angles at 60 positions are measured to increase the accuracy of the measurement.

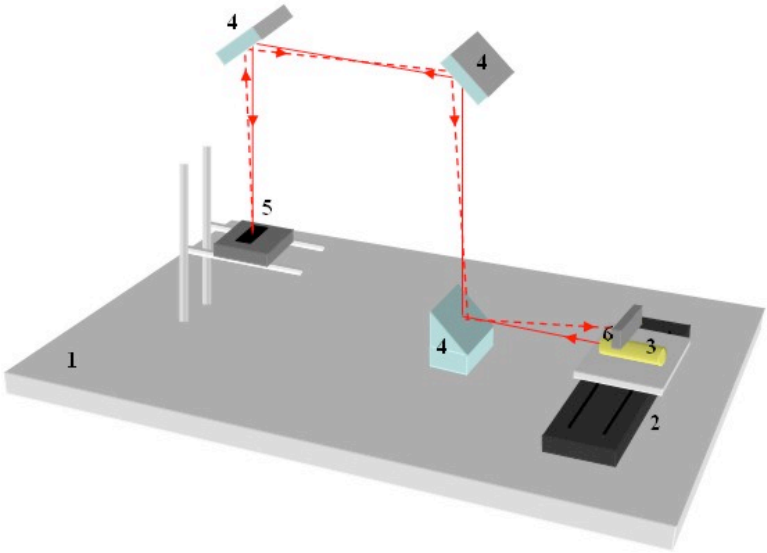

Figure 4.19 Setup to measure strong curved samples: 1) vibration absorbing optical bench 2) linear positioning stage 3) laser 4) mirrors 5) substrate on stage 6) Position sensing diode (PSD)

Figure 4.20 shows the measurement of a curved sample. The diagram shows the position where the laser spot hits the PSD while scanning over the sample. From the slope of the linear fit of the data points one can calculate the curvature of the sample. As mentioned before, the sensitivity of the SSIOD method strongly depends on the geometry of the set up, such as the distance between the sample and the detector. In the current configuration the minimal radius that can be measured is R_{min}=4 m when the whole detector length is used. However much smaller radii can be measured nonetheless. In this case the reflected angle of the laser beam extends the length of the PSD during the measurement. When the thereby reduced scanned sample length is considered in the evaluation, radii down to one meter and even below can be measured.

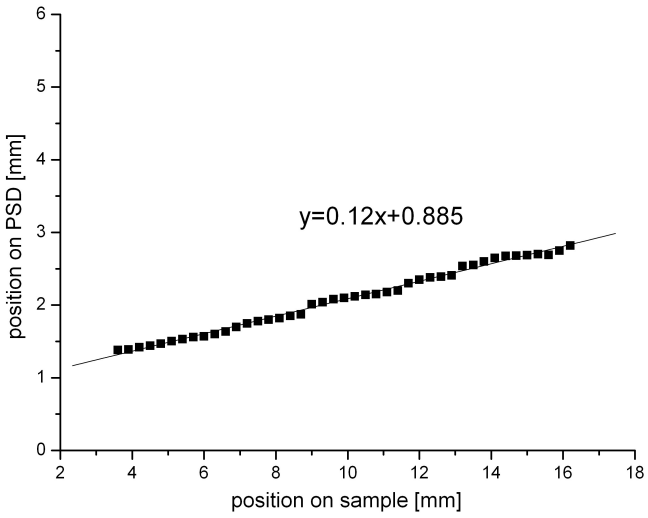

Figure 4.20 Deflection of the laser beam during the measurement

The biggest radius measurable, and therewith the smallest resolution for this set up is given by the noise of the PSD and the smallest quantization step of the A/D converter processing the PSD signal respectively. The current setup is capable of measuring radii up to 4 km.

4.4.3 Low Stress SSIOD Setup

A more complex, though more sensitive setup [Iba97] [San04] [Kur05] for measurement large radii up to 150 km is shown in Figure 4.21 and Figure 4.22.

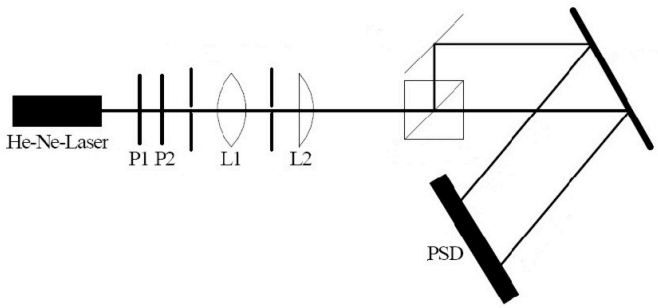

Figure 4.21 Setup to measure large curvatures: P1, P2: polarization filters L1, L2: lenses to focus laser on PSD: „Position sensing diode“

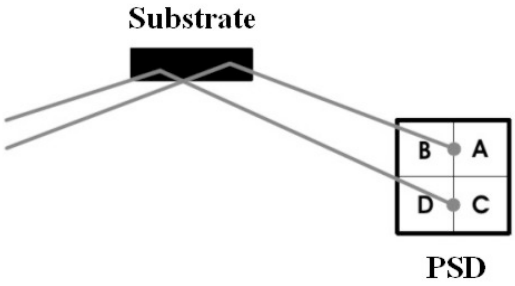

Figure 4.22 This setup utilizes a 4 quadrant detector

In this method a laser beam is splitted into two beams and a 4-quadrant detector is measuring directly the difference in the reflected angle of the two laser beams. By that

$$h''(x) = \frac{2}{R}x + b \qquad \text{Equation 4.5}$$

is measured and the curvature thereby deduced in a very elegant way.
In both methods it is possible to lead the laser beam through a window into the deposition chamber to measure the formation of residual stress in situ.
During this work the high stress setup was enhanced by a heatable substrate holder stage. By using a heated substrate holder the temperature dependency of the residual stress can be measured and thereby information about the thermal expansion coefficients can be obtained which extends the value of the methods far over just measuring the residual stress.

4.5 Deposition Process

As standard substrates in this work (100) oriented double side polished silicon wafers with a thickness of 425 µm were used. The substrates were usually cut from a wafer to a size of around 20 x 10 mm. Nevertheless also depositions on an entire 4-inch diameter wafer were performed to show the uniformity of the deposition process on this area.
To enhance the nucleation of diamond the substrates were ultrasonically scratched for 30 min with a scratching solution consisting of diamond powder (~ 20 nm grain

size), Ti powder (~ 5 nm particle size) and Ethanol in a weight percent ratio of 1:1:100 (wt%). Afterwards the substrates were ultrasonicated for 15 min in Acetone to clean the surface from any residues of the scratching solution [Lin06] [Buc08a].
After the substrate pre-treatment they were immediately installed into the vacuum chamber placed on top of the molybdenum substrate holder and the recipient was pumped down to high-vacuum.
The plasma is ignited at ca. 1 mbar pressure with a process gas mixture of hydrogen (≈ 3 %) in argon (≈ 97 %) and a MW-power of 1 kW. It turned out that the plasma was igniting very reliable with these parameters. After the ignition the pressure was slowly increased up to the deposition pressure (typically 200 mbar) during a 30 min period. This 30 min step is due to two reasons: Firstly the substrate surface is cleaned by the etching effect of the plasma. Secondly the temperature of the substrate is slowly increased in the process of the rising pressure. In doing so the substrate is already close to the targeted deposition temperature before switching to the deposition parameters and introducing the carbon carrier gas into the chamber. During the whole process of increasing the pressure the MW power coupling into the plasma is adjusted to the changing conditions. After reaching the desired deposition pressure the carbon carrier gas was introduced therewith starting the deposition process.
The deposition process was continued for standard 5 h for the deposition of UNCD films although also nucleation experiments were performed where the deposition time was as low as several minutes [Mac05].
Most of the process parameters were varied during the set of experiments performed in this work to investigate their influence on the deposition of nanocrystalline diamond. Table 4.1 shows the most important deposition parameters and the limits they were varied in the course of this work.

Parameter	
Pressure	150 mbar – 250 mbar
Gas flow	200 sccm – 2000 sccm
H_2 fraction	2,5 % - 7 %
CH_4 fraction	0.5 % - 2.3 %
Ar fraction	90.7 % - 97 %
MW-power	0.8 kW – 2.5 kW
Deposition time	5 h
Substrate	
Temperature	600°C – 900°C

Table 4.1 Process Parameters

The limits for the process parameters are mostly given by the aim of depositing ultrananocrystalline diamond films. For instance the pressure has to be higher than 160 mbar to get a reasonable deposition rate. However higher process pressures influence the shape and size of the plasma ball. Due to the lower mean free path of the particles the plasma ball is shrinking and that limits the area of deposition. Therefore the regime between 150 mbar and 250 mbar was chosen for the experiments. The process gas composition was chosen in a way that nanocrystalline diamond films are deposited. High admixtures of hydrogen lead to larger diamond crystals and therefore to microcrystalline diamond growth. Higher admixtures of methane lead to more and more graphitic films while lower admixtures again lead to a reduced deposition rate. As shown later the same is true for extremely low substrate temperatures (lower than 600°C) so the deposition temperature was varied between 600°C and 900°C.

5 Experimental Results

Although plenty of publications exist concentrating on the properties of diamond grains when characterizing UNCD films, the importance of the matrix surrounding the crystal was overlooked so far.

Because the matrix of UNCD films is an amorphous carbon structure it is systematically characterized in this work with approved methods for amorphous carbon such as Raman and FTIR spectroscopy.

The influence of the process parameters on the growth process of the matrix as well as the diamond grains and subsequently the influence of the growth process on the resulting film properties will be discussed according to the modelling of the deposition process already introduced in Figure 3.5. Only this holistic approach, where the specific process steps are investigated independent from each other lead to an understanding of the growth process and gives the possibility to tailor selective film properties.

Consequently, the influence of the process parameters such as pressure, gas composition, gas flow, MW-Power etc. on the plasma properties will be investigated first (Chapter 5.1). Subsequently, the influence of the plasma properties on the film deposition will be investigated (Chapter 5.2). Due to its importance for the film performance and the adhesion of the films, the residual stress measurement will take a central part in the analysis. According to Figure 3.5, the substrate properties are the other important factor affecting the deposition process. Because different pre-treatment methods were already investigated soundly in previous publications like [Lee06] [Che07] and also in cooperation with our workgroup like [Mac05] [Deu06] the most applicable one for the UNCD deposition on silicon was used for this work and only the influence of the substrate temperature on the deposition process is investigated in more detail.

Finally, the influence of the plasma and the substrate properties on the resulting film properties will be presented. It will be shown that the measurement and interpretation of the residual stress in the films exceeds by far the simple determination of the stress state in the films but also gives information about the matrix fraction to the overall film volume in the films, correlate the intrinsic stress to Raman spectroscopy and allows the measurement of the thermal expansion coefficients in the deposited

films. These methods were used for the first time on UNCD films to determine film properties in the course of this work.

5.1 Influence of Coating Parameters on Plasma Properties

Results of this chapter are partly published in [Woe09].

The influence of the macroscopic coating parameters pressure, gas flow, methane fraction in the process gas and the MW power on the plasma parameters were investigated (Figure 5.1). The process parameters are device specific and cannot directly explain the physical processes leading to the deposition of UNCD films. By analysing how the coating parameters are influencing the plasma parameters and subsequently how the plasma properties are influencing the film properties, the decisive physical processes can be understood.

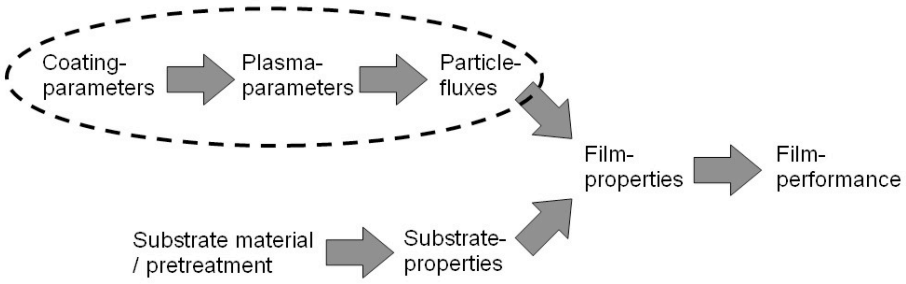

Figure 5.1 Influence of Coating Parameters on the Plasma Parameters

Since the first deposition of nanostructured diamond films from Argon-rich plasma, the role of the C_2 carbon dimer in the deposition process - whose presence in the plasma can clearly be deduced from the green emission of the plasma – is discussed. The fact that diamond films could be deposited from plasmas where only small amounts of hydrogen, or even none, were added and the fact that the strongest visible emission line in the optical spectrum in the UNCD growth conditions is the C_2 line lead to a new deposition model with the C_2 dimer as main growth and nucleation species [Gru94] [Gru99]. Although recent papers disagree, doubting that the C_2 molecule is in any way participating in the growth of UNCD referring to it as an spectator molecule [Rab04] [May06] [May07] or as species responsible for the high secondary nucleation [Buc08a], the role of the dimer is still discussed.

5.1.1 OES Measurements of C_2 Emission Intensity

Since the C_2 carbon dimer role in the deposition process is yet not fully understood the carbon dimer $d^3\Pi \rightarrow a^3\Pi$ Swan band emission at 516 nm is investigated using optical emission spectroscopy.

The spectrometer was coupled to the process chamber via a glass fibre and the whole system was calibrated as usual with a tungsten strip lamp.

A typical emission spectrum was already shown in Chapter 3.4.1.1 (Figure 3.15). The intensity of the C_2 (516 nm) line was measured and compared to the H_α (656,3 nm) line to exclude changes in the experimental setup during the measurement like coated windows that would affect the intensities [Van97].

Goyette et al. compared the optical emission intensity of the $d^3\Pi \rightarrow a^3\Pi$ (0,0) vibrational band of the C_2 Swan system with the absolute C_2 concentration in a $Ar/H_2/CH_4$ plasma used in UNCD deposition and found that it correlates linearly for variations of several plasma parameters. The comparative absolute C_2 measurements were done by white-light absorption spectroscopy [Goy98].

A detailed investigation of the plasma processes during nanocrystalline diamond deposition from $Ar/H_2/CH_4$ can be found in [Zho07]. By investigating the plasma with quadrupole mass spectroscopy and optical emission spectroscopy Zhou et al. were able to find an explanation for CH_4 decomposition in hydrogen-poor plasmas. In these plasmas electron impact seems to be mainly responsible for the CH_4 dissociation other than hydrogen abstraction with atomic hydrogen.

In this work, the influence of the process parameters (pressure, gas flow and microwave power) on the carbon dimer $d^3\Pi \rightarrow a^3\Pi$ Swan band emission at 516 nm is systematically investigated.

Despite the fact that Goyette et al. were able to show the use of OES for relative determination of the C_2 density in the special case of nanocrystalline diamond CVD deposition it is in general not valid to ratio the emission intensities of species from a plasma as a function of process conditions and to draw quantitative conclusions from this. Actinometry - where the emission intensities of each species are scaled by the intensity of emission from a inert gas – is a possible solution. In this work the Argon line at 751.4 nm was used to scale the measured C_2 emission line. Unfortunately the intensity of the Argon line at 751.4 nm is weak for all spectra taken in this work and

the measured values are prone to statistical error. It would be preferable to use the intensities of the C_2 (516 nm) line and the H_α (656.3 nm) line because both are strong in the spectra. Therefore it was measured, if the C_2/Ar intensity and C_2/H_α ratio show the same trend for the spectra taken.

Figure 5.2 shows the influence of the pressure on the measured C_2/Ar and the C_2/H_α intensities. All OES measurements were done with a MW-Power of 1.5 kW and the measured intensities were normalized to the maximum.

It is observed that increasing the pressure results in a stronger C_2 emission intensity for the C_2/Ar ratio as well as the C_2/H_α ratio. The emission intensity increases by nearly an order of magnitude when changing the pressure by 50 mbar from 175 mbar to 225 mbar.

Because both ratios show the same trend for the measurements done here and because Goyette showed the applicability for the UNCD deposition, the C_2/H_α is used due to the stronger intensities to correlate plasma properties with the film properties.

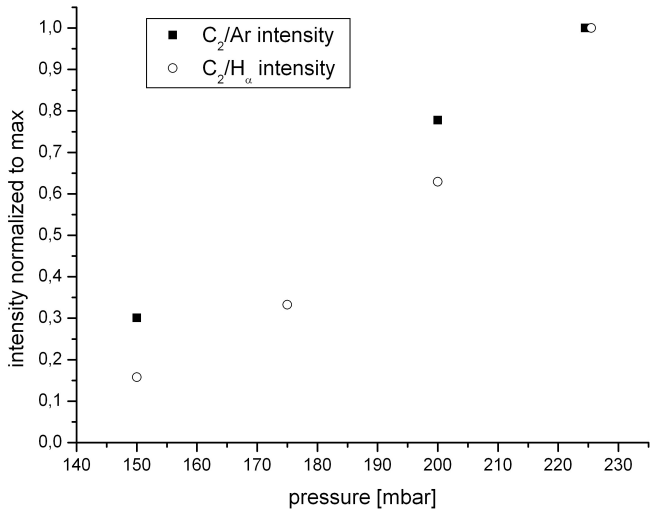

Figure 5.2 C_2/Ar and C_2/H_α intensity normalized to maximum measured by OES

Figure 5.3 shows the C_2/H_α ratio as measured by OES. One can see that the gas flow as well as the pressure has an influence on the ratio. The intensity is increasing by a factor of 2 with gas flow being increased from 300 to 1300 sccm. A maximum is reached at this point and the intensity is decreasing again with higher gas flow. Pressure has also a strong influence on the intensity, especially when increasing the pressure from 160 to 200 mbar. A strong increase in plasma brightness and a

change to an intense green emission can be observed resulting from the stronger C_2 peak measured by OES. A maximum of intensity is found at 210 mbar.

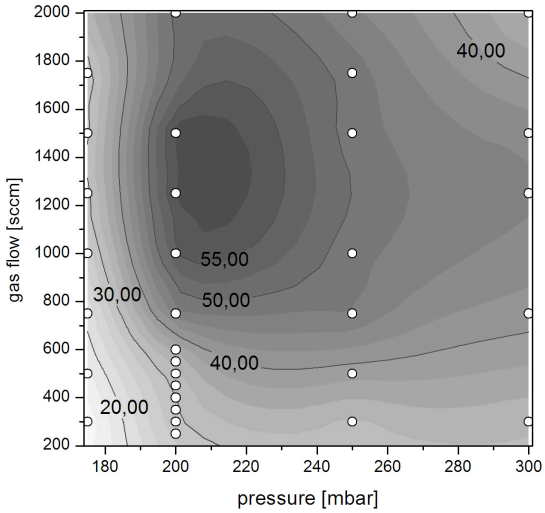

Figure 5.3 Influence of the process parameters pressure and gas flow on the intensity ratio of the C_2 (516.5 nm) line and the H_α (656.3 nm) line taken from the Optical Emission spectroscopy. White points represent measured data

While the previously shown connection between coating- and plasma parameters were performed at constant MW-power of 1.5 kW, the results shown in Figure 5.4 point out the influence of the MW-power and the pressure on the C_2 density. There is a strong influence of the pressure on the C_2/H_α values as shown before. However the MW-power does not seem to have a strong influence on the ratio. Although the power was increased from 1 kW to 2 kW the results obtained by OES suggest that the C_2/H_α values almost stay constant at a given pressure. This finding corresponds to the earlier results that the MW-power is significantly increasing the size of the plasma ball inside the reaction chamber but not the plasma chemistry.

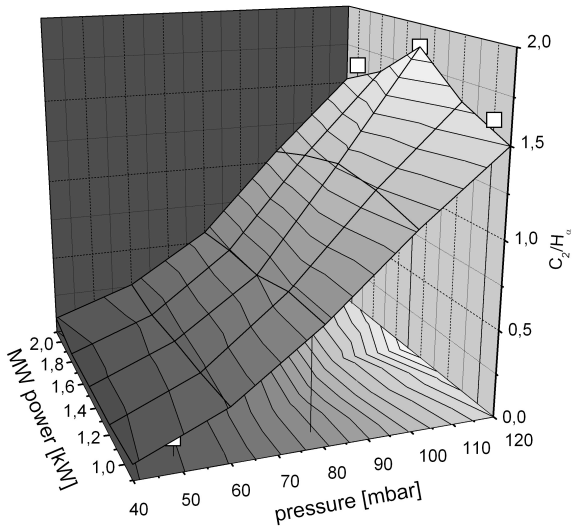

(a)

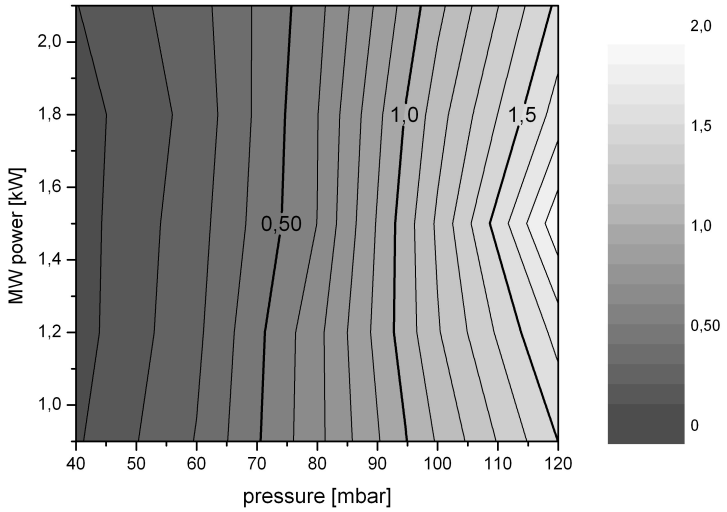

(b)

Figure 5.4 Influence of the process parameters pressure and MW-power on the intensity ratio of the C_2 (516.5 nm) line and the H_α (656.3 nm) line taken from the Optical Emission spectroscopy. Data shown in a 3D view (a) and in a 2D diagram (b)

Finally OES was used to determine the plasma temperature by measuring the ratio of hydrogen Balmer Lines as explained in Chapter 3.4.1.1. Figure 5.5 shows the results and the influence of the coating parameters pressure and MW-power on the plasma temperature while methane fraction and gas flow were kept constant. The plasma temperature is slightly decreased by around 150 K when the process pressure is

increased from 50 mbar to 120 mbar. The MW-power does not have a strong influence on the plasma temperature when increased from 1 kW to 2 kW.

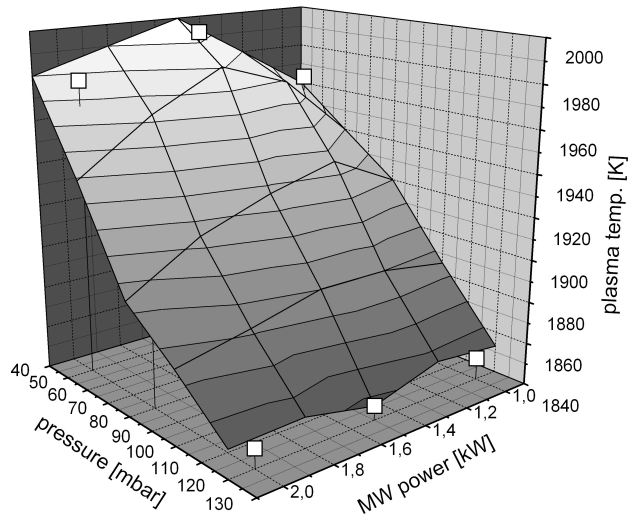

Figure 5.5 Plasma temperature as measured by OES

5.1.2 Mass Spectrometer Measurements

Although Goyette et al. already showed the applicability of OES for the determination of C_2 concentrations in $Ar/H_2/CH_4$ plasma [Goy98] in the regime of typical parameters for UNCD deposition, we performed comparative studies by mass spectroscopy. The intensity of the carbon dimer (mass number 24) was taken from the mass spectra and compared with the results obtained by OES. Figure 5.6 and Figure 5.7 show the influence of gas flow and process pressure variation on the C_2/H_α taken from OES and C_2 intensity taken from the mass spectra respectively. In the case of gas flow variation, both signals show the same trend in a wide range from 400 sccm to 1500 sccm. At higher gas flows the C_2/H_α signal is decreasing again while the C_2 signal measured by mass spectroscopy is still increasing. In the case of pressure variations the trend – althought not that clear – is still noticeable. The differences in the measurements can be explained by the different position of the measurement. While the OES data is taken in the plasma (above the substrate) the mass spectroscopy measurement is done further away from the substrate in the exhaust.

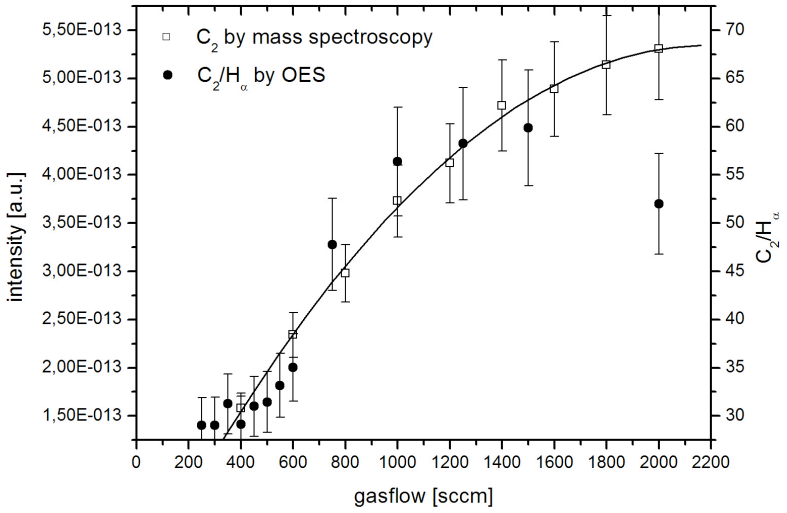

Figure 5.6 Intensities of C_2/H_α ratio taken from the Optical Emission Spectroscopy (black dots) and mass spectroscopy, measurement of C2 [amu 24] (white squares) as a function of the gas flow at constant pressure of 210 mbar

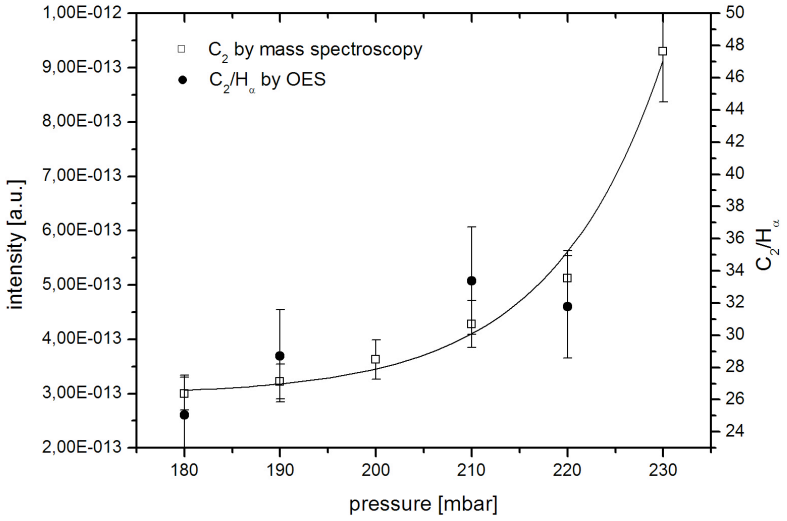

Figure 5.7 Intensities of carbon dimers taken from the Optical Emission Spectroscopy (black dots) and mass spectroscopy (white squares) as a function of the pressure at constant gas flow of 400 sccm

The comparability of the measurements in the given process regime support the assumption that the OES can be used to quantitatively determine the C_2 density in the plasma in situ.

5.1.3 Plasma Properties and Process Parameters

The OES and mass spectrometer measurements show how the C_2 concentration in the deposition plasma is influenced by the process parameters pressure, gas flow and MW-power demonstrating a strong influence of pressure and gas flow and almost no influence of MW-power. These results are important to judge how sensitive the process is to variations in the specific parameters.

The fact that the results for OES and mass spectrometry coincide and agree with absorption spectroscopy gives further confidence that the measured C_2 intensities correspond to the absolute density of carbon dimers in the plasma.

5.2 Influence of Particle Fluxes on Film Properties

After investigating how the coating parameters determine the plasma properties, the subsequent step in modelling the deposition process is the influence of the plasma parameters and particle fluxes on the film properties (Figure 5.8).

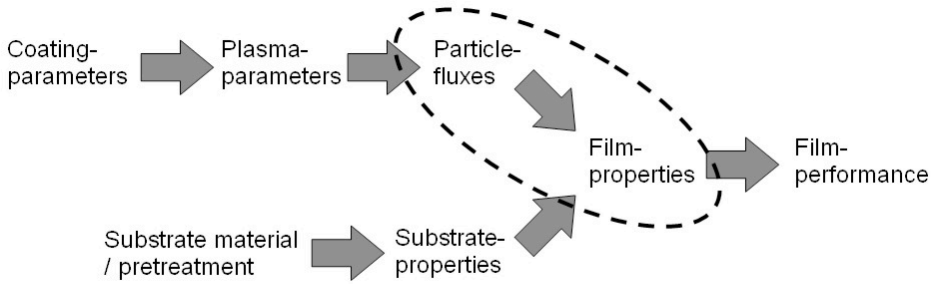

Figure 5.8 Influence of Plasma Parameters and Particle Fluxes on film properties

First of all, the influence of the gas flow on the film properties such as thickness (growth rate) and nucleation density is worked out (Chapter 5.2.1.1). It is shown how the C_2 measurements can explain these findings (Chapter 5.2.1.2).

The influence of the C_2 line intensity in the plasma on the deposited film properties such as residual stress and structural properties of diamond crystals and the matrix is investigated (Chapter 5.2.1.3– 5.2.1.7).

Afterwards, a variation of hydrogen in the process gas is performed. The resulting changes in morphology, growth rate, residual stress and the influence of the hydrogen admixture on the internal structure of the films as measured by various spectroscopic methods (Chapter 5.2.2) are demonstrated.
Finally, the influence of nitrogen on the deposition process is worked out and the results are presented in Chapter 5.2.3.

5.2.1 Influence of C_2 Density in the Plasma on the UNCD Film Properties

Results of this chapter are partly published in [Buc08b] and [Woe09b].

It is well established that the methyl radical is the *growth precursor* for CVD grown microcrystalline diamond. In usual hydrogen-rich gas compositions it is produced by abstraction of one hydrogen atom from the methane molecule via its reaction with atomic hydrogen. $CH_4+H \rightarrow CH_3+H_2$. In hydrogen deficient atmosphere – as it is used for UNCD growth – it is produced by electron collisional impact. By investigating the plasma with quadrupole mass spectroscopy and optical emission spectroscopy Zhou et al. were able to find an explanation for CH_4 decomposition in hydrogen-poor plasmas, in these plasmas electron impact seems to be mainly responsible for the CH_4 dissociation other than hydrogen abstraction with atomic hydrogen. [Zho07]
This contribution leads to a non-vanishing growth rate even in hydrogen free gas mixtures [Gru99].
At constant gas composition, gas pressure, microwave-power and substrate temperature - the plasma chemistry is fixed and the growth rate of diamond grains should be constant.
There is evidence that the *nucleation process* differs from these reactions [Buc08b] and is independent from the mentioned growth precursor. As mentioned before, C_2 might be a candidate responsible for the high secondary nucleation rate in the growth process of UNCD. Because both – the growth precursor and the nucleation species – are decomposed from the CH_4 molecule, growth and nucleation could be competing processes. If – as it is probable – the lifetimes of the corresponding intermediate reactants are different, it is possible to influence the balance of nucleation and growth by variation of the residence time of the species involved i.e. by plasma pulsing

[Fan02] or varying the gas flow [Kob99] [Hei01] (keeping all other deposition parameters constant).
The open question is, how the “intermediate space” between the diamond grains, i.e. the amorphous matrix, is influenced by this variation. Amorphous carbon films are often referred to diamondlike carbon films (DLC). The term DLC alone describes a whole class of materials and includes different materials that can, for example, consist entirely of carbon (a-C), of carbon and hydrogen in different concentrations (a-C:H), or have different constituents such as metals (Me-C:H), silicon, oxygen, halogens, or nitrogen, and techniques for the characterization of these structures are well established.

The nanocrystalline films shown here were deposited at a pressure of 200 mbar from an $Ar/H_2/CH_4$ plasma. The gas flow was varied to investigate the influence on film structure and film properties without changing the process gas composition as shown in Table 5.1. The MW-power was kept constant at 1 kW and the films were deposited for 5 h.

Parameter	
Pressure	200 mbar
Gas flow	250 sccm – 1050 sccm
H_2 fraction	2.5 %
CH_4 fraction	0.8 %
Ar fraction	96.7 %
MW-power	1 kW
Deposition time	5 h
Substrate	Si (100) abraded for 15 min

Table 5.1 Process Parameter for gas flow variation

5.2.1.1 Influence of Gas Flow on Nucleation and Growth Rate

Cross sections of the films were taken by SEM to investigate the film thickness and the deposition rate. As suggested before, the deposition rate depends strongly on the

gas flow of the process gas, as shown in Figure 5.9. The higher the gas flow the lower the growth rate.

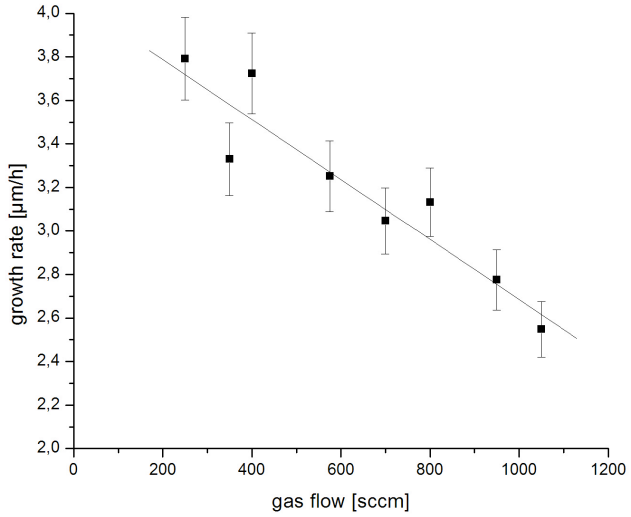

Figure 5.9 Growth rate as a function of the gas flow measured at 200 mbar

SEM is also used to determine the nucleation density by manually counting the number of nuclei after 2 min. deposition. The results are shown in Figure 5.10. In contrast to the growth rate, the nucleation density increases with the gas flow. Thus, the film structure must be strongly influenced by variations of the gas flow.

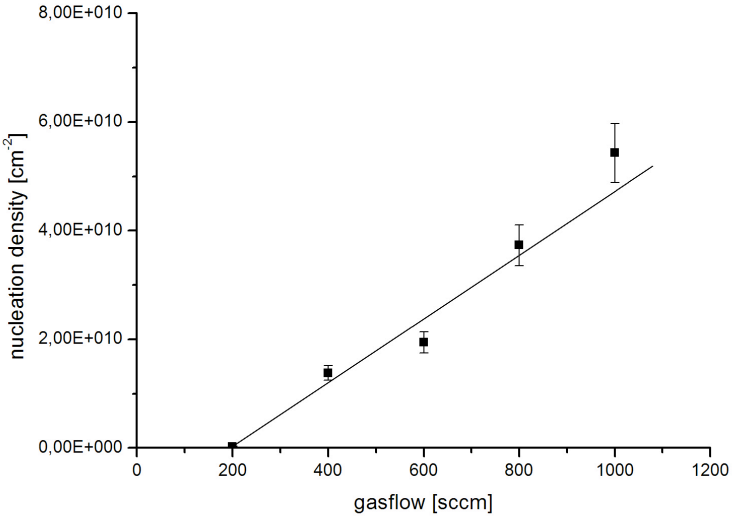

Figure 5.10 Nucleation density as a function of the gas flow

An explanation for these measurements can be found when taking the C_2 measurements into account.

The influence of the gas flow on the C_2 peak intensity as measured by OES is shown in Figure 5.11 for the given process parameters.

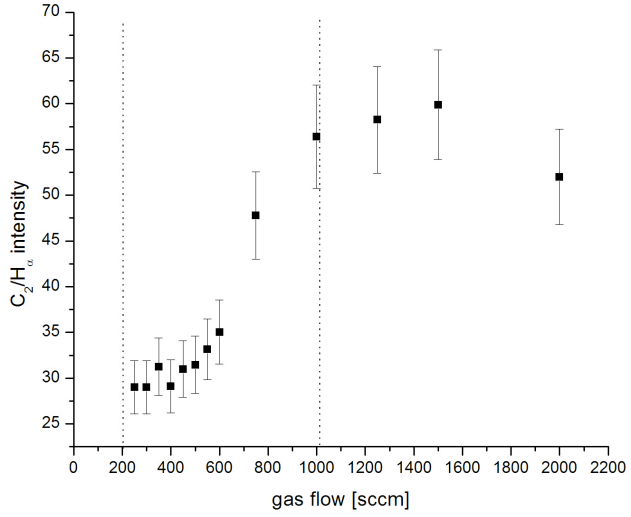

Figure 5.11 Influence of process gas flow on the C_2 dimer density in the plasma as measured by OES at 200 mbar

The films shown in Figure 5.9 and Figure 5.10 were deposited between 200 sccm and 1000 sccm. Figure 5.11 shows that the dimer peak intensity is increased by a factor of 2 in this regime. The C_2 dimer is possibly participating in the nucleation process of UNCD growth. The more CH_4 is decomposed into C_2 the less CH_3 is available for the growth of the diamond crystals thus reducing the growth rate.

One possible explanation for the maximum of C_2/H_α at a gas flow of 1500 sccm could be found in the amount and residence time of the carbon carrier gas in the plasma. By increasing the overall gas flow, more methane is introduced into the plasma and transformed into the C_2 dimer. At higher gas flow, the residence time of the methane in the plasma is too short to activate all of the molecules. Therefore, the C_2 concentration in the plasma is decreasing again.

5.2.1.2 Influence of C_2 Density on Growth Rate and Nucleation Density

To find a direct correlation between the growth rate and the nucleation density of UNCD films and the C_2/H_α during deposition, measurements were done which are shown in Figure 5.12. The measurements of the growth rates were done by film thickness measurements using cross section pictures taken by SEM.

The growth rate is decreasing with the amount of dimers being up to 3.8 µm/h at a C_2/H_α value of 40 and dropping down to 3 µm/h for C_2/H_α of 60. Large amounts of graphitic carbon were deposited in the deposition chamber at C_2/H_α values above 60 that suggests that the deposition of graphitic carbon is favourable in these growth conditions.

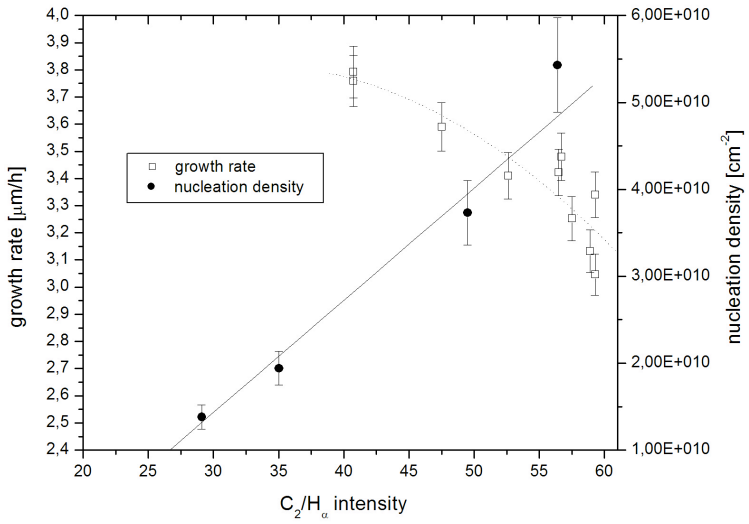

Figure 5.12 Growth rate and nucleation density as a function of C_2/H_α taken by Optical Emission Spectroscopy

Figure 5.12 shows the influence of C_2/H_α ratio on the nucleation density. It is shown that the nucleation density is correlates with the C_2/H_α ratio measured by Optical Emission Spectroscopy. By increasing the carbon dimer intensity, it is possible to increase the nucleation density.

A possible explanation for this result could be found in the interplay of two competing species involved in the growth of NCD and UNCD films. It was suggested that different species for the nucleation on the one hand and the growth of diamond

grains on the other hand exist. The ratios of these species determine the macroscopic structure of the growing films by influencing the rate of secondary nucleation and therefore the matrix density and the grain size of the growing crystals. A higher amount of the nucleation species leads to smaller crystals and more material between the grains. A higher amount of growth species allows the grains to grow faster (thus a higher growth rate) suppressing the secondary nucleation. In the literature, C_2 was suggested to be the nucleation species [Gru98] as strong emission of the C_2 dimer could be found in the plasmas used for the deposition of fine-grained NCD and UNCD films. On the other hand plenty of different CH_x radicals are discussed to be candidates as growth species of diamond films. Without taking part in the discussion concerning specific possible growth and nucleation species, Figure 5.12 can be interpreted as the competition of the growth and the nucleation mechanisms: Both – nucleation species as well as growth species – are generated from the methane molecule in the process gas. The more nucleation species C_2 is generated in the plasma, the less carbon carrier gas is available to generate the growth species.

Based on these results it seems that the growth rate can be adjusted directly by controlling the amount of carbon dimers in the plasma.

5.2.1.3 Influence of C_2 on the Microstructure of the Grains

X-Ray diffractometry (XRD) is used to characterize the crystalline structure of the films. The peak position, intensity and full width of half maximum (FWHM) in the diffraction patterns give information about the crystallographic structure, preferential orientation (texture) of the crystals in the film, and the stress within the grains.

The analysis of nanostructured films is problematic because the peaks in the diffraction patterns broaden not only due to the reduced grain size in these films but additionally by intrinsic stress (which influences the position and the FWHM of these films, although a separation of these contributions is possible using the Williamson-Hull plot). Thus XRD is a powerful and frequently used method for diamond film analysis [Bac92] [Deu98] and recently the applicability of the XRD method for UNCD has also been shown [Ger05].

The diffraction patterns used in this work were measured by a Phillips PW 1710 diffractometer with a theta 2-theta goniometer using Co K_α radiation. The 0.179 nm cobalt K_α-line was employed to investigate the crystalline structures of the samples.

Three diamond peaks are clearly visible in the diffraction pattern shown in Figure 5.13: d<111> at 51.52°, d<220> at 90.42°, and d<311> at 112.65°.

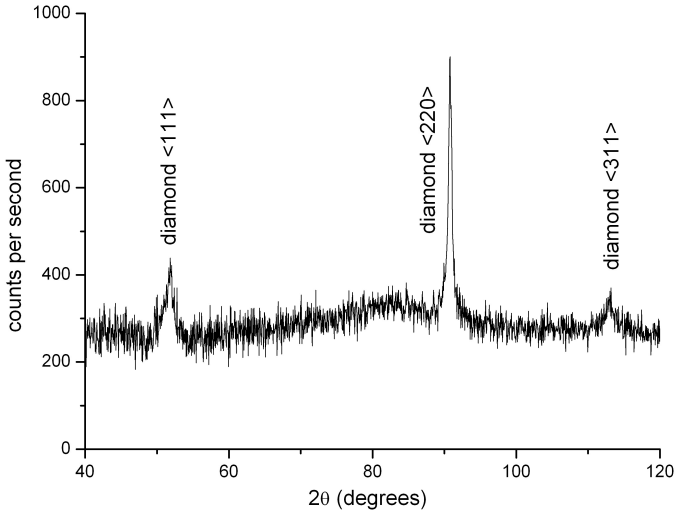

Figure 5.13 XRD pattern of NDC film

The intensities of the XRD peaks are compared to reference powder samples taken from the literature: <111> 100 %, <220> 25 %, <311> 16 %, and <004> 8 % [Pow01]. A rough estimate of preferential orientations in the films and the influence of the C_2 on it can therefore be made by comparing the measured intensities with the expected intensities of a randomly oriented film. Figure 5.14 shows the intensity ratio of the <220> peak to the <111> peak in the XRD pattern as a function of the C_2/H_α intensity during deposition. Additionally a dashed line in the diagram is indicating the ratio for randomly oriented crystals taken from the powder sample where I<220>/I<111>=0.25.

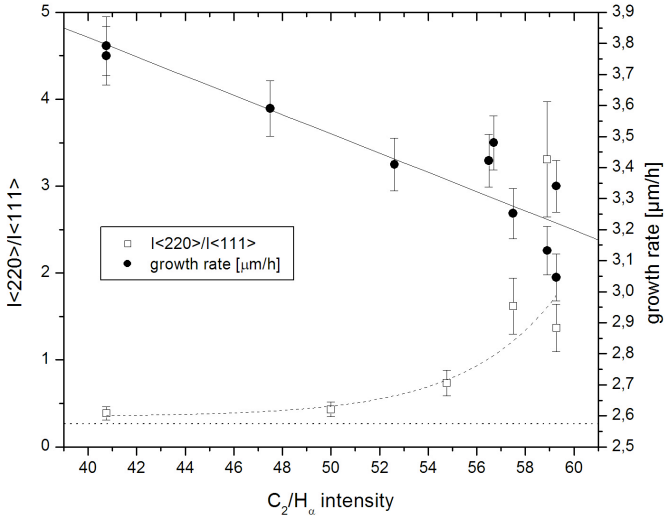

Figure 5.14 Intensity ratio of <220> and <111> peak in XRD pattern compared to the growth rate. The dashed line indicates the literature value for randomly oriented diamond [Pow01]

Only samples deposited with low C_2/H_α ratios up to 50 appear to be randomly oriented and it is clearly seen that all films deposited with high ratios show a preferred <220> texture in the films that is increasing with C_2/H_α. At the same time the deposition rate is decreased.

From FWHM measurements the grain size of the diamond crystals was determined. It was found that the grain sizes differ for different orientations. The grain size of the <220> oriented crystals was measured to be around 15 nm and the size of the <111> oriented crystals was found to be around 5 nm.

5.2.1.4 Macroscopic Relations between Matrix and Grains

To give a rough estimate about the volume ratio of matrix to grains in different films the density of the films was calculated by additionally measuring the weight of the films. It appears that films with different density can be prepared by varying the C_2/H_α ratio during deposition. Figure 5.15 shows the results of these measurements, indicating that denser films have larger diamond grains.

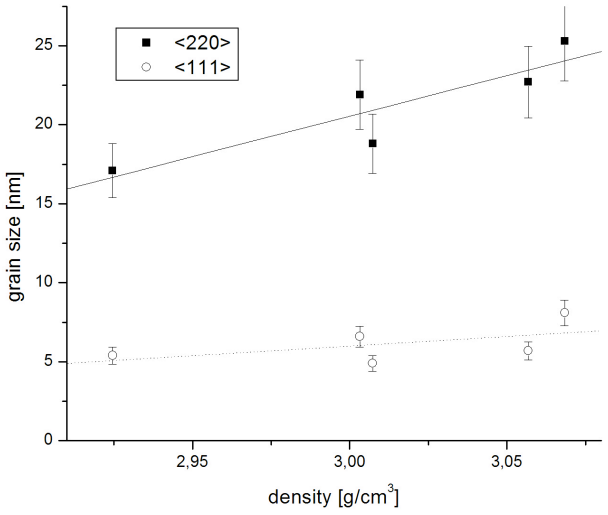

Figure 5.15 Grain size of the diamond crystals as a function of the density of the films

This result is expected upon considering that the diamond grains in the film have a higher density than the matrix, which is assumed to be some form of amorphous carbon. Assuming a density of 3.5 g/cm^3 for diamond grains and 2 g/cm^3 for the amorphous carbon matrix, the volume ratio of the matrix was calculated to be ca. 40 % for the lowest density of the films measured (the smallest diamond grains) and ca. 30 % for the highest film density (largest diamond grains).

From the calculated volume percentage of the matrix and the measured grain size in the films, one can estimate the distance and thus the matrix “thickness” between the grains by applying a simple model. In the model, cubic diamond crystals with a matrix of thickness *d* surrounding each crystal face is assumed. Because the matrix surrounds every crystal, the overall distance between two diamond grains t_{gb} is *2d*.

To calculate the matrix thickness using this model, the average grain size in the films was used taking into consideration the dominant <111> and <220> textures. The average grain size was calculated to be 7.5 nm for the films with 40 % matrix volume and 11 nm for the films with 30 % matrix volume. The matrix thickness t_{gb} can now be calculated for a 7.5 nm average grain size (40 % matrix):

$$\frac{2}{5} = \frac{6 \times d}{7.5 \times 10^{-9}\,\mathrm{m}} \qquad \text{Equation 5.1}$$

$$15 \times 10^{-9}\,\mathrm{m} = 30 \times d \qquad \text{Equation 5.2}$$

$$d = 0.5\text{nm} \qquad \text{Equation 5.3}$$

$$t_{gb} = 2 \times d = 1\text{nm} \qquad \text{Equation 5.4}$$

and for a 11 nm grain size (30 % matrix):

$$\frac{1}{3} = \frac{6 \times d}{11 \times 10^{-9}\,\text{m}} \qquad \text{Equation 5.5}$$

$$11 \times 10^{-9}\,\text{m} = 18 \times d \qquad \text{Equation 5.6}$$

$$d \approx 0.6\text{nm} \qquad \text{Equation 5.7}$$

$$t_{gb} = 2 \times d \approx 1.2\text{nm} \qquad \text{Equation 5.8}$$

These results indicate that although for larger diamond crystals in the films the overall volume fraction of the matrix is decreased as expected, the matrix thickness (and thus the distance between the diamond grains) is slightly increased.

5.2.1.5 Microscopic Structure of the Matrix

The internal structure of amorphous carbon films can be mainly characterized by the sp^3/sp^2 ratio and the configuration of the sp^2 phase (rings or chains), and also by the content of admixtures, usually hydrogen. To determine these properties without the destruction of the coating, which is important for most technical applications, spectroscopic methods (FTIR and Raman spectroscopy) are used; because the C-C and C-H bonds are responsible for the IR and Raman spectra, the H content and sp^3/sp^2 ratio can be deduced via the deconvolution of these spectra [Ris98] [Hei98] [Rob02]. Both, the Raman and the IR spectra, give partial descriptions of the internal vibrational motion of the molecules of the constituent atoms. Neither type of spectrum alone gives a complete description of the pattern of molecular vibration, and only the combined results of both methods allows us to understand the structure and composition of our carbon films. It is therefore essential to obtain a consistent result for all experimental techniques.

First the FTIR spectra were analyzed to find out how the structure of the matrix changes with the deposition parameters. All deposited films show a strong absorption band between 2750 and 3100 cm^{-1} indicating various C-H stretching modes. The

spectra were deconvoluted using 9 Gaussian peaks with frequencies and assignments given by Ristein et al. [Ris98].

Figure 5.16 shows the total integrated absorption of the C-H stretching band as a function of the C_2/H_α ratio. The total integrated absorption is the sum of all areas of the fitted Gaussian peaks used for the deconvolution. The error bars are estimated to be 20 % and include uncertainties in the baseline correction and in the fitting process.

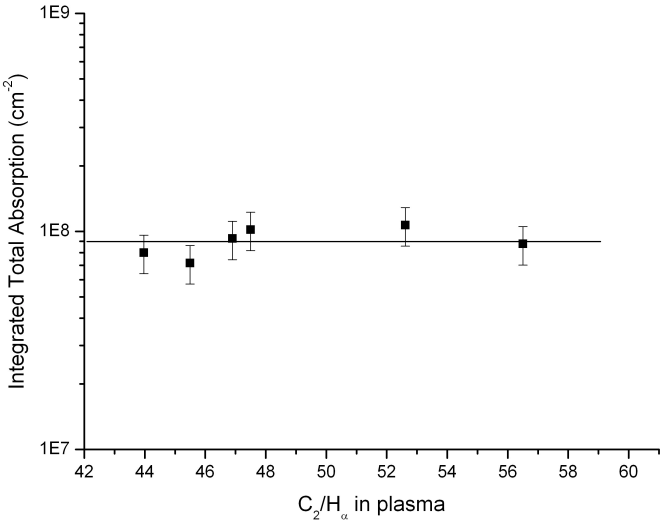

Figure 5.16 Total integrated absorption of C-H stretching modes as a function of C_2/H_α intensity

Although the volume percentage of the matrix is influenced by the C_2/H_α valuesas shown in the previous chapter, the total integrated absorption of the C-H stretching band does not change.

After measuring the total integrated absorption intensity of all C-H bonds in the matrix a more detailed investigation was performed to find out whether a change in the C-H configuration can be found in the deposited films. Figure 5.17 shows the relative absorption intensities separated into the sums of all sp^3CH_x and sp^2CH_x stretching modes.

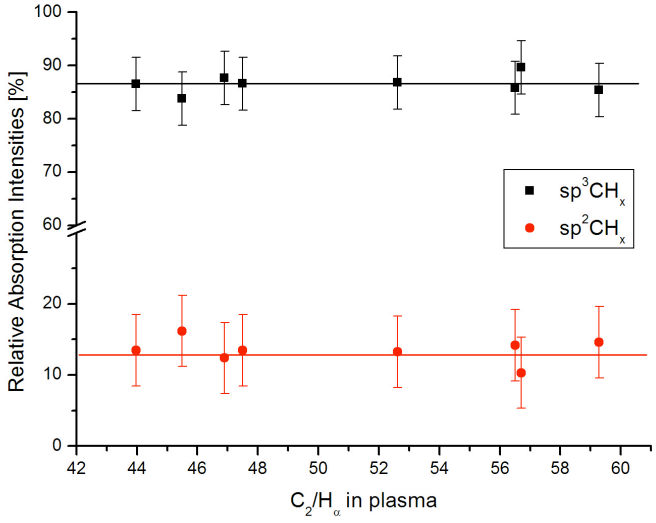

Figure 5.17 Relative absorption of C-H stretching modes as a function of gas flow

The ratio between sp^3- and sp^2-bonded hydrocarbons remains constant and no influence of the C_2/H_α ratio could be found. This indicates that the structure of the C-H bonds in the matrix does not change significantly.

Because neither Raman nor FTIR-spectroscopy is able to give an absolute measurement of the hydrogen content of the films, a reference measurement was performed by nuclear reaction analysis (NRA). Hans Werner Becker at the Ruhr-Universität Bochum at the Institut für Experimentalphysik III did the measurement.

With the NRA method it is possible to obtain concentration vs. depth distributions for hydrogen in thin films. The hydrogen is irridated with a projectile (^{15}N) and undergoes a nuclear reaction under resonance conditions for sharply defined resonance energy. The reaction product is a nucleus in an excited state that is emitting ionized radiation when decaying. To obtain depth profiles the initial kinetic energy of the projectile nucleus has to exceed the resonance energy. The projectile is then slowing down in the sample till it reaches the resonance energy. Thus the initial kinetic energy corresponds to a depth in the film where the reaction occurs.

The reaction commonly used to detect hydrogen and the reaction used in this work is:

$$^{15}N + ^{1}H \rightarrow ^{12}C + \alpha + \gamma(4.43eV) \qquad \text{Equation 5.9}$$

^{1}H and ^{15}N are fusing to a highly excited ^{16}O compound nucleus. The excited ^{12}C nucleus is finally emitting a γ particle with a resonance at 6.385 MeV.

The energetic emitted γ ray is characteristic of the reaction and the number that is detected at any incident energy is proportional to the concentration at the respective depth of hydrogen in the sample. The H concentration profile is then obtained by scanning the ^{15}N incident beam energy. [Lan76] [Lan92] [Lan95] [Eck98]

The measurement of a sample is shown in Figure 5.18. The depth profile shows a constant hydrogen content of 3 % in the sample. The measured depth in the sample can be calculated from the beam energy above the resonance at 6.385 MeV. In this measurement the 1.1 MeV correspond to a penetration depth of 550nm.

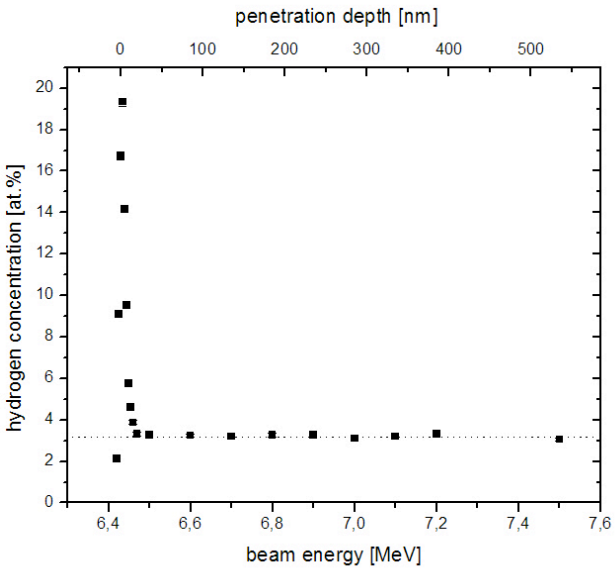

Figure 5.18 NRA measurements of hydrogen concentration in the film

After investigating the C-H bonds by FTIR spectroscopy, Raman spectroscopy was performed to investigate the structure of the C-C bonds. Figure 5.19 shows the influence of the C_2/H_α intensity on the G-peak obtained using an Ar laser (λ=514.5 nm). The figure shows that the position does not vary significantly and it is located between 1580 and 1595 cm^{-1} for all samples. Comparing these measurements with the three-stage model of increased disorder given by Ferrari and Robertson one can deduce structural information from the features in the Raman spectra [Fer00a] [Fer00b]. The G-Peak position can give information on the sp^3 content in the matrix as shown in the small inset in Figure 5.19. The measured position of the G-peak is suggesting that the amount of sp^3-bonded carbon in the

matrix is not exceeding a few percent (<5 %) for all C_2/H_α ratios being not changed with a variation in C_2/H_α ratios.

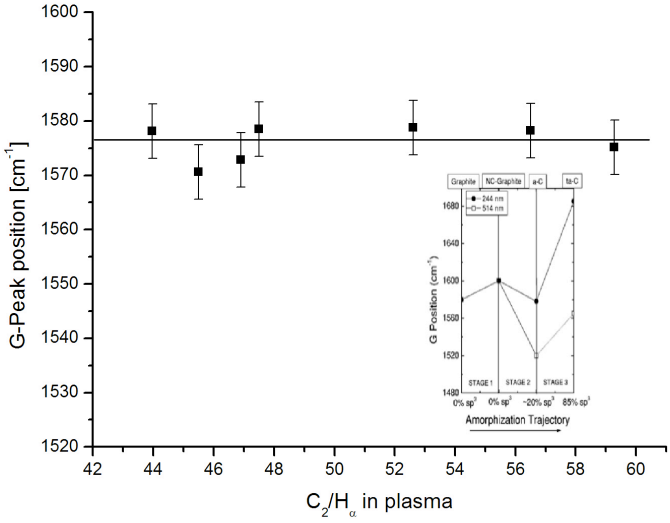

Figure 5.19 G-Peak position as measured by Raman spectroscopy as a function of C_2/H_α intensity

To verify the results from the G-peak position measurements, the dispersion of the G-peak when measured using different excitation wavelengths was also investigated. Supplementary Raman measurements were performed using a HeNe laser (λ=632.8 nm) to measure the G-peak position at this wavelength. The dispersion is low and comparable to the dispersion of a-C films, indicating that the matrix consist of an amorphous carbon phase with a low sp^3 fraction and low hydrogen content. Figure 5.20 is comparing the measurements with the results obtained by the group of Robertson [Fer04]. Furthermore the measurements suggest that the structure of the matrix is only lightly influenced by the C_2 concentration in the plasma.

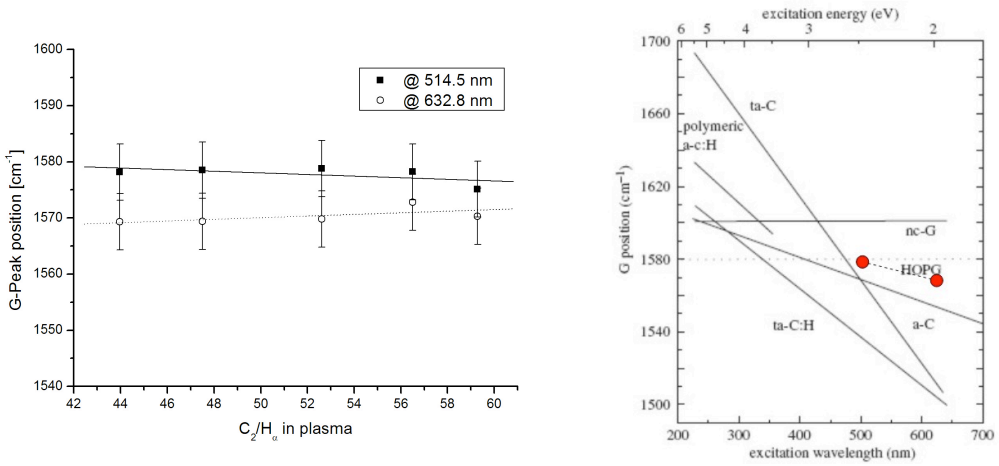

Figure 5.20 G-Peak dispersion as measured in UNCD films (left) and compared to other carbon films (right) [Fer04]. Dashed line in right picture indicate the measured G-Peaks for the UNCD samples at 514.5 nm and 632.8 nm respectively deposited at a C_2/H_α ratio of 58.5

Besides the typical peaks of amorphous carbon (D and G peaks at approximately 1350 and 1580 cm^{-1} respectively) the Raman spectra of ultra-nanocrystalline diamond features additional peaks at approximately 1150 and 1480 cm^{-1}, assigned to trans-polyacetylene in the matrix according to the literature [Fer00b] [Pfe05]. These features were investigated to determine their relationship with the intrinsic tensile stress in the films.

5.2.1.6 Influence of C_2 on Film Structure and Stress

Stress measurements were performed with a SSIOD ("**S**urface **S**tress **I**nduced **O**ptical **D**eflection") setup. By measuring the deflection angle of a laser beam incident on a substrate, the curvature of the substrate can be measured. Using Stoney's equation one can calculate the residual stress in the film σ with respect to the substrate properties (elastic modulus E_{sub} of the substrate, Poisson ratio v of the substrate, substrate thickness t_{sub}) and to the film thickness t_{film}. Because the residual stress is calculated from the change in substrate curvature induced by the deposited film a pre deposition measurement R_{pre} and a post deposition measurement R_{post} of the substrate curvature are necessary [Sto09].

$$\sigma = \frac{E_{sub}}{(1-\nu)} \frac{t_{sub}^2}{6 \cdot t_{film}} \left(\frac{1}{R_{post}} - \frac{1}{R_{pre}} \right) \qquad \text{Equation 5.10}$$

For thick films, the film bending moment and the resultant flexure stress are no longer negligible, and the film/substrate structure must be treated as a composite beam, which Windischmann and Gray considered for diamond films [Win95].
Because the thickness of most of the films investigated in this work is larger than 20 µm, the Brenner-Senderoff equation must be used to avoid substantial errors in the calculated stress,

$$S = S_0 \left(1 + 4R \frac{t_{film}}{t_{sub}} - \frac{t_{film}}{t_{sub}} \right) \qquad \text{Equation 5.11}$$

where R is the ratio between the film and substrate biaxial moduli (6.08 for polycrystalline diamond on (100) silicon) and S_0 is the stress derived from the Stoney equation.

It was found that the residual stress could be controlled directly by the carbon dimer density in the plasma (Figure 5.21) for C_2/H_α values lower than 55. For low values of C_2/H_α (≈ 42) the deposited films are under compressive stress (ca. -50 MPa). With increasing C_2/H_α the residual stress is changing into tensile stress to reach a maximum around a C_2/H_α value of 52. The maximum of tensile stress in the films was measured with 300 MPa. At higher dimer concentrations the deposited films get more and more graphitic and the residual stress is decreasing back to zero (at a C_2/H_α value of 57). At these high C_2/H_α values the C_2 density in the plasma is no longer directly determining the residual stress in the deposited films and the stress cannot be controlled by the C_2/H_α measurements anymore.
These results are remarkable because it is not only possible to monitor the residual stress in the deposited UNCD films by OES already during deposition but it is also possible to change the residual stress from tensile to compressive. This gives the possibility to tailor the residual stress in UNCD films for specific applications.
Of specific interest are the films deposited at values of 43 for the C_2/H_α because the measurements made in this work suggest that the films deposited at these conditions

are stress free, although it should be mentioned that these values vary with substrate temperature and substrate material.

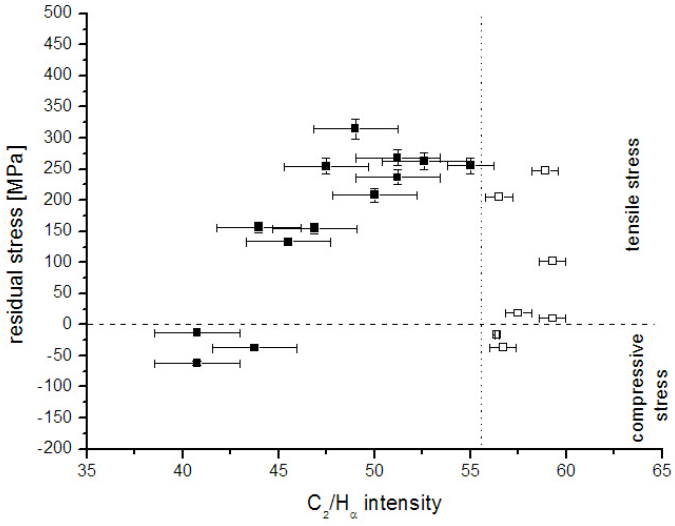

Figure 5.21 Influence of C_2/H_α – measured by Optical Emission Spectroscopy – on the residual stress in the films

The residual stress consists of two components: the thermal stress due to the different thermal expansion coefficients of the substrate and the film, and the intrinsic stress. By calculating the thermal stress, one can determine the intrinsic stress by subtracting the calculated thermal stress from the measured residual stress [Win91] [Fan00] [Woe06a]. The elastic modulus needed for the calculation was measured by nanoindentation as shown in Chapter 3.4.2.5.2.

The bending of a substrate induced by thermal stress can be calculated relatively simply with respect to Equation 5.12.

In Figure 5.22 the temperature dependence of the thermal expansion coefficients of silicon and diamond are shown. The thermal component of the residual stress can now be calculated by taking the integral of the coefficient of thermal expansion over the temperature and one gets the curvature of the sample that is induced by the thermal stress [Fan00] according to Equation 5.12.

$$\frac{1}{R} = \frac{6(1+m)^2 \int_{T_r}^{T_d} (\alpha_s - \alpha_f)\,dt}{h\left[3(1+m)^2 + (1+mn)\left(m^2 + \frac{1}{mn}\right)\right]} \qquad \text{Equation 5.12}$$

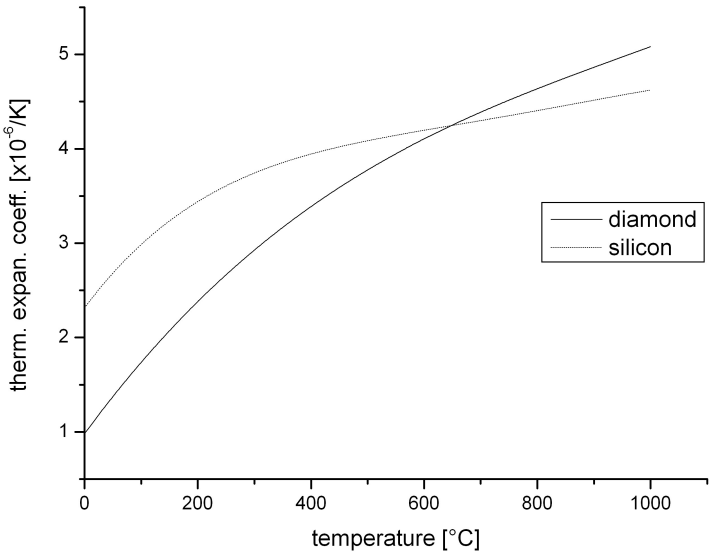

Figure 5.22 Thermal expansion coefficient of diamond and silicon

Taking the calculated thermal stress and subtracting it from the measured residual stress gives the intrinsic stress in the deposited films shown in Figure 5.23.

The thermal stress is calculated to be compressive, thus the residual stress in the UNCD films consists of a compressive thermal component and an intrinsic component that is tensile for all the deposited films.

Just like the residual stress the intrinsic stress is increasing with increasing C_2 dimer density in the plasma to reach a maximum at a C_2/H_α ratio of 52 with an intrinsic stress of 600 MPa. The intrinsic stress is decreasing again for higher C_2/H_α ratios.

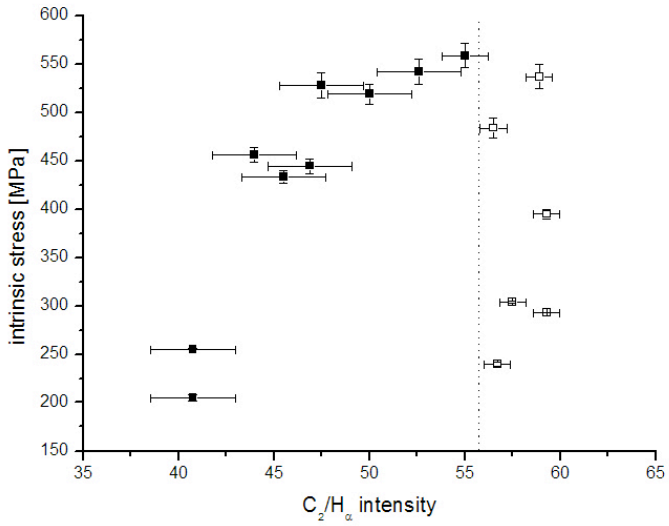

Figure 5.23 Intrinsic stress as a function of C_2/H_α

Figure 5.24 shows the positions of the <111> and <220> peaks as measured by XRD. A dashed line is added to each figure to indicate the position of each peak in the case of stress-free diamond crystals. In fact, both peaks are shifted to higher angles, indicating compressive stress in the grains. Moreover, the compressive stress in the grains seems to be independent of the C_2/H_α intensities and thus of the measured intrinsic stress in the films. This result suggests that the origin of the tensile stress cannot be found in the diamond grains themselves but in the surrounding matrix.

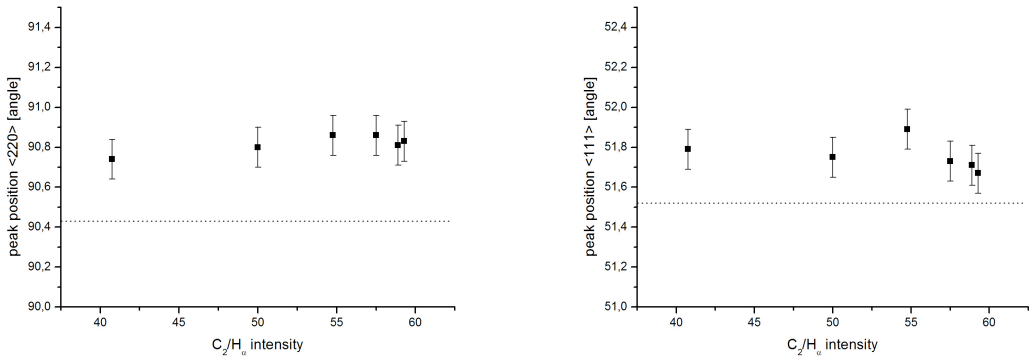

Figure 5.24 Peak position for the <111> and the <220> peak in the XRD pattern as a function of the C_2/H_α intensities. Dashed lines indicating position for stress free films

The relative intensity of the 1480 cm^{-1} Raman peak is investigated as follows. To exclude the external influences of experimental interference such as the variation of laser power, normalization to another spectral feature is proposed. Even if there is no such inherently constant feature normalization by the G peak is proposed to obtain a more robust quantitative verification of the intensity of the trans-polyacetylene peak.
Figure 5.25 shows the relative intensity of the peak at approximately 1480 cm^{-1}, which is usually assigned to trans-polyacetylene in the matrix, as a function of the intrinsic tensile stress.

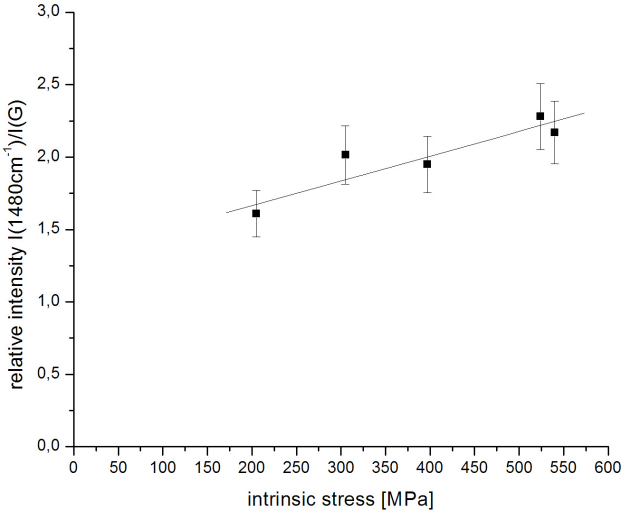

Figure 5.25 Relative intensities of the 1480 cm^{-1} peak as a function of the intrinsic tensile stress

It indeed turns out that the intensity of the trans-polyacetylene peak has a linear relationship with the intrinsic tensile stress in the film. The intensity is 50 % higher for a tensile stress of 600 MPa compared with a tensile stress at 200 MPa.

The results of investigating the trans-polyacetylene peak in the Raman spectra supports the results obtained by FTIR spectroscopy. Although the overall matrix volume is decreased at higher intrinsic stress, the intensities of the trans-polyacetylene peaks are increased. This can only be explained by a structural change in the matrix.

5.2.1.7 Plasma Parameters and Film Structure: C_2 Variation

The experimental results found in this chapter suggest that the C_2/H_α ratio in the plasma correlates with the inner structure of the NDC films. Although continuing experiments (with more variable process parameters) should be performed in the future to support the findings it is suggested that by controlling the C_2/H_α ratio it is possible to adjust the nucleation density and the growth rate of the deposited films. Higher C_2/H_α values lead to higher nucleation density and lower growth rate, suggesting that the C_2 is participating in the nucleation process of nanocrystalline diamond.

The orientation of the nanocrystals is influenced by the C_2/H_α ratio in the plasma from statistical orientation for low C_2/H_α values and a preferred <220> orientation for higher C_2/H_α values.

Although it was shown that the overall ratio of the matrix and crystals in the films could be influenced by the C_2/H_α variation between 30 and 40 %, the microscopic structure of the matrix is not changed.

Investigation of the matrix structure by Raman spectroscopy showed that the C-C bonds in the matrix are mainly sp^2-bonded with a sp^3 C-C fraction of below 5 % and a dispersion comparable to that of a-C films.

FTIR measurements showed that the C-H bonds in the matrix are mainly sp^3-bonded (85 %). The overall hydrogen content of the films is relativly low with 3 % measured by NRA.

It was shown that by adjusting the nucleation density one can tailor the matrix fraction of the films. As predicted by the grain boundaries model [Hof76] the matrix will lead to tensile stress in the films. This tensile stress was measured in all deposited films. The C_2/H_α was shown to be a very sensitive parameter to adjust the stress in the films and tailor it to the specific needs.

Furthermore it was shown that by extensive investigation of film structure a nondestructive spectroscopic method for the determination of mechanical stress was derived that may be important for technical applications. The applicability of this method is shown in Chapter 5.4.1 in more detail.

5.2.2 Influence of Hydrogen Admixture on the UNCD Properties

After investigating the influence of the C_2 density on the UNCD film growth, a set of experiments has been carried out to ascertain the role of hydrogen admixtures in the process gas on the deposition of these films. Nanocrystalline films were deposited at a pressure of 200 mbar from an Ar/CH_4 plasma with 0.8 % methane in argon. The percentage of hydrogen admixture in the process gas was varied between 2 % and 7 %.

The MW-power was kept constant at 1 kW and the films were deposited for 5 h on silicon substrates with substrate temperature of 720±20°C.

5.2.2.1 Influence of Hydrogen Admixture on Morphology and Growth Rate

The deposited films were investigated with SEM as shown in Figure 5.26. It is clearly seen that the structure of the UNCD films is changing with the amount of hydrogen in the process gas. The surface is rougher for higher hydrogen admixture and also the diamond crystals appear to become larger. The influence of hydrogen on the grain size during UNCD deposition was described before by Birrell et al. [Bir05].

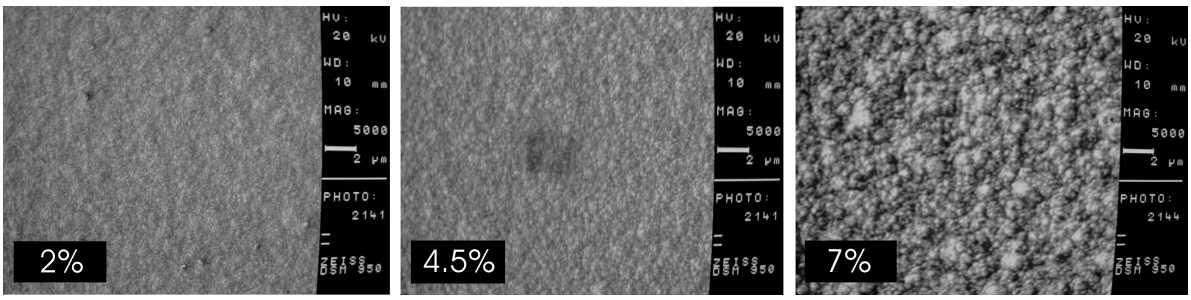

Figure 5.26 Morphology of UNC films deposited with different hydrogen fractions

Cross sections of the films were taken to investigate the film thickness and by that the deposition rate. Figure 5.27 shows the results for these measurements for two sets of experiments. The films in Series 1 were deposited with parameters given before while the substrate temperature for series 2 was increased to 800 ± 20°C and the methane fraction increased to 1 %. It is shown, that the deposition rate increases by increasing the amount of hydrogen in the process gas for both series of measurements as known from the literature.

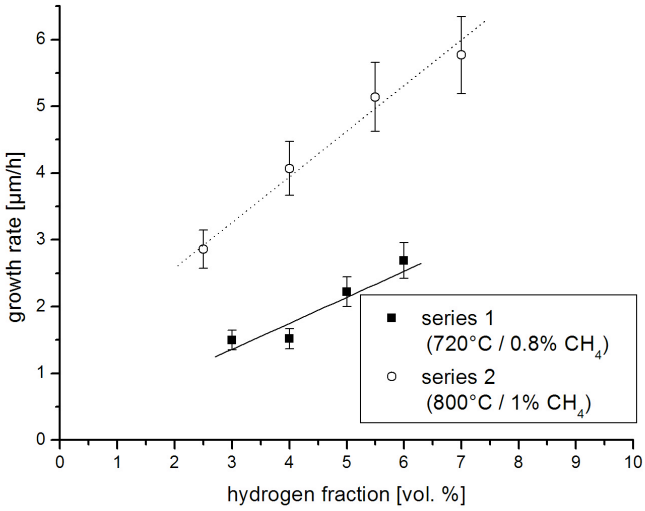

Figure 5.27 Growth rate dependence on hydrogen admixture

In Figure 5.28 it is shown that the reduction of grain size with less hydrogen in the process gas comes along with a smaller growth rate. It is shown that this effect is true for the whole temperature region investigated in this work. The growth rate is doubled when the hydrogen fraction is increased from 3 % to 6 %.

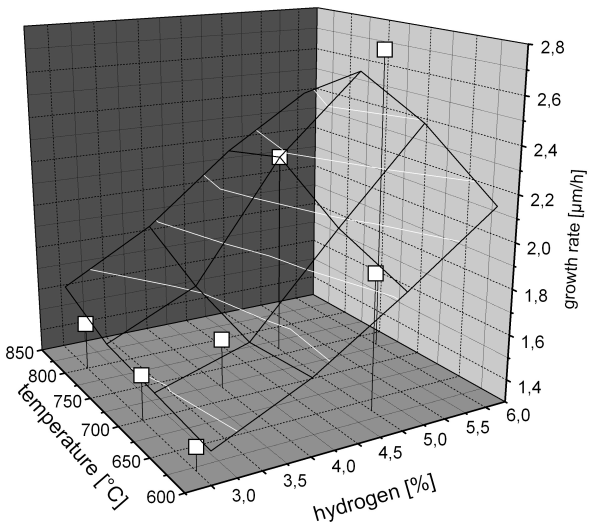

Figure 5.28 Growth rate as a function of hydrogen admixture and substrate temperature

Since the SEM measurements only give information about the surface roughness and not about the crystal size directly due to the nanometer size of the diamond

grains, grazing-incidence x-ray diffraction was used to investigate the crystalline structures of the samples. Again the d<111> at 51.52°, d<220> at 90.42°, and d<311> at 112.65° can be assigned in all spectra as allready shown in Figure 3.28. The intensities of these peaks are compared to reference powder samples to find a preferred orientation in the films.

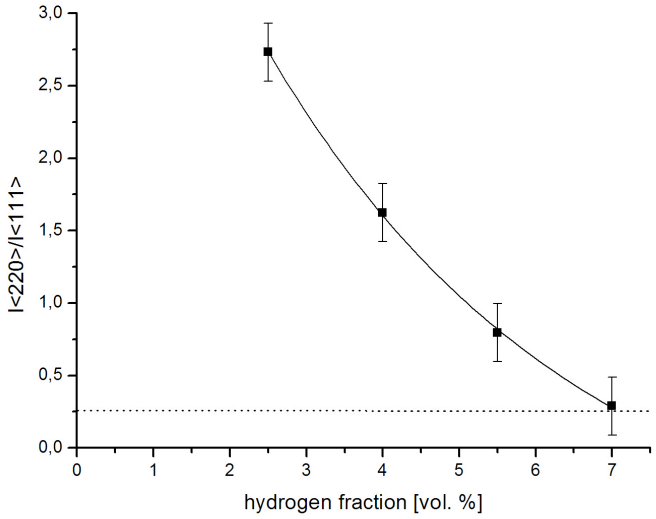

Figure 5.29 Intensity ratio of <220> and <111> peaks in XRD pattern. Dashed line indicating the literature value for randomly oriented diamond [Pow01]

Figure 5.29 shows the result and a comparison to the literature value for randomly oriented diamond samples (dashed line). The results are suggesting that the UNCD samples have a preferred <220> orientation for hydrogen depleted process gas compositions. Increasing the hydrogen admixture in the process gas leads to a more and more randomly oriented structure reaching the expected ratio for diamond of 0.25 for I<220>/I<111> above 7 % of hydrogen. These results stand in contrast to findings of Gerbi et al. [Ger05]. Although they found the same preferential <220> orientation in UNCD films their results suggest that increasing the hydrogen fraction in the process gas leads to a more pronounced <220> orientation in the films while introducing nitrogen to the process gas support a <111> oriented growth. They found UNCD films to grow randomly oriented with nitrogen admixtures of around 5 % with no hydrogen in the process gas. Figure 5.30 shows the I<111>/I<220> ratio obtained from our samples compared to the results of [Ger05].

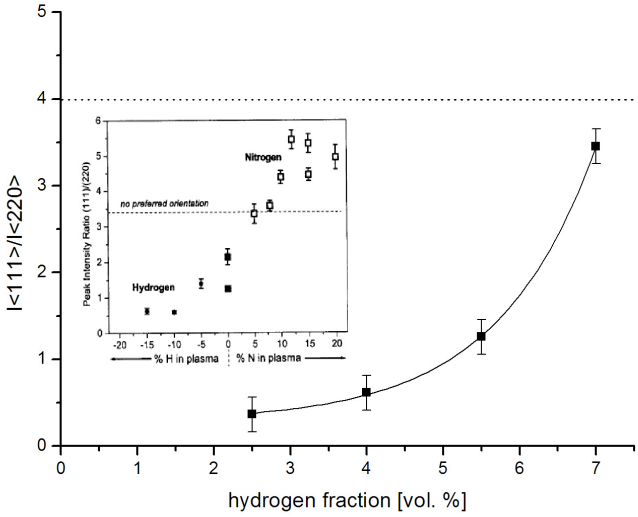

Figure 5.30 Intensity ratio of I<111>/I<220> in X-ray diffractogram. Dashed line indicating the literature value for randomly oriented diamond [Pow01]. Inset showing results from [Ger05]

The differences to our results (randomly oriented films at 7 % hydrogen admixture) may be due to other deposition conditions. Gerbi [Ger05] deposited films at rather low pressure of 150 mbar and at higher substrate temperatures of above 800°C. It was shown before that pressure as well as substrate temperature (demonstrated for microcrystalline diamond films by Koidl's work on the alpha Parameter of diamond growth [Wil93]) strongly influence the plasma properties and therefore the deposition mechanisms might be different making a direct comparison of the obtained results not possible.

5.2.2.2 Influence of Hydrogen Admixture on the Matrix Structure

Just like the samples from the C_2 density experiments the films deposited with different amounts of hydrogen in the process gas were investigated by FTIR and Raman spectroscopy to probe the internal structure of the matrix.

The FTIR spectra again show the strong absorption band between 2750 cm^{-1} and 3100 cm^{-1} indicating C:H stretching modes. It was possible to deconvolute the spectra using the 9 Gaussian peaks with frequencies and assignments found by Ristein [Ris98]. Figure 5.31 shows the total integrated absorption of the C:H stretching band as a function of the hydrogen admixture in the process gas. Error

bars of 20 % were added to include uncertainties in the baseline correction and in the fitting process.

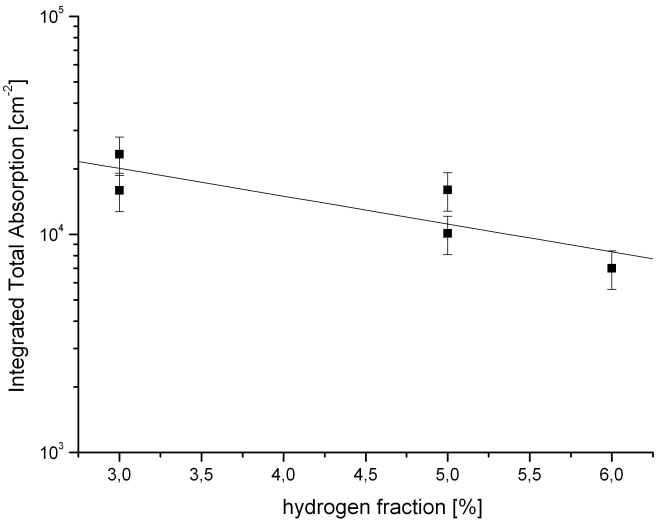

Figure 5.31 Total integrated absorption of C:H stretching modes as a function of hydrogen admixture in process gas

At first sight the result is contra-intuitive. The more hydrogen is added to the process gas the lower the integrated total adsorption by C-H bonds in the films. But this result can be explained when keeping in mind that adding of hydrogen leads to an increased grain size. The increased crystal size leads to a lower matrix fraction to the overall film volume and therefore the total absorption – resulting from C-H bonds in the matrix – is reduced.

By working out the FTIR relative absorption intensities for all sp^3CH_x and all sp^2CH_x stretching modes summed up respectively one can see the influence of hydrogen in the process gas on the C-H bonds. Figure 5.32 clearly shows that most C-H bonds in the films are sp^3-bonded (about 75 %). This fraction is even increased when more hydrogen is added to the process gas.

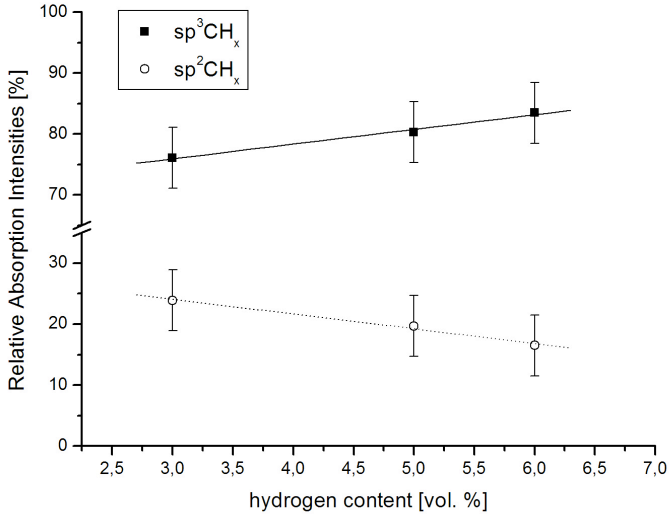

Figure 5.32 Influence of hydrogen on relative absorption intensities of all sp^3CH_x and all sp^2CH_x stretching modes

Figure 5.33 is indicating that hydrogen in the process gas is increasing the sp^3CH_2 and the sp^3CH_3-bonded hydrogen in particular while all sp^2-bonded hydrogen is decreased.

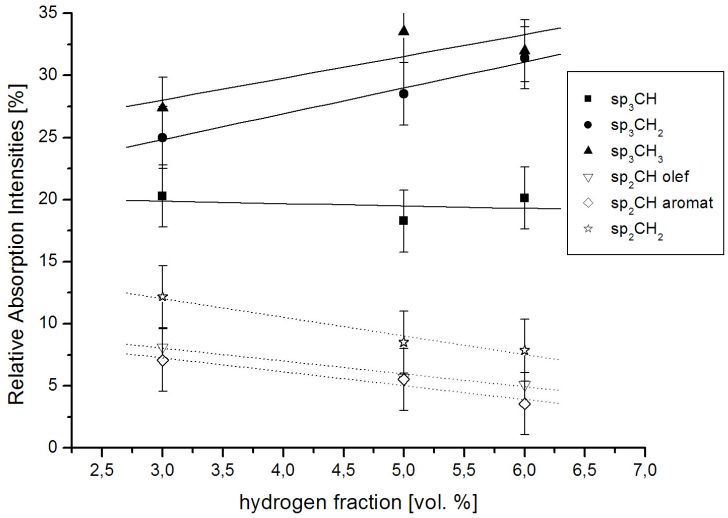

Figure 5.33 Influence of hydrogen on relative absorption intensities for all sp^3CH_x and all sp^2CH_x stretching modes

After characterizing the C:H bonds in the matrix, Raman spectroscopy is used to probe directly the C:C bonds in the films. The G-Peak positions of the deconvoluted

Raman spectra indicate the amount of sp^3-bonded carbon in the matrix (Figure 5.34). The G-Peak position is slightly shifted up to higher wavenumbers for higher hydrogen admixtures. A comparison of the results with the three-stage model of increased disorder [Fer00a] [Fer00b] (small inset in Figure 5.34) is suggesting that the matrix of the films deposited at low hydrogen admixtures consists of around 10 % sp^3-bonded carbon. The amount of sp^3-bonded carbon is decreasing for higher admixtures of hydrogen reaching 100 % sp^2-bonded carbon at around 7 % hydrogen fraction in the process gas.

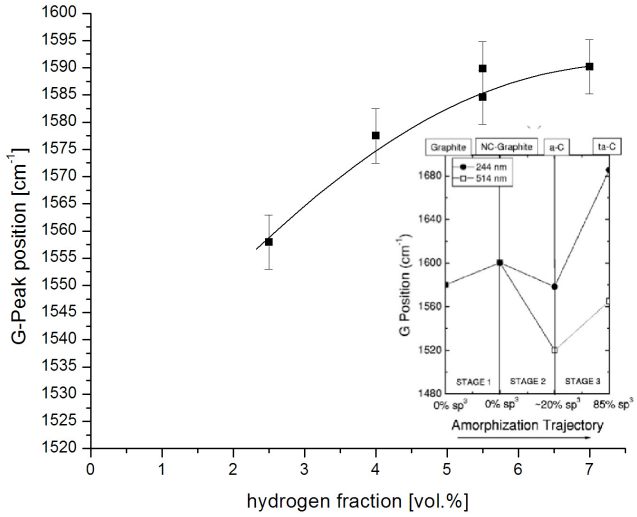

Figure 5.34 G-Peak position taken from Raman spectroscopy as a function of the hydrogen fraction in the process gas

The dispersion of the G-Peak was measured by taking Raman spectra with a second laser wavelength to get additionally information on the structure of the matrix. Figure 5.35 shows the G-Peak positions obtained with 514.5 nm and 632.8 nm excitation wavelengths respectively. The dispersion (difference between the G-Peak positions measured by the different wavelength) is not changing with increasing hydrogen fraction. Comparing the results to the data obtained in the C_2 density variation in Chapter 5.2.1 makes clear that the dispersion is lower for the films deposited with higher hydrogen fraction. While the matrix consisted of a-C in the earlier measurements the latter consist more of nanocrystalline graphitic structures.

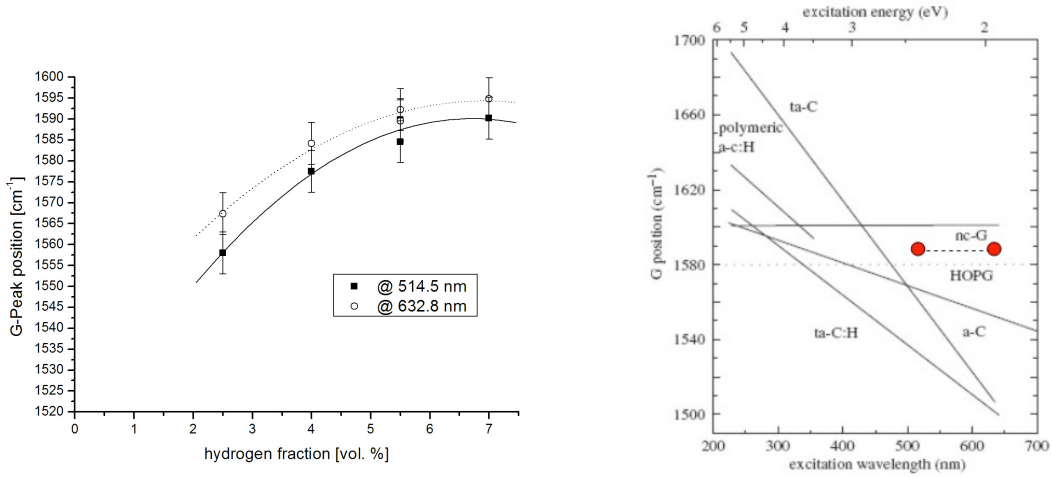

Figure 5.35 Dispersion of G-Peak as measured in UNCD films (left) and compared to other carbon films (right) [Fer04]. Dashed line in right picture indicate the measured G-Peaks for the UNCD samples at 514.5 nm and 632.8 nm respectively deposited with 7 % hydrogen

5.2.2.3 Influence of Hydrogen on Residual Stress

Results of this chapter were published in [Woe06c] and [Woe07].

Because it was demonstrated by the grain boundaries mismatch model how grain boundaries affect the residual stress (Chapter 3.2.3.1) and hydrogen is believed to increase the grain size in UNCD growth, a strong influence of the hydrogen in the plasma on the stress is expected.

Again because the film thickness investigated in this work is relatively large the Brenner-Senderoff equation must be used to correct the results of Stoney's equation to avoid substantial errors in the calculated stress [Bre49].

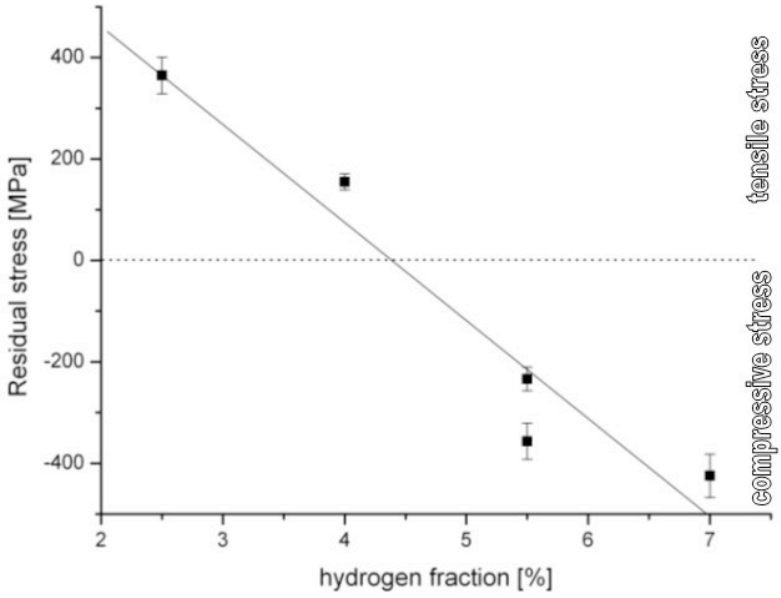

Figure 5.36 Residual Stress as a function of hydrogen fraction in the process gas

The residual stress is plotted versus the hydrogen fraction in the process gas. Both tensile and compressive stresses are measured. Per definition compressive stress is negative and tensile stress is positive.

It is shown that for small amounts of hydrogen, tensile stress is measured in the films. This changes as soon as the hydrogen fraction is increased above 4.5 %. Beyond this amount compressive stress is measured. This finding is of great interest, firstly because it is possible to adjust the residual stress in UNCD films in a wide range just by changing the amount of hydrogen in the process gas, and secondly because it is thereby possible to find process parameters where stress-free UNCD films can be deposited.

Again by subtracting the thermal stress from the measured residual stress one can deduce the intrinsic stress in the films as shown in Figure 5.37 for the UNCD films.

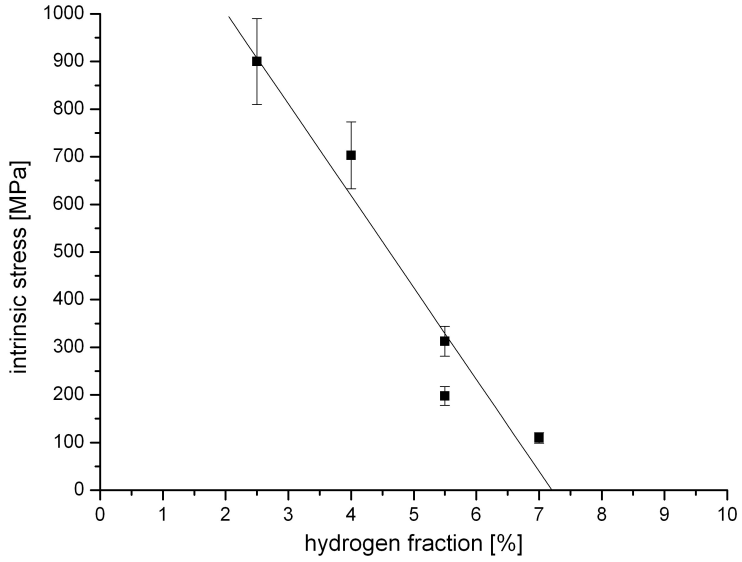

Figure 5.37 Intrinsic stress in the UNCD films

As shown before, the residual stress in the UNCD films consists of a compressive thermal component and an intrinsic component that is tensile for all the deposited films. The results suggest that the hydrogen admixture in the process gas can strongly influence the intrinsic tensile stress. For low amounts of hydrogen the tensile stress in the film is rather high at around 1000 MPa. By adding more hydrogen to the process gas the films are less tensile stressed. At a concentration of 7 % of hydrogen the tensile stress is as low as 100 MPa in the film.

As mentioned above the intrinsic stress usually is dominated by two contributions that can be explained by the two models: (1) The Ion Peening model that describes the bombardment of high energetic particles leading to overdense films and thus to compressive stress in the films (Chapter 3.2.3.2) and (2) the grain boundary mismatch model [Hof76] predicting tensile stress in underdense films. Because of the low mean free path at the given pressure of 200 mbar, strong thermalization of the particles must be assumed and thus ion peening can be neglected as in the case of microcrystalline diamond [Win91].

Extending this model to 3d-nanostructured materials like UNCD – here diamond grains in an amorphous matrix – one can look at grain boundaries as amorphous material; but in UNCD the thickness or amount of this amorphous matrix can be systematically varied. Adding hydrogen to the process gas leads to larger diamond crystals in the film [Bir05] and therefore the amount of matrix (former grain boundaries density) is decreased as can be explained by a simple model: A given

film volume is filled with idealized cubic crystals of equal edge length *a*. The volume of the film V_f is than filled with *N* crystals of the volume a^3.

$$V_f = N \cdot a^3 \Rightarrow N = \frac{V_f}{a^3} \qquad \text{Equation 5.13}$$

The six sides of the crystal cubes in this model and the area of one side given by a^2 give the surface area of the crystals. Because every crystal is directly neighboured by another crystal every sidewall is the sidewall of two crystals, the overall surface area A_f is therefore given by:

$$A_f = 3 \cdot N \cdot a^2 \qquad \text{Equation 5.14}$$

Using Equation 5.13 and Equation 5.14 one can eliminate the actual number of crystals and calculate the surface area by:

$$A_f = 3 \cdot V_f \cdot \frac{1}{a} \qquad \text{Equation 5.15}$$

Using the thickness of the grain boundaries *d* one can now calculate the overall volume of the matrix by

$$V_g = d \cdot A_f = 3 \cdot V_f \cdot \frac{d}{a} \qquad \text{Equation 5.16}$$

Anyway even for more realistic shapes there will be

$$\frac{V_g}{V_f} \sim \frac{d}{a} \qquad \text{Equation 5.17}$$

With the assumption that the thickness of the grain boundaries is not significantly changing one can see that the volume of the matrix normalized to the volume of the film is inversely proportional to the grain size. Further, the density of the grain size is, due to its disordered structure, lower than the density of the diamond crystals and

therefore the expression V_g/V_f equals the density change in the film. The relation between intrinsic stress, density and the grain size in this case is thus given with respect to Equation 5.17 by

$$\frac{\Delta\rho}{\rho} \sim \frac{V_g}{V_f} \sim \sigma \sim \frac{1}{a} \qquad \text{Equation 5.18}$$

By reducing the hydrogen in the process gas one is decreasing the grain size, thus increasing the amount of grain boundaries and according to Equation 5.18 the tensile stress is higher as experimentaly shown in Figure 5.37.
The relation given by Equation 5.18 between the grain size and the tensile stress in films is consistent with the model given by Hoffmann [Hof76] but extends the applicability to nanostructures where grains with different shapes (e.g needles) occur or structural variations of the matrix leads to different thicknesses of the “grain boundaries”. Thus it should be mentioned that it is not a microscopic contradiction to this model, but obviously included that at constant grain diameter the mechanical stress can be changed by variation of the “thickness of the grain boundaries”.

The decreased matrix fraction with increased hydrogen fraction was already shown by measuring the hydrogen dependence of the integrated total absorption of the C-H band obtained from FTIR spectra (Figure 5.31). The contra-intuitive behaviour was measured that adding more hydrogen to the process gas decreases the total absorption of C-H bonds in the films. This behaviour can be explained by taking into account that the grains in the films get bigger with more hydrogen added to the process gas and therefore the grain boundary density is reduced. The correlation between the intrinsic stress and the integrated total absorption is shown in Figure 5.38.

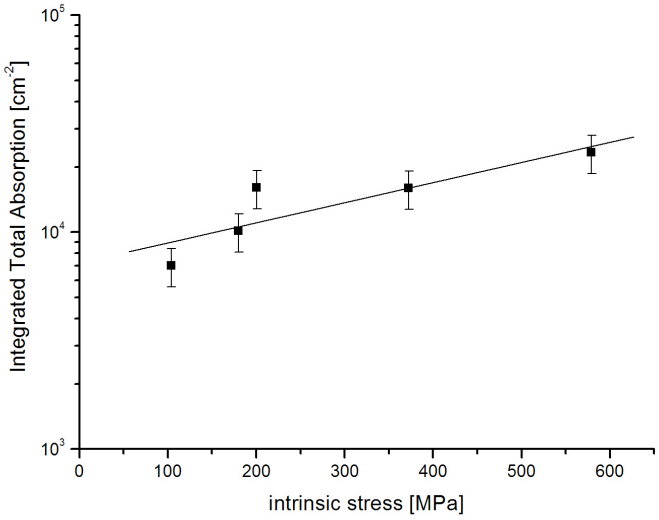

Figure 5.38 Integrated Total Absorption of the C:H band obtained from FTIR spectra as a function of the intrinsic stress

5.2.2.4 Influence of Hydrogen on Elastic Modulus

Nanoindentation measured the influence of the hydrogen admixture. The measurements are shown in Figure 5.39. It is shown that the hydrogen admixture influences the values for the elastic modulus during deposition. As expected the elastic modulus is higher (the material is stiffer) for higher admixtures of hydrogen. This can be explained by the larger diamond crystals in the amorphous matrix and the fact that the elastic modulus of the amorphous matrix is significantly lower than the modulus of the diamond grains. While the elastic modulus for diamond is around 1220 GPa the elastic modulus of the deposited UNCD films is measured to be around 500 GPa.

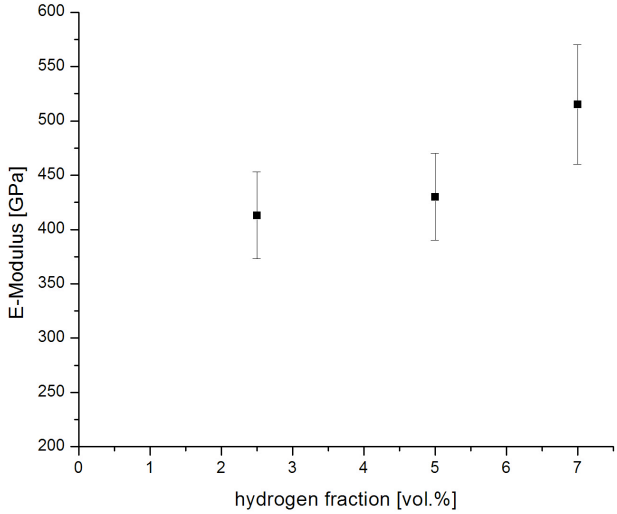

Figure 5.39 Influence of hydrogen on the E-Modulus of the film

5.2.2.5 Plasma Parameters and Film Structure: Hydrogen Variation

UNCD films were deposited using different hydrogen admixtures. It was investigated how the hydrogen is influencing the growth of the diamond films. It was shown that the growth rate is increased with the amount of hydrogen in the process gas and that the dimond crystals in the matrix become larger.

In contrast to the C_2 variation experiments shown in Chapter 5.2.1 hydrogen does influence the matrix structure.

The C-H bonds in the matrix are mainly sp^3-bonded as measured by FTIR and the concentration could be varied between 75 % for low hydrogen admixtures and 85 % for higher admixtures.

The hydrogen admixture is also influencing the C-C bonds in the matrix. Raman measured 10 % sp^3-bonded C-C for low admixtures of hydrogen and a nearly complete sp^2 C-C bonded matrix for high hydrogen admixtures. Raman dispersion was very low and comparable to nc-C.

The residual stress in UNCD films was measured and it was shown that it consists of a thermal component arising from the different thermal expansion coefficients of film and substrate and an intrinsic stress. The thermal stress was calculated and was found to be compressive for nanocrystalline films on silicon substrates. The intrinsic stress in the films was determined by substracting the calculated thermal stress from

the measured residual stress. It was shown that the intrinsic stress in the films is tensile for the UNCD presented in this work.

By altering the amount of hydrogen in the process gas it was shown that the intrinsic tensile stress in the films could be adjusted in a wide range. An explanation for the influence of hydrogen on the intrinsic tensile stress was given based on an extended grain boundaries mismatch model. It is known from the literature that a higher concentration of hydrogen in the process gas leads to larger crystals in the deposited film. Larger crystals mean less matrix fraction (lower grain boundaries density) and therefore lower intrinsic tensile stress.

Thus specific tailoring of the intrinsic tensile stress to compensate the compressive thermal stress seems possible and is an interesting possibility prospect for stress free films on substrates.

The influence of the hydrogen on the crystal size has also affect other film properties, as shown for the elastic modulus and the hardness. The fact that diamond grains are embedded in a carbon matrix with different properties allows tailoring the overall film properties in a wide range.

5.2.3 Influence of Nitrogen Admixture on UNCD Properties

An especially appealing field of application for UNCD are nitrogen doped semiconducting films. UNCD films are usually insulating, but n-doping is easily possible by admixture of nitrogen to the process gas. [Gru04]

To investigate the influence of the nitrogen admixture in the plasma on the deposition process more films were deposited at a pressure of 200 mbar with admixtures of nitrogen of 0 % to 7.5 %.

5.2.3.1 Influence of Nitrogen on Growth Rate

Figure 5.40 shows the influence of the nitrogen on the growth rate of the UNCD films. It is shown that the growth rate is highest for relatively small admixtures of nitrogen. With more Nitrogen in the deposition process the growth rate is decreased.

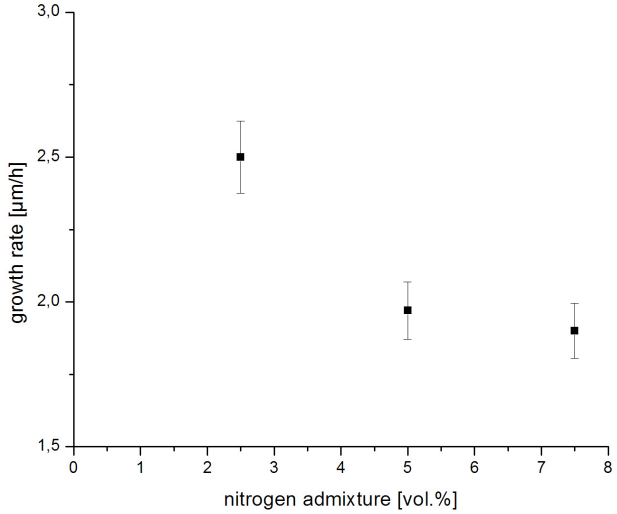

Figure 5.40 Influence of nitrogen admixture on growth rate

5.2.3.2 Influence of Nitrogen on Film Structure

High-resolution SEM pictures were taken to investigate the influence of hydrogen and nitrogen admixture on the morphology of the films. Figure 5.41 shows a film deposited with 2.5 % hydrogen and 2.5 % nitrogen in the plasma. The diamond grains appear to be very fine. Increasing the hydrogen admixture to 5 % while keeping the amount of nitrogen constant leads to bigger crystals as shown in Figure 5.42. Increasing the nitrogen admixture to 7.5 % and keeping the hydrogen admixture at 2.5 % changes the shape of the diamond grains. They appear to be needle-shaped as shown in Figure 5.43. These measurements show that the size of the grains is mainly influenced by the hydrogen fraction in the plasma and the nitrogen admixture can influence the shape of the diamond grains.

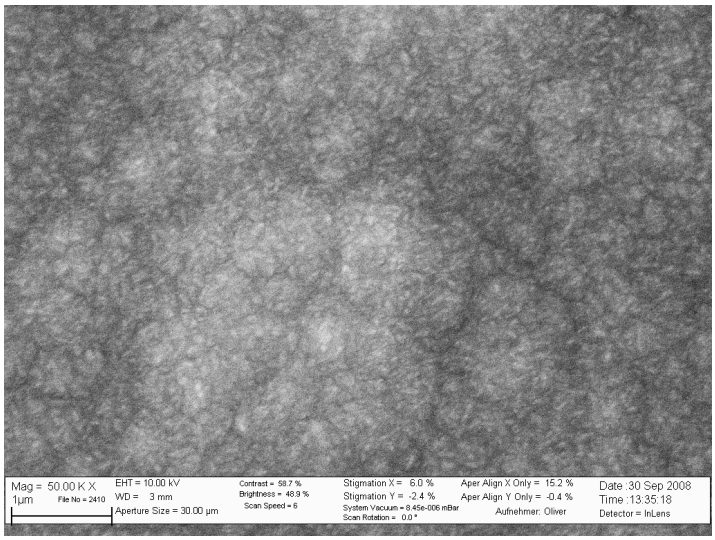

Figure 5.41 High resolution SEM measurement of a UNCD film deposited with 2.5 % hydrogen and 2.5 % nitrogen admixture

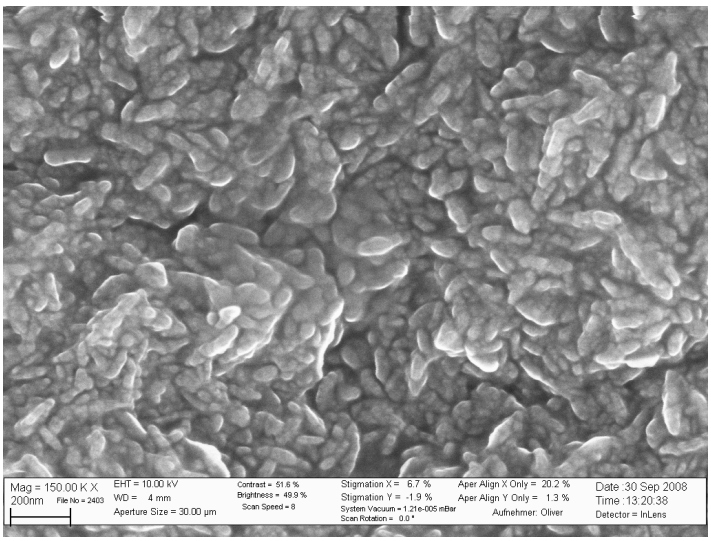

Figure 5.42 High resolution SEM measurement of a UNCD film deposited with 5 % hydrogen and 2.5 % nitrogen admixture

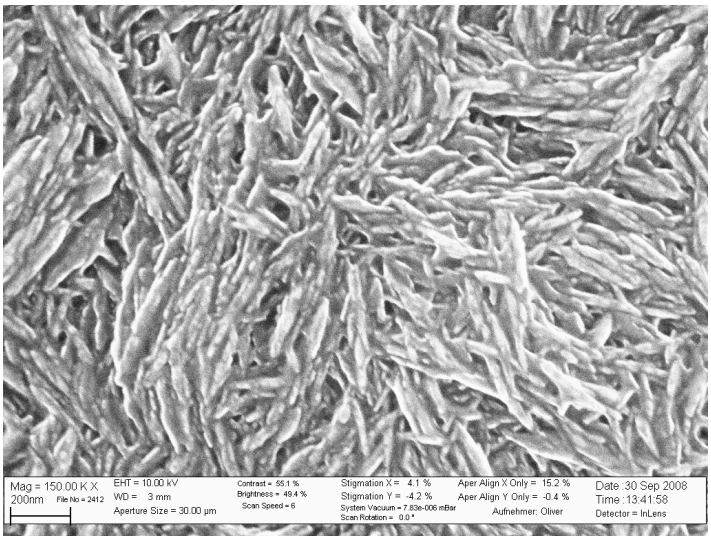

Figure 5.43 High resolution SEM measurement of a UNCD film deposited with 2.5 % hydrogen and 7.5 % nitrogen admixture

5.2.3.3 Influence of Nitrogen on Mechanical Properties

The influence of the nitrogen admixture on the elastic modulus and the hardness of the deposited films were measured by nanoindentation. The elastic modulus measurements are shown in Figure 5.44.

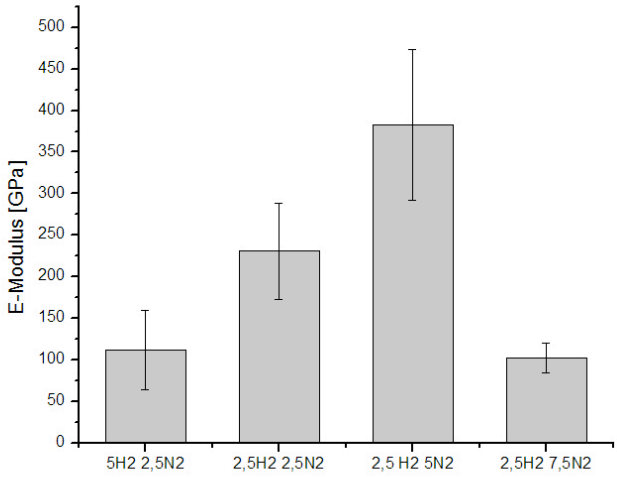

Figure 5.44 Influence of nitrogen and hydrogen on the E-Modulus of the films

It is shown that the nitrogen admixture influences the values for the elastic modulus during deposition. The films that were deposited with additional nitrogen are less stiff compared to the results shown in Chapter 5.2.2.4 where no additional nitrogen was used. While the elastic modulus for diamond is around 1220 GPa the elastic modulus

of the deposited UNCD films without additional nitrogen in the plasma was measured to be around 500 GPa. Now, by adding nitrogen, the elastic modulus for the deposited films was varied in a wide range from around 400 GPa down to 100 GPa.

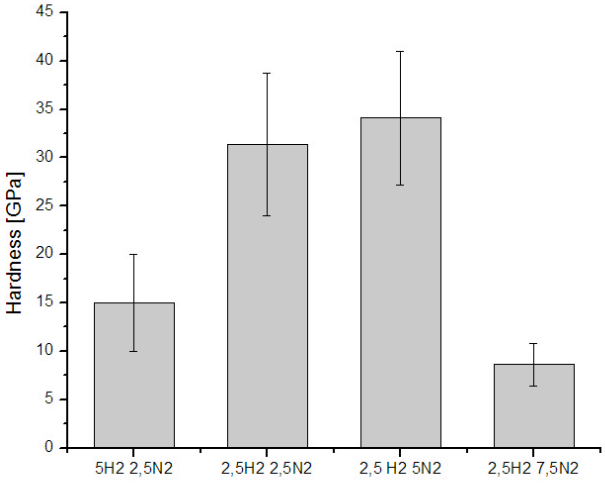

Figure 5.45 Influence of nitrogen and hydrogen on the hardness of the films

Additionally the hardness of the deposited films was measured (Figure 5.45). It is shown that the hardness can be varied considerably by a factor of three with respect to the process gas mixture used. Compared to single crystal diamond with a hardness of 100 GPa the hardness of the deposited films was measured to be between 10 GPa and 35 GPa only.

5.2.3.4 Results of Nitrogen Variation

The influence of nitrogen on the CVD diamond deposition is a wide subject and can only be briefly discussed in the course of this work.

The role of the produced C_xN_y species in the growth process is not fully understood and only some results are presented here.

It was shown how the Nitrogen admixture is influencing the growth rate and the structure of the UNCD films. While the hydrogen admixture is mainly influencing the crystal size, the Nitrogen admixture is changing the shape of the crystals to needle shaped crystals for higher nitrogen admixtures.

Additionaly Elastic modulus and hardness measurements were done by nanoindentation showing the influence of the nitrogen on the mechanical properties of the deposited films.

5.3 Influence of Substrate Properties on Film Properties

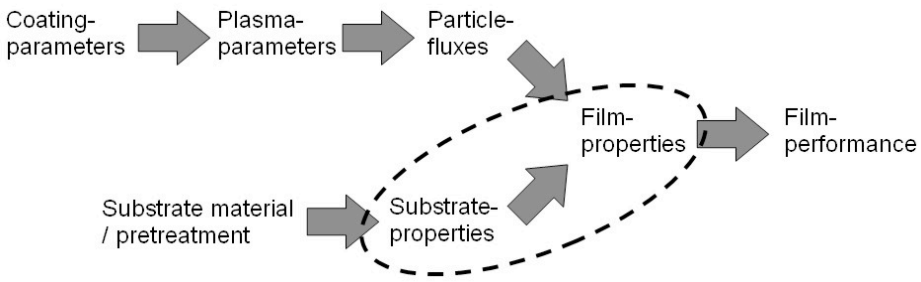

Figure 5.46 Influence of substrate properties on the film properties

Just like the particle fluxes and the plasma parameters are affecting the growing film, the film properties are influenced by the substrate properties (Figure 5.46). The growth influencing substrate properties can be classified into three categories: Firstly the material of the substrate, next the substrate pre-treatment, and finally the substrate temperature during film growth.

In many cases the substrate material is predetermined by the later application and is thereby not available for controlling the deposition process. Nevertheless the material does influence deposition steps like nucleation and growth and needs to be considered when modelling the deposition. All UNCD films shown in this work were deposited on silicon wafer. Although coatings were produced for SiC pump seals and WC–6%Co hardmetal substrates during the time of the work to demonstrate the technological applicability of the films, these results are not element of this thesis.

A variety of publications were dealing with the investigation of pre-treatment steps to increase the nucleation density of diamond on substrates. Especially the bias enhanced nucleation (BEN) (i.e. the application of a bias voltage to the substrate) and the mechanically scratching of the substrate surface are popular methods for the deposition of diamond films. More recent publications dealing with the substrate pre-treatment for UNCD deposition are [Lee06] [Che07]. They investigated four different pre-nucleation techniques for depositing UNCD films at low energies: bias- enhanced nucleation (BEN); pre-carburized and then ultrasonication with diamond powder

solution; ultrasonication with diamond and Ti mixed powder solution; and ultrasonication with diamond powder solution.

In this work the ultrasonication with diamond and Ti mixture powder solution was adopted because this method offers a high and homogeneous nucleation density even on large areas with a high reproducibility of the process. The pre-treatment process was not changed during the experiments in this work although different pre-treatment methods and their influence on the adhesion of the films were conducted in cooperation with the group of Prof. Deuerler (University of Wuppertal) in the process of coating WC–6%Co hardmetal substrates. The substrate surface was always modified by diamond grinding, sandblasting and/or etching. Additionally, different methods of mechanical pre-treatment like ultrasonically induced cavitation or shot peening with Al_2O_3 and SiO_2 particles were used to optimise the adhesion between diamond coating and cemented carbide cutting tool inserts. The results of this research were published in [Deu06].

The substrate temperature is a major process parameter that is predetermining the resulting film properties. Hence great effort was made to integrate a new aerosol water cooling specially designed for the needs of diamond CVD deposition to the experimental setup to allow the control and adjustment of the substrate temperature.

Monitoring and controlling the substrate temperature is in particular desirable because other process parameters like pressure, MW-Power and gas composition influence the temperature. If one wants to investigate the influence of the substrate temperature on the film growth solely, the temperature adjustment needs to be decoupled from other process parameters like it was done with the aerosol cooling in this work.

5.3.1 Influence of Substrate Temperature on Growth Rate

The influence of the process parameters on the substrate temperature during deposition can be taken from Figure 5.47. The substrate temperature was measured with deactivated aerosol substrate cooling in correlation to the MW-Power and the pressure. It is shown that the MW-Power has only limited influence on the substrate temperature while the influence of the pressure is more significant. The reason for the pressure influence on the temperature is the higher heat transfer from the plasma to the substrate holder at higher pressure due to more collisions. The MW-power is

mainly influencing the plasma ball size, thus enlarging the heated substrate area with limited effect on the substrate temperture.

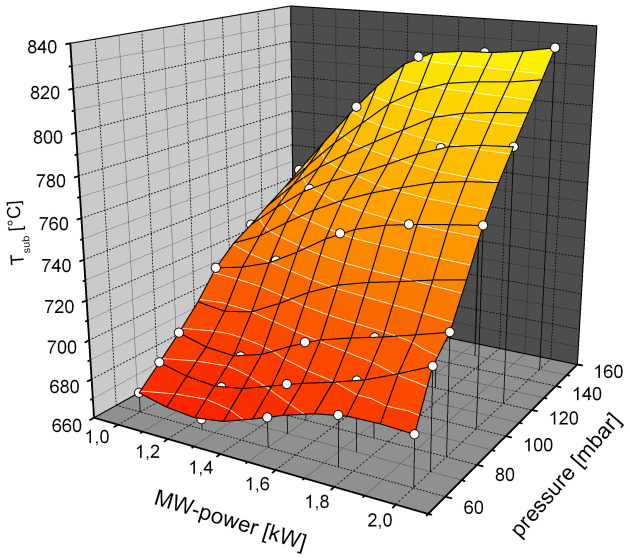

Figure 5.47 Influence of process parameters on substrate temperature (deactivated aerosol water cooling)

By variation of cooling power and otherwise constant process parameters UNCD films were deposited at different substrate temperatures. As shown in Figure 5.48 the influence of the substrate temperature on the growth rate was investigated in two sets of experiments for 3 % hydrogen admixture and 5 % hydrogen admixture respectively. The growth rate was found to be around 1.5 µm/h for 3 % hydrogen and around 2 µm/h for 5 % hydrogen. For both process gas compositions the growth rate is increased for higher deposition temperatures. At the same time the influence of the substrate temperature on the growth rate is increased with higher hydrogen admixture as can be seen from the slope of the fitted lines in the diagram. This fact is also reflected by the empirically calculated activation energies for the experiments.

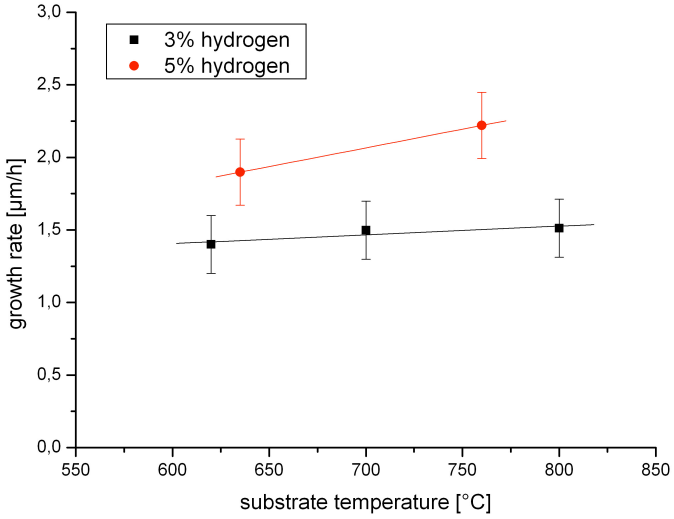

Figure 5.48 Influence of the substrate temperature on the growth rate

5.3.2 Influence of Temperature on Matrix Properties

The correlation of hydrogen admixture with growth rate and grain boundary density was shown in Chapter 5.2.2. Figure 5.49 shows the results again complemented by an additional axis showing the influence of the substrate temperature on the integrated total absorption measurements taken from the FTIR spectra. Since the absorption is mainly taking place in the matrix, the total adsorption is assumed to correlate with the matrix fraction. It is shown that the secondary nucleation (and therefore the grain boundaries density) is highest for low admixtures of hydrogen and low substrate temperatures. This result is in contrast to the results for the growth rate that is highest for higher temperatures and higher hydrogen admixtures. These results support the assumption that two independent processes are involved in the deposition of UNCD diamond: one process leading to secondary nucleation and one to the growth of the nuclei.

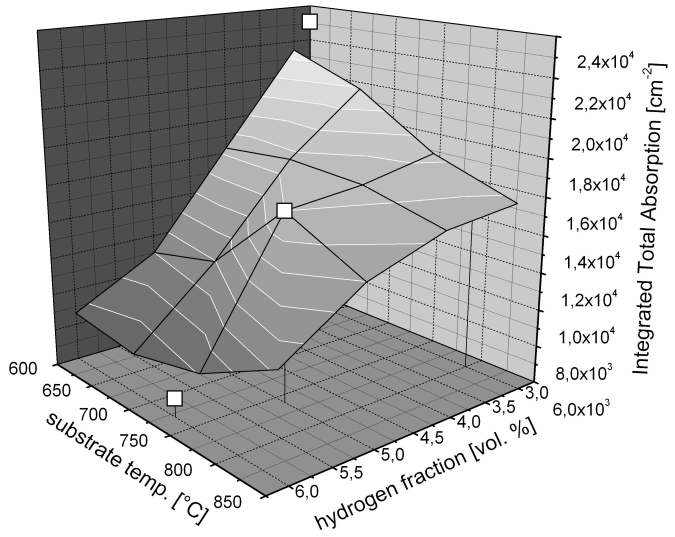

Figure 5.49 Integrated Total Adsorption as a function of substrate temperature and hydrogen fraction in process gas

The assumption of higher secondary nucleation and hence higher matrix fraction at lower temperatures is also supported by the intrinsic stress measurements shown in Figure 5.50.

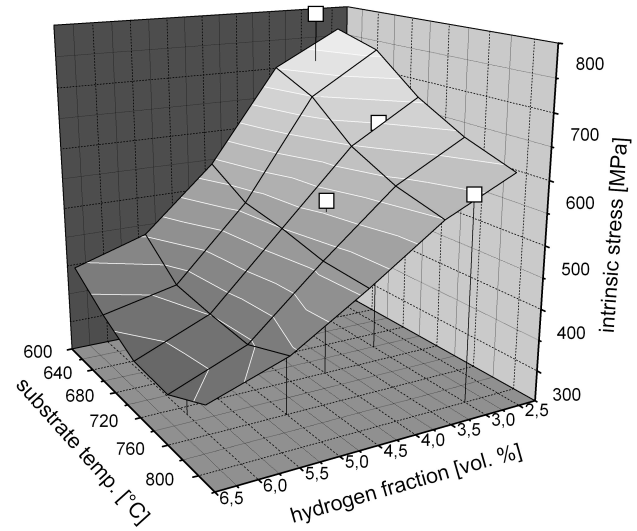

Figure 5.50 Intrinsic stress as a function of substrate temperature and hydrogen fraction in the process gas

The higher matrix fraction to the overall film volume for lower substrate temperatures results in higher intrinsic stress in the films as explained by the extended grain

boundaries mismatch model shown in Chapter 5.2.2.3. So the results from absorption measurements by FTIR spectroscopy and intrinsic stress measurements give a consistent picture of higher matrix fraction for lower substrate temperature and lower hydrogen fraction in the process gas.

Finally Raman and FTIR spectroscopy investigated the matrix structure of the films deposited at different substrate temperatures. Raman spectra for a film deposited at 525°C and 625°C respectively are shown in Figure 5.51. The values of the characteristic features of the deconvoluted spectra are shown in Table 5.2.

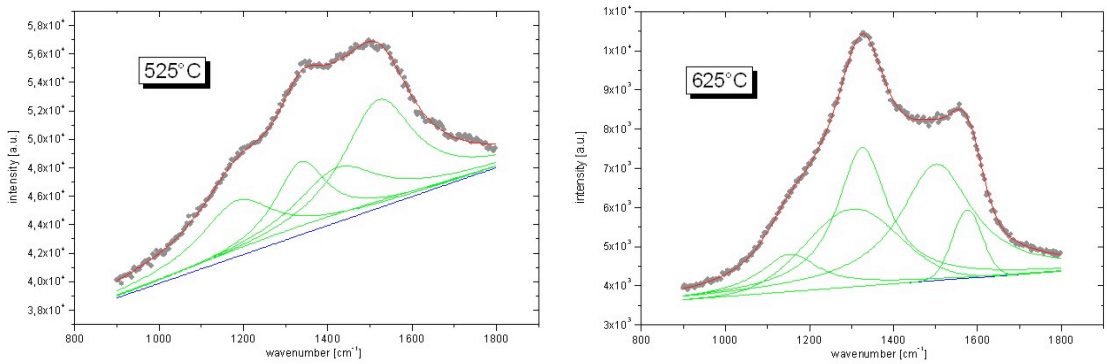

Figure 5.51 Raman spectra for UNCD films deposited at different deposition temperatures

Sample	Substrate Temperature [°C]	Intrinsic stress [MPa]	Growth rate [µm/h]	Position G-Peak [cm^{-1}]	FWHM(G) [cm^{-1}]	I(D)/I(G)
050215	720	292.92	3.34	1575.13	94.12	1.31
060315	630	52.08	2.03	1575.0	23.5	2.02
060316	525	802.53	0.36	1520.84	205.6	0.67

Table 5.2 Data taken from Raman spectra

Both the G-Peak position shift and the broadening of the FWHM of the G-Peak give hints that the sp^3 amount in the matrix is increased up to 10 % for lower substrate temperatures. Consistent with that is the ratio of the D-Peak to G-Peak intensities becoming smaller for lower substrate temperatures. A smaller I(D)/I(G) ratio represents more sp^2 chain structure bonds in the matrix in contrast to higher values which mean more sp^2 ring like structures.

Sample	Substrate Temperature [°C]	Intrinsic stress [MPa]	Growth rate [µm/h]	Total integrated absorption [cm^{-1}]	Sp^3/sp^2
061020	625	797.29	1.4	$2.33 \cdot 10^4$	7.28
061023	800	580.41	1.512	$1.59 \cdot 10^4$	3.18
061024	700	641.64	1.498	*$(9.07 \cdot 10^3)$*	3.65

Table 5.3 Data taken from IR spectroscopy

The FTIR spectra show the same trend for the sp^3 C-H bonds in the matrix (Table 5.3) (Figure 5.52). The lower the substrate temperature during the deposition the higher the sp^3/sp^2 ratio of the C-H bonded carbon in the matrix is.

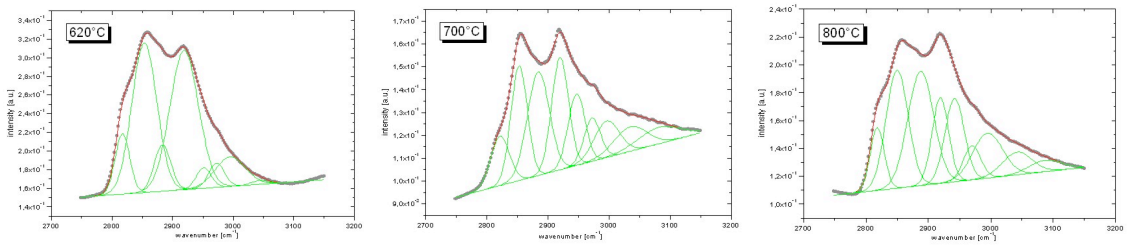

Figure 5.52 FTIR spectra of UNCD films deposited at different temperatures

5.3.3 Results of Substrate Temperature Variation

Due to the fact that the influence of substrate pretreatment and substrate material were studied in detail in previous publications [Lee06] [Che07], the influence of the substrate temperature was investigated in the course of this work.

It was shown that the substrate temperature has influence on the growth rate with higher growth rate for higher substrate temperature.

Spectroscopic and stress measurements support the assumption of (at least) one nucleation precursor and a growth precursor participating in the growth. Films with a higher matrix fraction in the samples were deposited at lower substrate temperature and lower hydrogen admixture (thus being deposited under C_2 favourable conditions with high secondary nucleation).

Finally it was shown that the substrate temperature has an influence on the matrix structure as measured by Raman and FTIR spectroscopy. Films deposited at lower

substrate temperature favour slightly increased sp^3 C-C bonds and also sp^3/sp^2 ratios of C-H bonds are increased.

5.4 Film Performance: Some Aspects for Technical Applications

Results of this chapter published in [Woe07].

In this chapter the intrinsic stress in the deposited films is investigated as a key property of the film. The reason why the residual stress is regarded as one of the most important film properties is not only because the stress state of the film determines the film adhesion and therefore the film performance but also because the measurement and interpretation of the residual stress in the films exceeds by far the simple determination of the stress state in the films.
For the first time a correlation between features in the spectroscopic Raman measurements and the intrinsic stress in UNCD films were found allowing a non-destructive way of measuring stress states in 3d objects. Furthermore it will be shown that stress measurements also give information about the thermal expansion coefficients in the deposited films. These methods were used for the first time on UNCD films to determine film properties in the course of this work.

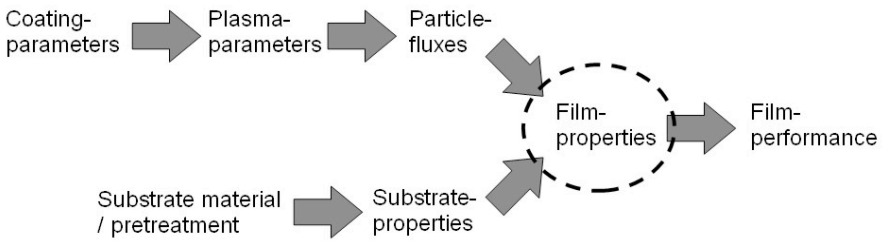

Figure 5.53 Film performance

5.4.1 Spectroscopic Stress Measurements in UNCD Films

It was shown that the intrinsic stress in the UNCD films correlates with the matrix volume fraction. As shown before, optical spectroscopic methods such as Raman and FTIR spectroscopy are basically probing the amorphous matrix of the films. It was tried to find features of the Raman spectra that correlate with the intrinsic stress.

Figure 5.54 shows the Raman spectrum (laser wavelength λ=632.8 nm) of a UNCD film deposited with 2.5 % hydrogen in the process gas. The spectrum was fitted as described earlier (Chapter 3.4.2.3.1) and shows the typical peaks of nanocrystalline diamond with the D and the G peak at around 1350 cm^{-1} and 1580 cm^{-1} respectively and the peaks at around 1150 cm^{-1} and 1480 cm^{-1} assigned to trans-polyacetylene in the matrix [Fer01] [Pfe05] in the literature.

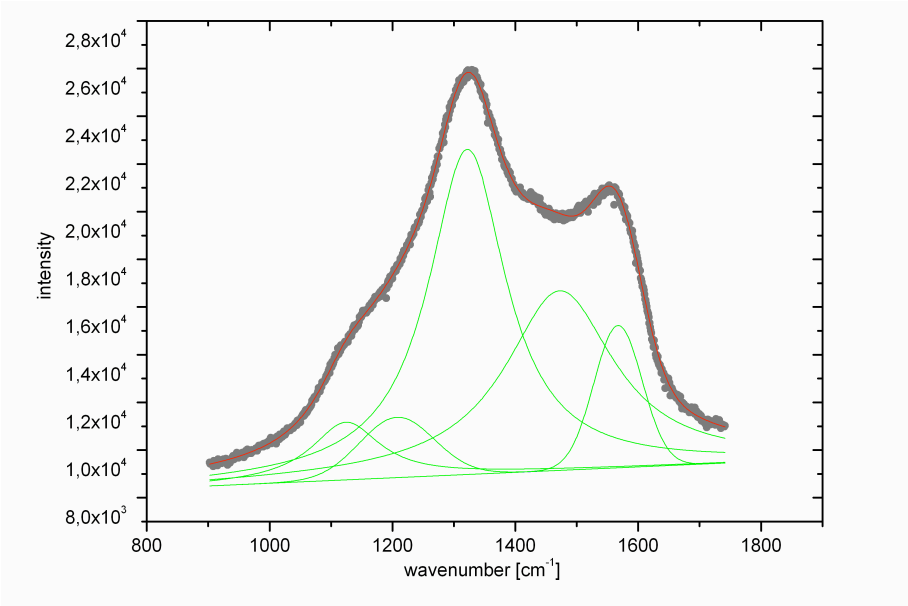

Figure 5.54 Raman spectrum obtained with 632.8 nm laser wavelength. Film deposited with 2.5 % of hydrogen in process gas

The relatively high absorption of UNCD films for visible light (in the order of 10^4 cm^{-1} at a wavelength of about 500 nm) has as a consequence that the absorption of the Raman is no more proportional to the whole film volume but to a volume fixed by the penetration depth.

Raman spectra of the deposited films were investigated to find correlations to the intrinsic tensile stress in the films. Specifically the intensities of the 1150 cm^{-1} and 1480 cm^{-1} peak were investigated because of its origin in the matrix. The intensity of

the trans-polyacetylene peaks is expected to be proportional to the volume of the matrix in the film that has been worked out to be proportional to the tensile intrinsic stress.

Casiraghi et al. pointed out [Cas05] that the intensity and width ratios should be studied separately, since they contain different information. Therefore the relative intensities and the FWHM of the 1150 cm^{-1} and 1480 cm^{-1} peaks are investigated in the following.

To exclude external influences of experimental interferences like variation of laser power etc. normalization to another spectral feature is proposed. Even if no such peak is inherently independent of the hydrogen content, it comes out that normalization to the G and the D-peak show the same trend. Thus normalization is proposed to get a more robust quantitative measure of the intensity of the trans-polyacetylene peak.

Figure 5.55 shows the relative intensities of the peaks at around 1150 cm^{-1} and 1480 cm^{-1} that are usually assigned to trans-polyacetylene in the matrix in correlation to the intrinsic tensile stress. Both peaks were normalized to the intensities of the G and the D-peak.

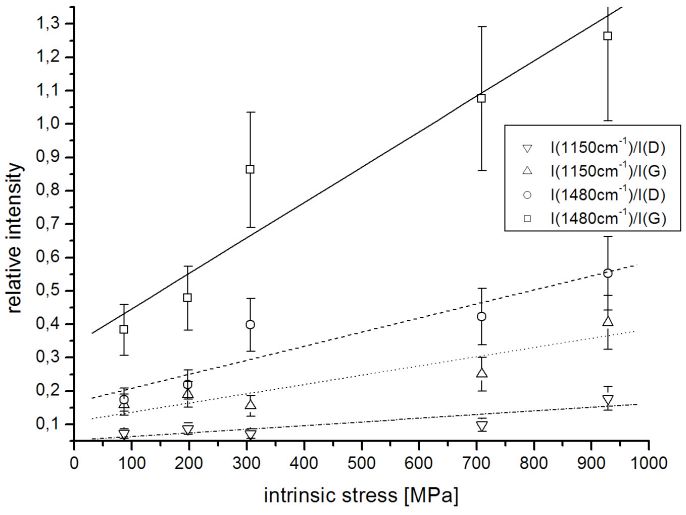

Figure 5.55 Relative intensities of the 1150 cm^{-1} and 1480 cm^{-1} peaks as a function of the intrinsic tensile stress

All relations show the same trend: The intensities of the trans-polyacetylene peaks are proportional to the intrinsic tensile stress in the film. The intensities are increased

by a factor of three for a tensile stress of 1000 MPa compared to the tensile stress at 100 MPa for all lines.

Also the FWHM of the 1480 cm^{-1} peak broaden with increasing tensile stress as shown in Figure 5.56. The same relation applies to the FWHM of the 1150 cm^{-1} peak although the data points are much more scattered compared to the 1480 cm^{-1} peak.

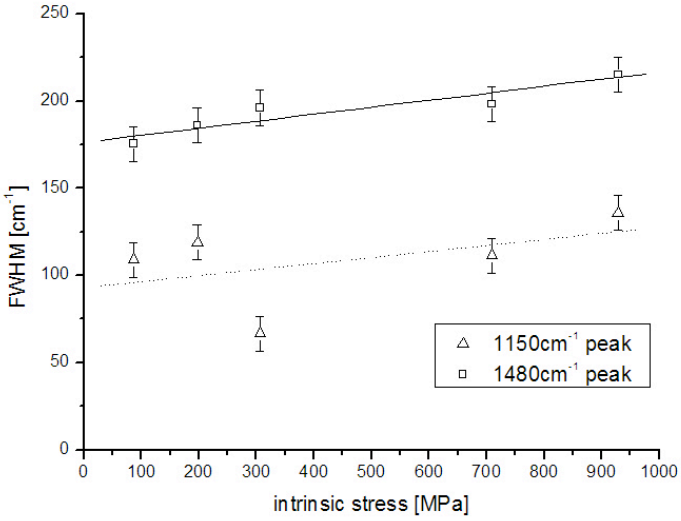

Figure 5.56 FWHM of the 1150 cm^{-1} and 1480 cm^{-1} peaks as a function of the intrinsic tensile stress

As the origin of the 1150 cm^{-1} and 1480 cm^{-1} peaks is supposed to be found in the matrix, these measurements support the presumption that the origin of the tensile intrinsic stress can be found in the matrix and increases with the matrix fraction of the film.

5.4.2 Results of Spectroscopic Stress Measurements

It was shown that there is a correlation of features in the Raman spectrum of UNCD films and the intrinsic stress in the films. Both the intensity and the FWHM of the 1150 cm^{-1} and 1480 cm^{-1} peaks in the spectra correlate with the intrinsic stress. Thus the stress state in UNCD films can be determined without destruction of the sample and even on samples with arbitrary shape. Furthermore the stress measurements with spectroscopic methods allow stress determination with high spatial resolution. Stress distributions in the samples can be measured and investigated by this

method. This is an important finding with respect to quality assurance in industrial coating processes.

5.4.3 Measurement of Coefficient of Thermal Expansion

Results of this chapter are published in [Woe09a]

A crucial parameter of coatings is the residual stress. High stress in films counteracts the adhesion and can lead to failure of the films. The residual stress consists of two components: The thermal stress due to the different coefficients of thermal expansion of the substrate and the film on the one hand, and the intrinsic stress on the other hand. For materials with large differences in their coefficients of thermal expansion and for depositions at high temperature the thermal stress is dominating. A control of the coefficient of expansion of the nanocrystalline film could help to reduce the thermal stress and enhance the adhesion of the film on the substrate.

A comparison of the coefficients of thermal expansion of single crystal diamond and a silicon substrate was already shown in Figure 5.22. For temperatures lower than 600°C the thermal expansion coefficient for diamond is significantly lower compared to the coefficient of silicon resulting in thermal compressive stress in the films. Thus to reduce the stress it would be desireable to fit the coefficients of the UNCD films better to the silicon. In the case of UNCD the coefficient is not only defined by the diamond crystals, but also by the amorphous matrix of the films. Taking typical coefficients of thermal expansion for amourphous carbon films and taking into account the crystal size and the matrix thickness (as calculated in Chapter 5.2.1.4) one can estimate the resulting coefficient of thermal expansion of the UNCD film. Estimating the matrix fraction to be around 10 % of the overall film volume and assuming a coefficient of thermal expansion of $9 \cdot 10^{-6}$/K for the matrix (as found in the literature [Wan98]) one can expect a coefficient of thermal expansion at room temperature that is around $1.8 \cdot 10^{-6}$/K for the UNCD films. This value would clearly fit better to the silicon substrates reducing the thermal stress in the deposited films. To verify this estimation the coefficient of thermal expansion of the UNCD films was measured in the following.

The coefficient of thermal expansion of the UNCD films was determined by measuring the residual stress in the films at different temperatures between room

temperature and 275°C. The bimetal theory [Tim25] was used to calculate the bending of the UNCD-silicon system [Fan00]:

$$\frac{1}{R} = \frac{6(1+m)^2 \int_{T_r}^{T_d} (\alpha_{sub} - \alpha_{film}) dt}{h\left[3(1+m)^2 + (1+mn)\left(m^2 + \frac{1}{mn}\right)\right]} \qquad \text{Equation 5.19}$$

using $m = \frac{t_{film}}{t_{sub}}$, $n = \frac{E_{film}/(1-\nu_{film})}{E_{Sub}/(1-\nu_{Sub})}$ and $h = t_{film} + t_{Sub}$.

With Equation 5.19 and Equation 5.10 it is possible to calculate the relative difference between α_{film} and α_{Sub}.

$$\frac{(1-\nu)}{E_{Sub}} \frac{6 \cdot t_{film}}{t_{Sub}^2} \frac{h\left[3(1+m)^2 + (1+mn)\left(m^2 + \frac{1}{mn}\right)\right]}{6(1+m)^2} \cdot \left(\frac{d\sigma}{dT}\right) = \alpha_{film} - \alpha_{Sub} \qquad \text{Equation 5.20}$$

Taking the coefficient of thermal expansion for silicon from the literature [Sla75] one can calculate the temperature dependent expansion coefficients of the deposited UNCD films and correlate them with the process parameters.

To take in account a change of the elastic modulus with a change in process parameters all samples were subjected to nanoindentation.

The residual stress in all films was measured for different temperatures between room temperature and 275°C as shown in Figure 5.57 for four samples. The change of the residual stress with the sample temperature during measurement can be explained by the bimetal theory as mentioned before: Due to the difference in the coefficients of thermal expansion the stress is changing with temperature. For all measured UNCD samples the residual tensile stress is decreasing with the temperature. This fact directly leads to the conclusion that the coefficients of thermal expansion of the films must be lower than the one of silicon. The difference in the slope of the linear fits to the data points in Figure 5.57 suggest that the coefficient of thermal expansion varies for the deposited UNCD films.

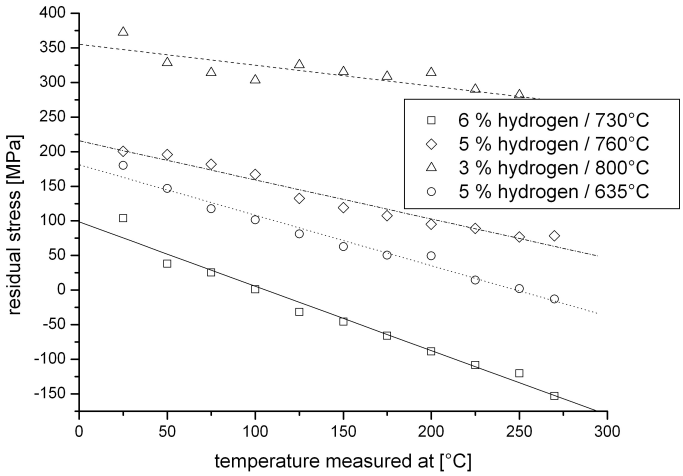

Figure 5.57 Residual stress in UNCD films deposited with different hydrogen admixtures as a function of the temperature where the measurement was performed

To specifically calculate the expansion coefficients for the samples and correlate the values to the process parameters, Equation 5.21 is taken. As one can see, the difference between the coefficients of thermal expansion of silicon and the UNCD films, α_{film} and α_{Sub}, depends on material constants such as elastic modulus, film and substrate thicknesses and the derivative of the residual stress with respect to the temperature. This derivative can be taken directly from the slope of the linear fits in Figure 5.57. Furthermore, the fact that the data points in Figure 5.57 can be fitted linearly shows that the difference between α_{film} and α_{Sub} is not changing in the investigated temperature regime.

Figure 5.58 shows the calculated coefficients of thermal expansion compared to the values of silicon and diamond taken from the literature [Sla75]. This result shows that the coefficients of thermal expansion of UNCD films are higher than the one for microcrystalline diamond and therefore closer to the one of silicon as already predicted by the estimation at the beginning of this chapter. This result explains directly why the adhesion of UNCD films on silicon is better than that of microcrystalline diamond films, as reported in the literature.

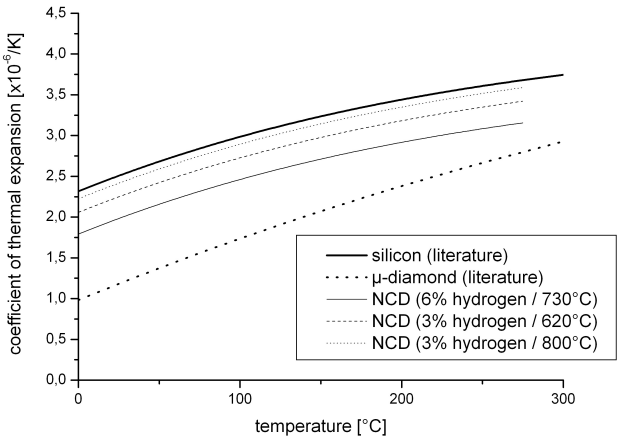

Figure 5.58 Coefficients of thermal expansion of UNCD films with respect to temperature. Values for silicon and microcrystalline diamond taken from [Sla75]

A closer look at the influence of the process parameters on the difference Δα between the coefficients of thermal expansion of silicon and the UNCD films is taken in Figure 5.59.

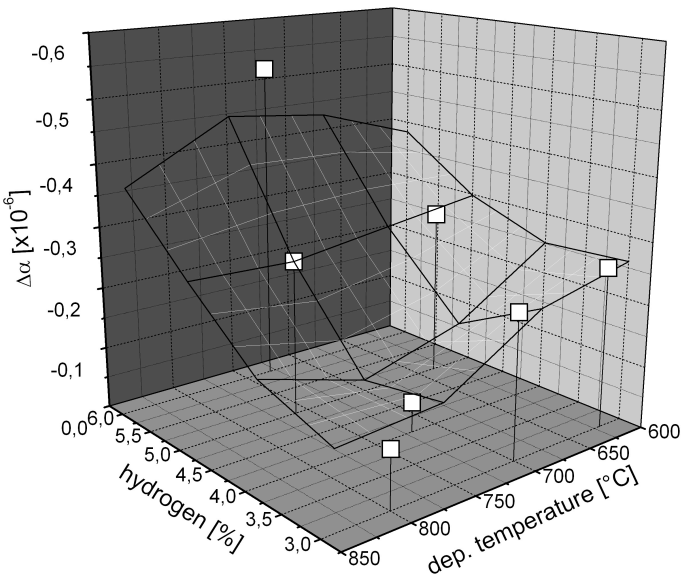

Figure 5.59 Δα of UNCD films compared to silicon with respect to the process parameters

One can clearly see the earlier mentioned trend that the difference between the coefficients of thermal expansion of silicon and diamond is smaller for lower hydrogen content of the process gas. Because the crystal size in diamond films is

inversely proportional to the amount of the hydrogen fraction, one can say that Δα is proportional to the crystal size and is smallest for nanocrystalline films.
Also an influence of the deposition temperature on Δα can be found in Figure 5.59. Higher deposition temperatures seem to be preferable to get UNCD films with expansion coefficients close to that of silicon.

To investigate the influence of nitrogen on the coefficient of thermal expansion, UNCD films were deposited at a pressure of 200 mbar from an $Ar/H_2/CH_4/N_2$ plasma with a fixed hydrogen fraction of 2.5 % and admixtures of nitrogen of 5 % and 7.5 % to the process gas. All other process parameters were similar to the parameters used in the results shown previously. The residual stress in these films was again measured for different temperatures between room temperature and 275°C and the results are shown in Figure 5.60.

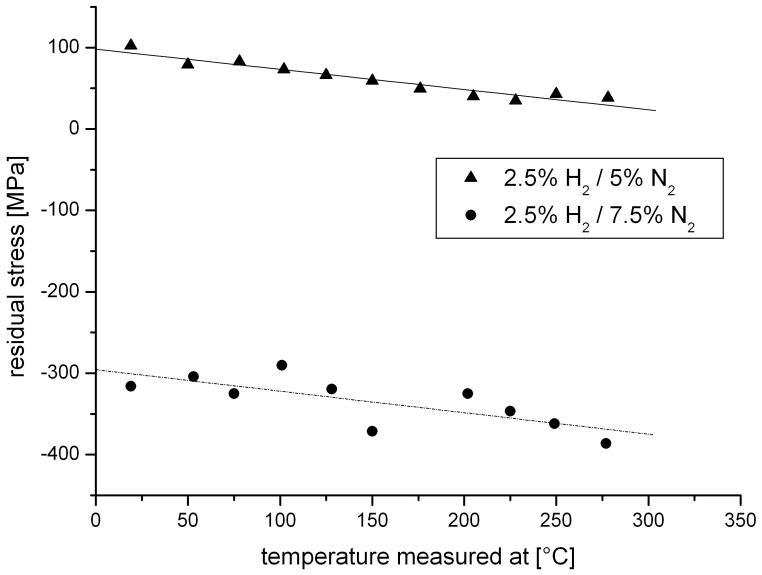

Figure 5.60 Residual stress in UNCD films deposited with different nitrogen admixtures as a function of the temperature where the measurement was performed

The residual stress is decreasing with temperature just like it was for the hydrogen and temperature variation shown in Figure 5.57. This means that coefficients of thermal expansion of the nitrogen-doped films are again lower than the one of silicon.

Figure 5.61 shows the calculated coefficients of thermal expansion compared to the value of silicon and microcrystalline diamond and to a UNCD film deposited without nitrogen.

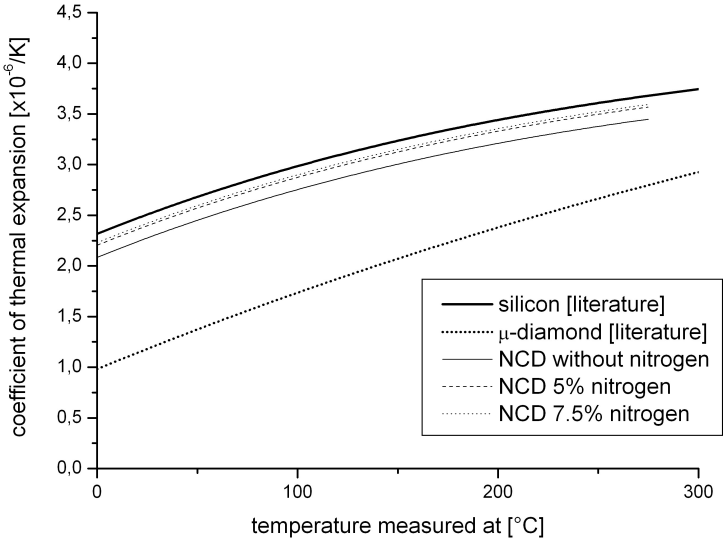

Figure 5.61 Coefficients of thermal expansion of UNCD films with respect to temperature. Values for silicon and microcrystalline diamond taken from [Sla75]

Again the coefficients of thermal expansion of UNCD films are higher than the one for microcrystalline diamond and therefore closer to the one of silicon. Comparing the results with the nitrogen free film one can see that the coefficients of thermal expansion of the nitrogen doped films are even closer to the value for silicon. Also the comparison with the findings in Figure 5.58 where the hydrogen and the deposition temperature was varied leads to the conclusion that the coefficients of thermal expansion are matched even better to the one of silicon by adding nitrogen to the plasma.

The influence of nitrogen on Δα is shown in Figure 5.62. Even for n-doped UNCD-films the coefficient of thermal expansion can be matched to silicon. Indeed, the results suggest that deposition with admixture of nitrogen reduce thermal stress.

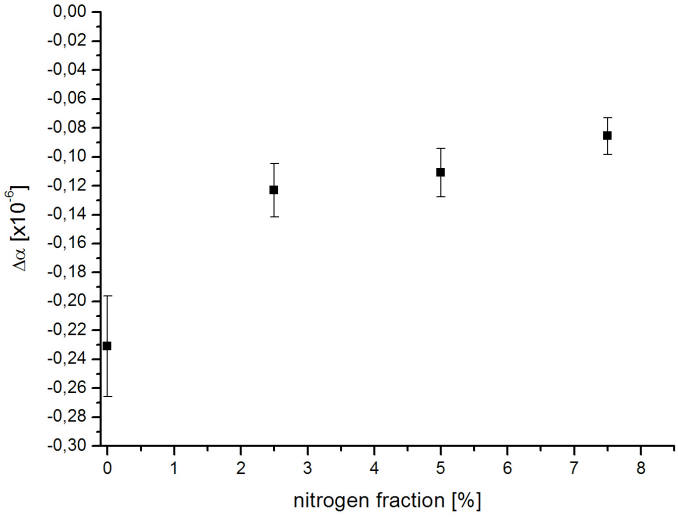

Figure 5.62 Δα of nitrogen doped UNCD films compared to silicon

5.4.4 Summary of the Thermal Expansion Measurements

Nanocrystalline diamond films were deposited in a MW-chamber from $Ar/H_2/CH_4/N_2$ with variation of the hydrogen and nitrogen fraction in the process gas and the substrate temperature during deposition. The change in the residual stress with temperature was used to estimate the coefficients of thermal expansion of the UNCD films in the frame of the bimetal theory.

It was shown that the coefficients of thermal expansion of insulating as well as nitrogen-doped, conducting UNCD films are closer to that of the silicon substrate than microcrystalline diamond films. This result explains the lower thermal stress observed in nanocrystalline diamond films compared to microcrystalline diamond films and is one reason for the better adhesion of these films.

6 Conclusions

UNCD films were deposited by Microwave Plasma CVD from an $Ar/H_2/CH_4$ plasma. For the first time, the importance of the matrix in these films was emphasized and the properties of the diamond grains and the amorphous matrix were investigated separately.

Applying a holistic approach, the influence of the substrate properties on the one hand and the coating and plasma properties on the other hand on the film deposition was investigated. The influence of process parameters like gas composition, pressure etc. on the deposition process – and with that information about the process stability – were investigated. It was shown how these parameters affect the growth, the microstructure and the quality of the deposited films. Moreover the effect of these process parameters on the film components matrix and grains was investigated. Solely by investigating the growth mechanism of these components separately it is possible to tailor UNCD films with specific film properties.

By analyzing the properties of the plasma, it was shown that the C_2/H_α intensity as well as the hydrogen and nitrogen admixture in the process gas have great influence on the growth of the **diamond grains**.

For the first time, the role of the C_2 dimer in UNCD deposition was resolved by separate examination of the nucleation and the growth of diamond as consecutive but yet independent growth steps. It was found that the nucleation density increases with the C_2/H_α intensity while the growth rate decreases at the same time. This finding is a clear evidence that, C_2 only plays a minor role in the growth of the diamond grains, although the C_2 dimer is an important nucleation precursor.

Investigating the structure of the grown diamond grains it was shown that higher C_2/H_α intensities lead to a preferred <220> orientation of the diamond.

No influence of the C_2 on the intrinsic stress in the diamond grains itself was measured in the course of this work.

The influence of the hydrogen admixture to the process gas on the diamond grains was investigated and it was shown that more hydrogen in the plasma leads to higher surface roughness and higher growth rate. The higher hydrogen admixture seems to

counteract the C_2 growth and nucleation process as it - in contrast to the carbon dimer - increases the growth rate and leads to a more randomly oriented structure of the grains with more hydrogen.
While the hydrogen is mainly influencing the size and orientation of the diamond grains, nitrogen in the process gas is influencing the shape of them. Needle shaped crystals where deposited by a certain admixture of nitrogen.

As pointed out before, the – oftentimes overlooked - **film matrix** is of equal importance for the determination of the overall film properties as are the diamond grains. Therefore the influence of the process parameters on the matrix properties was investigated too.
While the C_2/H_α intensity was shown to have great influence on nucleation density and grain orientation, no influence on the matrix could be found with standard methods for investigation of amorphous carbon films. Neither the C-H nor the C-C bonds in the matrix were influenced by changing the C_2/H_α intensity in the plasma as measured by Raman- and FTIR-Spectroscopy.
In contrast to the C_2/H_α intensity, it was found that the hydrogen admixture in the process gas has an influence not only on the diamond grains but also on the film matrix. It was shown that higher amounts of hydrogen lead to more sp^3-CH_x bonds in the matrix while for the C-C bonds the sp^2 configuration is dominant with sp^3 fractions of around 10 % for low hydrogen admixtures and no measurable sp^3 C-C configuration for hydrogen admixtures above 7 %.
Furthermore, it was shown how the substrate temperature during the diamond growth is influencing the matrix fraction in the films, and with it, the intrinsic stress induced by the grain boundaries. Lower substrate temperatures favour films grown with a higher matrix fraction and thus with higher tensile stress. Moreover, lower deposition temperatures favour more sp^3 C-C bonds as well as sp^3 C-H bonds in the matrix giving a third major parameter to influence matrix properties during deposition.

Although the influence of the process parameters on grain growth and matrix properties is of great importance for controlled deposition of films, the **overall film properties** are the most important criteria for the industrial application.

Especially promising are the residual stress measurements where it was shown that the mechanical stress in the films can be adjusted and changed between tensile and compressive stress and that it is even possible to deposit stress free UNCD films.
As expected, the higher nucleation density observed for higher C_2/H_α intensity lead to increased intrinsic stress in the films as predicted by the grain boundary mismatch model. The same effect was shown for the admixture of hydrogen, where the higher hydrogen admixture lead to bigger diamond grains and thus to lower intrinsic stress in the films.
The understanding of the origin of residual stress in nanocrystalline diamond films is an important aspect when it comes to establishing UNCD as a serious material for thin film application. It was shown how measurements were performed for UNCD films and how information regarding the thermal stress and the intrinsic stress were extracted from these measurements. It was shown how it is possible to calculate the thermal stress, and that this thermal stress is compressive in the case of UNCD on silicon substrates. The intrinsic component of the residual stress was calculated to be tensile. Additionally it was shown that it is possible to deposit stress-free films when process parameters are chosen appropriately.
The understanding of these fundamental phenomena leads to a new possibility for the non-destructive measurement of intrinsic stress in nanocrystalline diamond films. While up to now it was necessary to use special methods to measure the residual stress literally “in the laboratory” on special flat samples it is now possible to characterize coated work pieces directly from the production regarding to their intrinsic stress. The measurement can be performed by Raman spectroscopy. The influence of the intrinsic stress on the obtained Raman spectra was shown.
Finally, it is shown that, by variation of process parameters, a control of the thermal expansion coefficient of UNCD is possible. It was shown that the thermal expansion coefficients of all deposited UNCD films fit better to the silicon substrate compared to microcrystalline diamond films. This result explains lower thermal stress in nanocrystalline diamond films compared to microcrystalline diamond films and is one reason for the better adhesion of these films. The results show that deposition at high temperatures seems to be preferable to receive films with low thermal stress.
The results presented in this work are especially important for industrial applications because small and precise components such as MEMS made from nanocrystalline diamond need to be stress free. Also protective coatings made from nanocrystalline

diamond demand to be stress free because the adhesion of such films depends on the residual stress.

7 References

[Aka88] F. Akatsuka, Y. Hirose, K. Komaki; Jpn. J. Appl. Phys., 27 (1988) L1600

[Ang68] J. C. Angus, H. A. Will, W. S. Stanko, J. Appl. Phys. 39 (1968) 2915

[Ang89] J. C. Angus, F. A. Buck, M. Sunkara, T. F. Groth, C. C. Hayman, R. Gat, MSR Bull. 14(10) (1989) 38

[Auc04] O. Auciello, J. Birrell, J. A. Carlisle, J. E. Gerbi, X. Xiao, B. Peng, H. D. Espinosa, J. Phys.: Condens. Matter 16 (2004) R539

[Bac88] P. K. Bachmann, W. Drawl, D. Knight, R. Weimer, R. F. Messier, in Diamond and Diamond-Like Materials, ed. A. Badzian, M. Geis, G. Johnson, MRS Symposium Proceedings, Vol. EA-15 (1988) 99

[Bac91] P. K. Bachmann, H. Lydtin, in Diamond and Diamond-like Films and Coatings, Plenum Press, New York (1991) 829

[Bac92] P. K. Bachmann, D. U. Wiechert, Diamond Relat. Mater., 1 (1992) 422

[Bac95] P. K. Bachmann, Diamond Relat. Mater. 4 (1995) 821

[Bau58a] E. Bauer, Z. Kristallographie, Vol. 110 (1958) 372 – 394

[Bau58b] E. Bauer, Z. Kristallographie, Vol. 110 (1958) 395 – 431

[Bel92] D. N. Belton, S. J. Harris, J. Chem. Phys. 96 (1992) 2371

[Bey82] W. Beyer, H. Wagner, J. Appl. Phys., 53 (1982) 8745 – 8750

[Bi02] B. Bi, W. -S. Huang, J. Asmussen, B. Golding, Diamond Relat. Mater. Vol. 11, Issues 3-6 (2002) 677-680

[Bir05] J. Birrell, J.E. Gerbi, O. Auciello, J.M. Gibson, J. Johnson, J.A. Carlisle; Diam. Rel. Mater. 14 (2005)

[Böh94] V. Böhm, V. Buck, M. Liesenfeld, T. Naubert, J. Zeng, Diamond Relat. Mater. 4 (1994) 33-42

[Bre00] M. Breiter, C. Dopplep, K.-H. Weiß, G. Nutsch: Diamond and Related Materials 9 (2000) 333-336

[Bru95] Bruker Analytische Messtechnik GmbH, user manual FTIR spectrometer IFS 28/IFS 55 EQUINOX®, Ettlingen 1995

[Buc54] W. Buckel, R. Hilsch:Z. Phys. 138 (1954) 109 *(in German)*

[Buc79] V. Buck, Z. Physik B 33, (1979) 349 – 355

[Buc86] V. Buck, Thin Solid Films, 139 (1986) 157 – 168

[Buc89] V. Buck, 7th Intern. Conf. Ion & Plasma Assisted Techniques (1989) 267

[Buc93] V. Buck, Surf. Coat. Technol. 57 (1993) 163 – 168

[Buc98] V. Buck, F. Deuerler, Diamond Relat. Mater. 7 (1998) 1544-1552

[Buc04] V. Buck, N. Wöhrl, R. Spitzl, H. Sung-Spitzl, Galvanotechnik, 95 (2004)8, S. 1980-1984 *(in German)*

[Buc05] V. Buck, Forum Forschung, Public Verlagsgesellschaft und Anzeigenagentur mbH (2005) 24 – 29 *(in German)*

[Buc06] V. Buck, N. Woehrl, A. Poukhovoi, O. Filipov, M. Haase, Y.-Ch. Lee, Proceedings of "Application of Nanocrystalline Diamond and Diamond Like Carbon Materials" IWAncDLC-2006 conference Nov. 28 – Dec 01, 2006, Nihar Ranjan Ray (Ed.) pp. 57 – 66

[Buc07] V. Buck, A. Poukhovoi, Proceedings of "XIV. Workshop Plasmatechnik", June 21. – 22. 2007, Ilmenau *(in German)*

[Buc08a] V. Buck, J. Opto. Adv. Mater. 10 (2008) 85

[Buc08b] V. Buck, N. Woehrl; Jpn. J. Appl. Phys., Vol. 47, No. 10 (2008) 8208

[Buc09] V. Buck, M. Degenhardt, N. Woehrl, Proceedings of „7th Int. Workshop on Microwave Discharges: Fundamentals and Applications" MD-7, Hamamatsu, Japan (2009)

[Bun55] F. P. Bundy, H. T. Hall, H. M. Strong, R. H. Wentorf, Nature, 167 (1955) 51-55

[Cas04] C. Castiglioni, M. Tommasini, G. Zerbi; Phil. Trans . R. Soc. Lond. A (2004)

[Cas05] C. Casiraghi, A. C. Ferrari, J. Robertson, Physical Review B 72, 085401 (2005)

[Chen07] L-J. Chen, N-H. Tai, C-Y. Lee, I-N. Lin, J. Appl. Phys. 101 (2007) 064308

[Cho69] K.L. Chopra: Thin Film Phenomena, Mc Graw-Hill Book Company, N.Y. 1969, p142f

[Con07] CVDiamond XXL^2, Condias GmbH, Retrieved Aug. 16, 2007, from: www.condias.de

[Cyr00] CYRANNUS® III Patent: "Device for the production of homogenous microwave plasma" European Patent No. 0 992 058; USA Patent No. 6,543,380

[Dav93] C. A. Davis, Thin Solid Films, 226 (1993) 30 – 34

[Deg05] M. Degenhardt, diploma thesis, University of Essen, Essen (2005)

[Der75] B. V. Deryagin, D. V. Fedoseev, Sci. Am 233 (1975) 102

[Der76] B. V. Derjagin, B. V. Spitzyn, L. L. Bujlov, Dokl. Acad. Nauk. SSSR., 231 (2) (1976) 333 – 335

[Deu98] F. Deuerler, J. Peterseim, H. Gruner, Q. Wang, V. Buck, Int. J. Ref. Met. Hard Mater. 16 (1998) 191

[Deu06] F. Deuerler, N. Woehrl, V. Buck, Int. J. Refr. Met. Hard Mat., Volume 24, Issue 5, (2006) 392-398

[Dis87] B. Dischler, in Amorphous Hydrogenated Carbon Films, EMRS Symp. Proc. Vol. 17, ed. P. Koidl, P. Oelhafen (Les Èditiones de Physique, Paris) (1987) 189

[Dis98] B. Dischler, in Low-Pressure Synthetic Diamond, eds. B. Dischler, FC. Wild, Sringer Series in Material Processing (1998)

[Don99] C. Donnet, J. Fontaine, F. Lefbevre, A. Grill, V. Patel, C. Jahnes, J. Appl. Phys. 85 (1999) 3264 – 3270

[Eck98] Ecker, K.-H., Reinholz, U., Volbracht, M., Weise, H.-P., Analysis of hydrogen in technical layers, NIM B 136-138, (1998) 1277-1280

[Erd99] A. Erdemir, G. R. Fenske, A. R. Krauss, D. M. Gruen, T. McCauley, R. T. Csencsits, Surface and Coatings Technology, 120-121 (1999) 565-572

[Eve62] W. G. Eversole, US Patents 3 030 287 and 3 030 188 (1962)

[Fan00] Q. H. Fan, J. Grácio, E. Pereira, J. Appl. Phys. 87 (2000) 2880

[Fan02] Q. H. Fan, N. Ali, Y. Kousar, W. Ahmed, J. Gracio: J. Mater. Res., Vol. 17 (2002) 1563

[Fel66] W. Felsch: Z. Physik 195 (1966) 201 (in German)

[Fer00a] A.C. Ferrari, J. Robertson, Phys. Rev. B61 (2000) 14095

[Fer00b] A.C. Ferrari, J. Robertson, Phys. Rev. B64 (2000) 075414

[Fer01] A. C. Ferrari, J. Robertson, Phys. Rev. B 64, 075414 (2001)

[Fer04] A. Ferrari; J. Robertson; Phil. Trans. R. Soc. Lond. A 362 (2004) 2477

[Fey60] R. P. Feynman, Engineering and Science, Vol. 23:5 (1960) 22-36

[Fre88] M. Frenklach, K. E. Spear, J. Mat. Res. 3 (1988) 133

[Fre91] M. Frenklach, in Diamond and Diamond-Like Films and Coatings, Plenum Press, New York (1991) 499

[Ger05] J. E. Gerbi, J. Birrell, M. Sardela, J. A. Carlisle, Thin Solid Films 473 (2005) 41

[Goo93] D. G. Goodwin, J. Appl. Phys. 74 (1993) 6888

[Goy98] Goyette, A.N., Lawler J.E.; Anderson L.W.; Gruen D.M.; McCauley T.G.; Zhou D.; Krauss A.R., Plasma Sources Sci. Technol., Vol. 7, 149 (1998)

[Gra05] S. Yu. Grachev, F. D. Tichelaar, G. C. A. M. Janssen, J. Appl. Phys. 97 (2005) 073508

[Gre02] J. Greene, Talk CEI-Europe Course #51 Thin Film Deposition at the Nanoscale: Mechanisms and Application, Uppsala (2002)

[Gru94] D. M. Gruen, X. Pan, A. R. Krauss, A. Liuy, J. Luo, and C. M. Foster, J. Vac. Sci. Technol. A 12 (1994) 1491

[Gru95] D. M. Gruen, C. D. Zuiker, A. R. Krauss, X. Z. Pan, J. Vac. Sci. Technol. A 13 (1995) 1628

[Gru98] D. M. Gruen, MRS Bulletin, Vol. 23, No. 9 (1998) 32 - 35

[Gru99] D. M. Gruen, Annu. Rev. Mater. Sci. 29 (1999) 211

[Gru04] D. M. Gruen, A. R. Krauss, O. H. Auciello, J. A. Carlisle, (2004) US Patent No. 6793849

[Haa88] M. Haase, diploma thesis, University of Essen, Essen (1988) *(in German)*

[Han88] L. M. Hanssen, W. A. Carrington, J. E. Butler, nK. A. Snail, Mater. Lett. 7 (1988) 289

[Har90] S. J. Harris, Appl. Phys. Lett. 56 (1990) 2298

[Hau93] R. Haubner, B. Lux, Diamond Relat. Mater. 2(9) (1993) 1277 - 1294

[Hee01] A. Heerwagen, M. Strobel, M. Himmelhaus, M. Buck, J. Am. Chem. Soc. 123 (2001) 6732 – 6733

[Heg96] M. I. Heggie, G. Jungnickel, C. D. Latham, Diam. Rel. Mat. 5 (1996) 236

[Hei98] T. Heitz, B. Drévillon, C. Godet, J. E. Bourée, Phys. Rev. B 58 (1998) 13957

[Hei01] B. Heimann, V. Raiko, V. Buck: Int. J. Refract. Met. Hard. Mater. 19 (2001) 169

[Her04] F. J. Hernandez Guillen, K. Janischowsky, W. Ebert, E. Kohn, Phys. status solidi, A, Appl. res., vol. 201, no11 (2004) 2553-2557

[Hir88] Y. Hirose, in First Intern. Conf. on the New Diamond Sci. Technol., New Diamond Forum, Japan (1988) 38

[Hof76] R. W. Hoffman, Thin solid films 34 (1976) 185

[Hon97] S. Hong, M. Y. Chou, Phys. Rev. B 55 (1997) 9975

[Iba97] H. Ibach, Surf. Sci. Rep. 29 (1997) 193 – 264

[Ipl02] technical manual C1-6/10/SC102s/10 © iplas gmbh 2002

[Kam82] M. Kamo, M. Tsutsumi, Y. Sato, N. Setaka, 43rd Japan Appl. Phys. Soc. Fall Meeting (1982)

[Kam83] M. Kamo, Y. Sato, S. Matsumoto, N. Setaka, J. Cryst. Growth, 62(3) (1983) 642

[Kar96] J. Karner, M. Pedrazzini, C. Hollenstein, Diamond Relat. Mater. 5 (1996) 217-220

[Kob99] T. Kobayashi, K. K. Hirakuri, N. Mutsukura, Y. Machi, Diamond Relat. Mater. 8 (1999) 1057

[Kra01] A. R. Krauss, O. Auciello, D. M. Gruen, A. Jayatissa, A. Sumant, J. Tucek, D. C. Mancini, N. Moldovan, A. Erdemir, D. Ersoy, M. N. Gardos, H. G. Busmann, E. M. Meyer, Q. Q. Ding: Diamond Relat. Mater. 10 (2001) 1952

[Kru07] J. Krug; Verhandl. DPG (VI) 42, DS 21.1 (2007) *(in German)*

[Kur05] P. Kury, T. Grabosch, M. Horn- von Hoegen, Rev. Sci. Instrum. 76 (2005)

[Kur88] K. Kurihara, K. Sasaki, M. Kawaradi, N. Koshino, Appl. Phys. Lett., 52 (1988) 437

[Lan76] Lanford, W.A., Trautvetter, H.P., Ziegler, J.F., Keller, J., Appl. Phys. Lett. 28 (1976) 9

[Lan92] Lanford W.A., Nuclear Instruments and Methods in Physics Research B66 (1992) 65-82

[Lan94] T. Lang, J. Laimer, H. Störi, Diamond Relat. Mater. Vol. 3, Issues 4-6, (1994) 470-475

[Lan95] Lanford W.A., Nuclear Reactions for Hydrogen Analysis in Handbook of Modern Ion Beam Materials Analysis, Materials Research Society, (1995) 195-196

[Lan98] K. Landes, J. Zierhut, R. Hartmann: Indirektes Plasmatron, European patent EP 0 851 720 A1 (1998)

[Law98] J.E. Lawler, Talk SFB-Kolloquium, Ruhr-Universität Bochum (1998)

[Lec00] Product cataloque: Pneumatic atomizer nozzles, Lechler GmbH, 2000

[Lee06] Y. C. Lee, S.-J. Lin, D. Pradhan, I.-N. Lin, Diam. Relat. Mat., Volume 15, Issues 2-3, (2006) 353-356

[Lia55] H. Liander, ASEA Jl, 28 (1955) 97-98

[Lin06] I. N. Lin, Y. C. Lee, S. J. Lin, C. Y. Lin, M. C. Yip, W. Fang, Diam. Relat. Mat., vol 15 no 11-12, (2006), p 2046-50

[Liu95] H. Liu, D. S. Dandy, Diamond Chemical Vapor Deposition, Nucleation and early growth stages, Noyes Publications (1995)

[Loc94] R. Locher, C. Wild, N. Herres, D. Behr, P. Koidl, Appl. Phys. Lett. 65 (1994) 34

[Mac05] J. Mack, diploma thesis, University Duisburg-Essen, Essen (2005) *(in German)*

[Mar97] B. Marchon, J. Gui, K. Grannen, G.C. Rauch, J.W. Ager, S.R.P. Silva, J. Robertson, IEEE Trans. Magn. 33 (1997) 3148

[Mat81] S. Matsumoto, N. Setaka, 8th Japan Carbon Soc. Fall Meeting (1981)

[Mat82a] S. Matsumoto, Y. Sato, M. Kamo, N. Setaka, Jpn. J. Appl. Phys. 21 (1982) L183

[Mat82b] S. Matsumoto, Y. Sato, M. Tsutsumi, N. Setaka, J. Mater. Sci. 17 (1982) 3106

[Mat87a] S. Matsumoto, M. Hino, T. Kobayashi, Appl. Phys. Lett. 51 (1987) 737

[Mat87b] E. Matthaei, Hardness Investigation with Low Loads and Their Application for Subsurface Layer Investigation, DGM Informationsges., Oberursel 1987 *(in German)*

[Mat92] S. Matsumoto, Y. Manabe, Y. Hibino, J. Mater. Sci., 27(21) (1992) 5905 - 5910

[May06a] P. W. May, J. N. Harvey, J. A. Smith, Yu. A. Mankelevich, J. Appl. Phys. 99 (2006) 104907

[May06b] P. W. May, Yu. A. Mankelevich, J. Appl. Phys. 100 (2006) 024301

[May07] P. W. May, M. N. R. Ashfold, Yu. A. Mankelevich, J. Appl. Phys. 101 (2007) 053115

[Mes87] R. Messier, A. R. Badzian, T. Bazian, K. E. Spear, P. Bachmann, R. Roy, Thin Solid Films, 153, 1 (1987)

[Mey98] S. Meyer, V. Buck, VI. Workshop Plasmatechnik, 18./19. 06. 1998, Tu Ilmenau, FG Plasma- und Oberflächentechnik, 1998 *(in German)*

[Mey00] S. Meyer*;* Dissertation, Universität Essen (2000) (*in German)*

[Mic04] T. Michely, J. Krug, Springer Serie in Surface Sciences Vol. 42, Berlin: Springer, 2004

[Mos88] M. Moske, K. Samwer, Rev. Sci. Instrum. 59 No. 9 (1988) 2012

[Mul86a] K.-H. Muller, J. Vac. Sci. Technol. A, 4 (1986) 184

[Mul86b] K.-H. Muller, J. Appl. Phys., 59 (1986) 2803

[Oht92] N. Ohtake, M. Yoshikawa, Thin Solid Films, 212(1-2) (1992) 112-121

[Oku01] K. Okumura, P.-G. de Gennes : Eur. Phys. J. E 4 (2001) 121

[Oli04] W.C. Oliver, G.M. Pharr, J. Mater. Res. 19 (2004) 3

[Pan84] J. T. Pan, I. Blech, J. Appl. Phys. 55 (1984) 2874 – 2880

[Pet83] J.B. Pethica, R. Hutchings, W.C. Oliver, Phil. Mag. A48, (1983) 593

[Pfe05] R. Pfeiffer, H. Kuzmany, P. Knoll, S. Bokova, N. Salk, B. Günther, Diam. Rel. Mater. 14 (2005) 470 – 475

[Pis05] S. Piscanec, F. Mauri, A. C. Ferrari, M. Lazzeri, J. Robertson, Diamond Relat. Mater. 14, 1078 (2005)

[Pow01] Powder Diffraction File, Joint Committee on Powder Diffraction Standards, ICDD PDF-2, Newtown Square, PA, 2001, Card 06-0675.

[Pun04] A. Pundt, E. Nikitin, P. Pekarski and R. Kirchheim Acta Materialia, Volume 52, Issue 6, 5 April 2004, Pages 1579-1587

[Rab04] J. R. Rabeau, P. John, J. I.B. Wilson, Y. Fan, J. Appl. Phys. 96, (2004) 6724

[Ris98] J. Ristein, R. T. Stief, L. Ley, W. Beyer, J. Appl. Phys., Vol. 84 (1998) 3836

[Rob93] J. Robertson, Phil. Trans. R. Soc. A 342 (1993) 277

[Rob94] J. Robertson, Pure Appl. Chem. 66 (1994) 1789

[Rob02] J. Robertson, Mater. Sci. Eng., R 37 (2002) 129

[Rot94] B. Rother, D.A. Dietrich, phys. Stat. sol. (a) 142 (1994) 389

[Sai86] S. Saito, S. Matsuda, S. Nogita, J. Mater. Sci. Lett. 5 (1986) 565

[San04] D. Sander, J. Phys.: Condens. Matter 16 (2004) R603 – R636

[Sar91] D. Sarid, Scanning Force Microscopy, Oxford Series in Optical and Imaging Sciences, Oxford University Press, New York (1991)

[Sch69] R. L. Schwoebel, J. Appl. Phys. 40 (1969) 614

[Sen49] A. Brenner, S. Senderhoff, J. Res. Nat. Bur. Stand., 42 (1949) 105

[Sla75] G.A. Slack, S.F. Bartram, J. Appl. Phys. 46, 89 (1975)

[Ste03] M. Sternberg, P. Zapol, L. A. Curtiss, Phys. Rev. B 68 (2003) 205330

[Ste06] H. Sternschulte, T. Bauer, M. Schreck, B. Stritzker, Diamond Relat. Mater. 15 (2006) 542 – 547

[Sto09] G. G. Stoney, Proc. R. Soc. Lond. Ser. A 82 (1909) 172

[Sun04] H. Sung-Spitzl, R. Spitzl, 47th Annual Technical Conference Proceedings (2004) ISSN 0737-5921

[Tim25] S. P. Timoshenko, J. Opt. Soc. Am. 11, 233 (1925)

[UCF98] Diamond Growth and Films, ed. By UCFMG (Universities' Carbon Films and Materials Group) Elsevier Applied Science Publishers LTD 1998

[Van97] T. Vandevelde, M. Nesladek, C. Quaeyhaegens, L.Stals, Thin Solid Films 308 (1997) 154

[Vep99] S. Veprek, J. Vac. Sci. Technol. A 17 (1999) 2401

[VDI06] Guideline VDI 2840: Carbon coatings – Basic knowledge, coating types and properties, Beuth Verlag GmbH, 10772 Berlin, Germany (2006)

[Wad80] N. Wada, P.J. Gaczi, A. Solin, J. Non-cryst. Solids 35-36 (1980) 543

[Wan98] J. S. Wang, Y. Sugimura, A. G. Evans, W. K. Tredway, Thin Solid Films 325 (1998) 163 – 174

[Wik07] Carbon, Wikipedia, Retrieved July 12, 2007, from: http://en.wikipedia.org/wiki/Carbon

[Wil91] C. Willingham, T. Hartnett, C. Robinson, C. Klein, in Applications of Diamond Films and Related Materials, ed. Y. Tzeng, M. Yoshikawa, M. Murakawa, A. Feldman, Materials Science Monographs, 73 Elsevier, Amsterdam (1991)

[Wil93] C. Wild, P. Koidl, W. Müller-Sebert, H. Walcher, R. Kohl, N. Herres, R. Locher, R. Samlenski, R. Brenn, Diamond Rel. Mater. 2, 158 (1993)

[Wil99] Plasma Reactor Patent: European Patent No. 0 438 179; USA Patent No. 5,954,882

[Wil06] O. A. Williams, M. Daenen, J. D'Haen, K. Haenen, J.Maes, V. V. Moshchalkov, M. Nesladek, D. M. Gruen, Diam. Relat. Mater., 15 (2006) 654 - 658

[Win87] H. Windischmann, J. Appl. Phys. 55 (1984) 2874 – 2880

[Win91] H. Windischmann, G. F. Epps, Y. Cong, R. W. Collins, J. Appl. Phys. 69 (1991) 2231

[Win92] H. Windischmann: Critical Review in Solid State and Material Science 17(8) (1992) 547

[Win95] H. Windischmann, K.J. Gray, Diam. Relat. Mater. 4 (1995) 837-842

[Woe03] N. Wöhrl, diploma thesis, University Duisburg-Essen (2003) (*in German*)

[Woe06a] N. Woehrl, V. Buck, Galvanotechnik 12 (2006) 3020 – 3029 *(in German)*

[Woe06b] N. Wöhrl, M. Degenhardt, V. Buck, Tagungsband XIII. Workshop Plasmatechnik, 22. und 23. Juni 2006, B. Dzur (Hrsg.), Technische Universität Ilmenau, Institut für Werkstofftechnik, Fachgebiet Plasma- und Oberflächentechnik, Verlag ISLE, Ilmenau 2006, S. 56 (ISBN 978-3-00-018483-3)

[Woe06c] N. Woehrl, V. Buck: Frühjahrstagung der DPG, Dresden, Verhandl. DPG (VI) 41, DS 7.7 (2006) *(in German)*

[Woe07] N. Woehrl, V. Buck, Diamond Relat. Mater. 16 (4-7) (2007) 748

[Woe09a] N. Woehrl, T. Hirte, O. Posth, V. Buck, Diamond Relat. Mater. 18 (2009) 224-228

[Woe09b] N. Woehrl, S. Reuter, V. Buck, Proceedings of the „19th International Symposium on Plasma Chemistry“, Bochum (2009)

[Xia04] X. Xiao, J. Birrell, J. E. Gerbi, O. Auciello, J. A. Carlisle, J. Appl. Phys., Vol. 96, No. 4 (2004) 2232

[Yan02] W. Yang et al., Nature Materials 1, (2002) 253257

[Yan03] W. Yang, O. Auciello, J. E. Butler, W. Cai, J. A. Carlisle, J. E. Gerbi, D. M. Gruen, T. Knickerbocker, T. L. Lasseter, J. N. Russell Jr., L. M. Smith, R. J. Hamers, Mater. Res. Soc. Symp. Proc. Vol. 737 MRS (2003) F4.4.1

[Yug91] S. Yugo, T. Kanai, T. Kimura, T. Muto, Appl. Phys. Lett. 58, (1991) 1036

[Zai01] A. M. Zaitsev, Optical Properties of Diamond: A data handbook, Springer-Verlag Berlin Heidelberg (2001)

[Zap02] P. Zapol, M. Sternberg, L. A. Curtiss, T. Frauenheim, D. M. Gruen, Phys. Rev. B 65 (2002) 045403

[Zho07] H. Zhou, J. Watanabe, M. Miyake, A. Ogino, M. Nagatsu, DRM 16 (2007) 675

[Zie42] J. Ziegler, N. Nichols: Trans ASME 64 (1942) 759 – 768

Table of Figures